Theoretical study of entanglement and dynamical properties of topological phases of Majorana fermions in one dimension

Takumi Ohta

Contents

Abstract

We study the topological and dynamical properties of the one-dimensional Majorana fermions in the presence of several competing interactions. First part is devoted to the study of the ground-state phase diagram and dynamics of the Majorana fermions. We first map out the ground-state phases of the model and identify the universality classes of the transitions by the exact solution and the conformal-field-theory techniques. Each phase is characterized by order parameters, winding number, and the entanglement spectrum. We then investigate the dynamical properties during temporal linear changes (sweeps) of the parameters of the Majorana interactions through the critical points which separate two topological phases using the time-dependent Bogoliubov transformation with the open boundary condition. When the sweep speed is slow, the correlation functions and the entanglement entropy exhibit characteristic periodic structures in space after the interaction parameter crosses the critical points identified above. On top of this, the degenerate levels in the entanglement spectrum show splitting and oscillating structures. By explicitly calculating the above quantities for excited states, we attribute these behaviors to the Bogoliubov quasiparticles (bogolons) generated near the critical points. We also show that the entanglement spectrum reflects the strength of the Majorana correlations not only in the ground state but also in the excited states.

In the second part, we study the quantum phase transitions and the stability of Majorana zero modes in the one-dimensional Majorana fermions when the chemical potential is periodically modulating in space. We study the non-local properties such as the entanglement spectrum and the string correlation functions by using the numerical Bogoliubov transformation for the open boundary condition. As we vary the phase of the modulation, the number of the Majorana zero modes changes, which manifests itself in the degeneracy of the lowest level of the entanglement spectrum. Next, we investigate the quantum phase transitions driven by the change in the amplitude of the modulation. In particular, for certain values of the wave number and the phase of the modulation, we observe a quantum phase transition from one topological phase into another where there is a single Majorana zero mode and the string correlation function oscillates in space. We also show that in a certain case, the degeneracy of the entanglement spectrum and the number of the Majorana zero modes do not change even for large enough amplitude of the modulation. Finally, we characterize the phases of the system with the periodic boundary condition by the topological invariant, which reflects the number of the zero-energy excitations with the open boundary condition.

Publication list

This thesis is based on the following papers:

- "Phase diagram and sweep dynamics of a one-dimensional generalized cluster model"
  T. Ohta, S. Tanaka, I. Danshita, and K. Totsuka, J. Phys. Soc. Jpn. **84**, 063001 (2015).(Chapter 4)
- "Topological and dynamical properties of a generalized cluster model in one dimension"
  T. Ohta, S. Tanaka, I. Danshita, and K. Totsuka, Phys. Rev. B **93**, 165423 (2016).(Chapter 4)
- "Topological quantum phase transitions in a Majorana chain with spatial modulation"
  T. Ohta and K. Totsuka, J. Phys. Soc. Jpn. **85**, 074003 (2016).(Chapter 5)

Chapter1

Introduction

1.1 Background

Understanding phases of quantum many-body systems is one of the most important topics in the condensed-matter physics. Due to thermal fluctuations, many-particle systems at finite temperatures show a variety of phases. These phases are well described by the Landau theory of symmetry breaking with local order parameters [1]. For example, the Ising model with $\mathbb{Z}_2$ symmetry exhibits two phases when we vary the temperature; one is a symmetry-broken ordered phase with local magnetization as the order parameter, and the other is disordered phase with vanishing local order parameter.

There is another type of fluctuations (quantum fluctuations) which are dominant at zero temperature. Compared to the phases stabilized by thermal fluctuations, quantum fluctuations give rise to more complex phases. Theoretical and experimental studies have discovered phases called topological phases such as quantum Hall effect (QHE) [2, 3], the Haldane phase [4–12], quantum spin liquids [13, 14], and topological insulators [15–19] and superconductors [20, 21]. These phases in one dimension are characterized not by any local order parameters of the Landau theory but by non-local order parameters [6–12], and their emergent edge excitations [4, 22]. In two or higher dimensions, there appear quasiparticles in the bulk which obey fractional statistics [23, 24] and ground-state degeneracy depending on the geometry where the systems are defined [25, 26]. For example, the non-local order parameters [6] for the Haldane phase in the spin-1 Heisenberg antiferromagnet in one dimension are called the string order parameters and are able to detect the hidden antiferromagnetic order in the ground state [4].

The quantum Hall states are insulating in the bulk and metallic at the edges, which are distinct from trivial band insulators. They are realized in the electrons in two dimensions under strong magnetic field and the Hall conductance is proportional to a topological invariant [27]. This number, called the Chern number, reflects the topological nature of the Landau band. In analogy to the QHE, Kane and Mele theoretically predicted the quantum spin Hall effect (QSHE) on the graphene with spin-orbit interactions [15]. This phase is characterized by the spin current at the surface and the $\mathbb{Z}_2$ topological invariant, which in the presence of the time-reversal symmetry is stable until the energy gap closes. Thus this phase is robust against interactions and disorder which preserve time-reversal symmetry. However, it is found that the spin-orbit interaction in the graphene is too weak to show the QSHE. Instead of graphene the use of HgTe/CdTe quantum well has been theoretically proposed and experimentally realized later [16, 17]. The concept of the QSHE is generalized to the three dimensional cases, which is called the topological insulators [18, 19].

The topological superconductors are the topological phases which have superconducting gaps and particle-hole symmetry [21]. Because of the particle-hole symmetry, the zero-energy excitations are the Majorana quasiparticle excitation. One of the simplest models which are known to host these phases would be the Kitaev model of spinless p-wave superconductor in one dimension. [20]. This model is believed to be realized by the proximity effect of a quantum wire placed on superconductors [28–30]. A similar model is obtained using the optically trapped fermion atoms [31]. In the topological phase of the Kitaev model with open boundaries, a pair of unpaired Majorana fermions appearing at the two ends of the system form a non-local fermion excitation with zero energy, leading to the two-fold degeneracy in the ground states. The modes are stable until the energy gap of the system closes and thus characterize the topological phase. Because of the non-local nature of the Majorana fermions, they obey non-Abelian statistics and can be used for the topological quantum computation [32, 33].

In the context of the quantum-information science, quantum entanglement has been proposed to characterize phases. Entanglement is non-local correlation inherent in quantum mechanics. There are mainly two ways to quantify entanglement: entanglement entropy and entanglement spectrum. The entanglement entropy, which is defined as the von Neumann entropy of the reduced density matrix of the subspace, is used to study the quantum phase transitions [34–45]. In the gapped phases, the entanglement entropy satisfies the area law: the entanglement entropy is proportional to the surface area of the subspace [39, 44]. In particular, the entanglement entropy of one-dimensional gapped systems is constant [36]. At the critical points, on the other hand, the entanglement entropy logarithmically diverges; the scaling of the entanglement entropy carries information on the conformal field theories underlying the critical points such as the central charge [34, 35]. The entanglement entropy is also used in the study of the topological phases and reflects topological properties in the ground states [37, 38, 40–43, 45].

The spectrum of the eigenvalues of the reduced density matrix, called the entanglement spectrum, contains more information than the entanglement entropy and thus has been proposed as the fingerprints of topological phases [46]. Sometimes it is more convenient to consider the logarithm of the inverse of the eigenvalues of the reduced density matrix. In Ref. [46], it is shown that the level structure of the entanglement spectrum of the fractional quantum Hall state obtained this way has a close relationship with the energy spectrum of the physical boundary excitations appearing at the edge of the system. Thereafter the entanglement spectrum has been used in theoretical studies of the topological phases and now it is well-known that in a variety of topological phases the level structure of the entanglement spectrum reflects that of the emergent excitations at the edges of the systems [47–59].

1.2 Motivation of this thesis

The study of the Majorana fermions is important from the view point of both quantum-information science and condensed-matter physics. Since the first proposal of quantum computation using the Majorana zero modes [32], the stability of the modes has been attracting much attention from the quantum-information perspective [60–62]. To manipulate them in the actual experiments, we must know entanglement and non-local correlation of them. In condensed-matter physics, on the other hand, much effort has been devoted to the investigation of the topological phases exhibiting the Majorana fermions [63]. As the Kitaev model is the simple model and exactly solved, a lot of theoretical works have use it to explore the Majorana fermions. Because the Kitaev model does not contain all the effects which are relevant in the real experiments, we have to consider them by modifying the Kitaev model. For example, there are theoretical studies concerning the effects of long-range interactions [64,65], periodic modulation [66,67], disorder [68], and quartic interaction [69]. Because several types of Majorana interactions such as long-range ones may change the number of the Majorana zero modes [64, 65], we expect a variety of phases and critical points. Furthermore the stability of the Majorana zero modes against spatially periodic modulation and disorder has been considered in Ref. [66], where the authors found out the enhancement of the topological phase by the modulation and the transitions from the topological phase to a trivial phase. Because the modulation of the chemical potential influences the topological phases by inhomogeneously disturbing the pairing pattern of the Majorana fermions, the interplay of the long-range interaction and the modulating chemical potential would cause non-trivial effects on the formation of topological phases characterized by the Majorana fermions. Thus it would be interesting to study how the pattern of the correlation of the Majorana fermions is affected by the interaction and modulation of chemical potential in the light of entanglement and non-local correlations.

Dynamical properties of systems associated with phase transitions have been extensively studied for a long time [70–81]. In particular, dynamics during temporal linear changes (sweeps) of the parameters of the interactions across the critical points has been investigated [73–80]. In phases characterized by conventional local order parameters, a universal relation called the Kibble–Zurek scaling [71, 72] is known to hold between the defect density and the sweep rate. Recently, connection between the time evolution from the ground states and the topological properties during parameter sweeps across critical points of topological phase transitions has been studied intensively [82–87]. It is found that dynamics associated with topological phase transitions depends on their topological properties and differs from what is expected from the Kibble–Zurek physics [82–85]. In order to further understand how the topology affects the dynamics, it is desired to study the entanglement properties. The references [79–81] found that the dynamics of the entanglement entropy and the entanglement spectrum gives us a new perspective in the study of phase transitions: it may detect the dynamical phase transition. In topological systems in their equilibrium, it has been already recognized that the string correlation functions, the entanglement entropy, and the entanglement spectrum are useful to study the topological phases of the ground states [88]. Thus, it is an important issue to pursue this direction and study dynamical properties in topological systems in terms of the string correlation functions, the entanglement entropy, and the entanglement spectrum of excited states. To focus on only low-lying excitations for simplicity, we study the dynamics during the interaction sweeps rather than following a quench where all the excitations are involved in the dynamics.

1.3 Plan of this thesis

In this thesis, we study entanglement and dynamical properties in topological phases of Majorana fermions in one dimension. This thesis is organized as follows: In Chapter 2, we review the topological phases in one dimension using pedagogical examples such as the spin-1 Heisenberg model and the Kitaev model. We characterize the phases of these models by the entanglement properties, edge modes, and non-local order parameters. There we also introduce a powerful way of representing ground states in one dimension called the matrix-product representation to classify the topological phases.

In Chapter 3, we summarize several numerical methods used in this thesis. We begin with the Bogoliubov-transformation method for free fermion models to study the ground-state and dynamical properties. Then, we sketch the algorithm of a relatively new method, called the infinite time evolving block decimation (iTEBD) [89, 90], based on the matrix-product state to numerically obtain the ground-state wave function. The method to calculate entanglement quantities and correlation functions is also illustrated.

In Chapter 4, which is based on Refs. [91, 92], we present extensive analyses on the ground-state and dynamical properties of a generalized Kitaev model with several competing interactions. We first map out the ground-state phase diagram of the model and characterize each phase by the topological invariant, order parameters, and entanglement. The universality classes of the critical points among these phases are determined analytically. On the basis of the phase diagram obtained in this way, we study the sweep dynamics across the critical points of topological phase transitions. To see topological properties, we calculate the entanglement spectrum as well as the correlation functions and the entanglement entropy. We observe spatially periodic structures in the distance dependence of correlation functions and in the block-size dependence of the entanglement entropy. On the other hand, we observe temporal oscillation and splitting of the degenerate levels of the entanglement spectrum. To clarify why these structures appear, we study the topological properties of the Bogoliubov quasiparticles (bogolons) from a viewpoint of the correlation of Majorana fermions. Focusing on the Majorana correlations, we give a physical picture for the entanglement properties for the excited states. In addition, we discuss the origin of the breakdown of adiabaticity.

In Chapter 5, which is based on the results presented in Ref. [93], we study quantum phase transitions that happen in one-dimensional Majorana-fermion systems under inhomogeneous chemical potential periodically modulating in space when its phase and the amplitude are varied. Specifically, we consider the effect of a next-nearest-neighbor interaction and the periodic modulation in the chemical potential on the topological properties of the Kitaev model focusing on entanglement and non-local correlation. We numerically calculate the entanglement spectrum and the string correlation functions by using the Bogoliubov-transformation method. When we vary the modulation, the degeneracy in the lowest level of the entanglement spectrum changes, which we confirm corresponds to the degeneracy of the ground states and the topological invariant.

In Chapter 6, we conclude this thesis and give some future perspectives. Supplemental information is summarized in Appendices A-E.

Chapter2

Topological phases

In this chapter, we review the topological phases in low dimensions which cannot be understood by the Landau paradigm of symmetry breaking. The Landau theory describes the phase transitions by the pattern of symmetry breaking of the system. A lot of ways have been theoretically proposed to characterize topological phases such as non-local order parameters [6–12], edge modes [4,22], entanglement [37,38,47,48,94–96]. In Sec. 2.1, we use entanglement to define and classify phases. There are topological phases where the symmetries play an important role in the classification, although any symmetries do not break [47,48,94–96]. The phases which are distinct from trivial ones only in the presence of certain symmetries are called the symmetry protected topological phases (Sec. 2.1.1). In Sec. 2.2, we represent the states of this class by the matrix-product states. We illustrate the matrix-product representation of the Haldane phase of $S = 1$ Heisenberg antiferromagnet as the example. In Sec. 2.3, we show the fermion models which we study in Chapters 4 and 5. These models also show topological phases which would be clearly seen in the Majorana representation.

2.1 Entanglement

Entanglement is non-local correlation in quantum mechanics which is absent in classical systems, and is contained in the (ground-state) wave functions. It is widely used in a variety of fields in physics such as statistical mechanics, condensed-matter physics, quantum-information science, quantum field theory and so on. In condensed-matter physics, for example, entanglement can be used to detect the quantum phase transitions [35,36,47,48,58,59]. It is also found that entanglement is useful to characterize phases such as the quantum Hall states [46,53] and quantum spin liquids [37,38] which cannot be described by Landau's local order parameters. In quantum-information science, on the other hand, entanglement is the key to efficiently represent states of quantum many body systems. In fact, we write the wave function by the product of tensors and numerically obtain the ground state by optimizing it.

The amount of entanglement gives us a good criterion in the optimization problem. This fact is used for the iTEBD method [89, 90] and density matrix renormalization group (DMRG) method [97], which are now recognized as efficient ways to obtain the ground-state wave functions of quantum systems in one dimension.

In this section, we see how entanglement is quantified and is used to characterize phases. In Sec. 2.1.1, we show classification scheme beyond that of Landau. In Sec. 2.1.2, we give a representation where the entanglement property is apparent, which is also useful for the matrix-product representation in Sec. 2.2. In Secs. 2.1.3, 2.1.4, we define physical quantities to quantify entanglement.

2.1.1 Entanglement and phases

In condensed-matter physics, we have much interest in the ground-state properties of quantum systems. The system is described by the Hamiltonian H and we usually want the wave function defined in the Hilbert space. We assume that the Hilbert space is spanned by products of local basis $\{|m_i\rangle\}$ of the i-th site. For a long time, we used local order parameters to determine which phase the state belongs to. This is well described by the Landau theory of symmetry breaking based on corresponding order parameter: if the Hamiltonian possesses a symmetry G, then the symmetry group F of the ground state is one of the subgroups of G. This pattern of symmetry breaking enables us to classify the phase transitions. It had been believed that the Landau theory describes all orders and transitions. Since the discovery of the QHEs, however, it turned out that the theory cannot be used for the classification. In fact, all the quantum Hall states have the same symmetry, although there are distinct phases characterized by different topological numbers [27]. Toward construction of new theory which describes new types of order beyond Landau description, several universal properties such as topological degeneracy of the ground states [26] and fractional statistics [23, 24] are theoretically proposed.

Recently it has been found that entanglement plays an important roll in classifying phases [47, 48, 94–96, 98]. To explain it, we first consider that the deformation of states under local unitary transformation. We say that the Hamiltonian is gapped if it has excited states with finite energy gap and it is local if its support of each term is finite. We consider a family of the local Hamiltonian $H(g)$ which smoothly depends on a parameter g. Let the states $|\Psi(0)\rangle$ and $|\Psi(1)\rangle$ be the ground states of the Hamiltonians $H(0)$ and $H(1)$, respectively. We define that the two states $|\Psi(0)\rangle$ and $|\Psi(1)\rangle$ are equivalent if there exist a family of Hamiltonians $H(g)(0 \leq g \leq 1)$ which are gapped and local and they are connected by local unitary transformation [98,99]

$$|\Psi(1)\rangle = T_g[\mathrm{e}^{-\mathrm{i}\int_0^1 dgH(g)}]|\Psi(0)\rangle. \tag{2.1.1}$$

Here T_g is the time ordering with respect to fictitious time-evolution in g. In other word, the two gapped states $|\Psi(0)\rangle$ and $|\Psi(1)\rangle$ are in the same phase if and only if they can be connected by adiabatic transformation without closing the energy gap.

In order to classify the states by the local unitary transformation (2.1.1), the entanglement structure of the wave function $|\Psi\rangle$ turns out to be important. We define that the wave function is *not entangled* if it is written in the direct product form as

$$|\Psi\rangle = \cdots \otimes |s_1\rangle \otimes |s_2\rangle \otimes |s_3\rangle \cdots , \tag{2.1.2}$$

where $|s_i\rangle$ is expanded in the basis $\{|m_i\rangle\}$ of the i-th site. On the other hand, we say that the state is *entangled* if it is not a direct-product state. With the above setup, we classify quantum states. We focus on the entanglement structure of the states and the symmetry of the transformation.

We first consider the case where the system is not subject to any symmetry constraints. The states are called long-range entangled (LRE) if they cannot be deformed into direct product states by *any* local unitary transformations in Eq. (2.1.1). The states remain entangled during the transformation [98]. These LRE states have the intrinsic topological order like the QHEs: they typically have ground-state degeneracy [26] and anyonic excitation [23,24]. This degeneracy depends on the topology of manifolds (cylinder, torus, etc.) on which the system is defined, rather than on the symmetry of the Hamiltonian. On the other hand, the states are called short-range entangled (SRE) if they are connected to a direct product state by a local unitary transformation. Thus the SRE states are continuously transformed to each other and there is only a single SRE phase when no symmetry is imposed.

Next let us consider the case where a certain symmetry G is imposed. Then the SRE states can be richer depending on the symmetry group G. When the symmetry is broken, the phases are described by the Landau theory. The phase transitions are associated with the patterns of symmetry breaking $G \to F$, which are classified by the group theory. On the other hand, there are SRE states where the symmetry of the Hamiltonian is not broken. They are called the *symmetry protected topological (SPT) phases* [100,101], which we focus on this thesis. The states are entangled and cannot be connected to direct product states by the local unitary transformations (2.1.1) which preserve the symmetry. The SPT phases in one dimension are the equivalence classes of symmetric local unitary transformations and are classified by the group cohomology theory [94–96]. Note that there is a classification of the SPT phases in higher dimensions using cobordism [102].

In the presence of the symmetry, there can be distinct phases sharing the same symmetry, and the bulk gap has to close when a phase transition between them occurs. The well known examples of the SPT phases include the Haldane phase protected by such symmetries as inversion and time-reversal symmetries [47] and the topological phase of the Kitaev model protected by time-reversal symmetry and fermion parity [103], which we mainly consider in this thesis. Note that there are also the LRE states with a symmetry constraint, which are called the symmetry enriched topological phases [104, 105].

2.1.2 Schmidt decomposition

We define the Schmidt decomposition by the singular-value decomposition of matrices [106]. Suppose that we have a normalized wave function $|\Psi\rangle$ of the entire system. We then divide the system into two subsystems A and B whose Hilbert spaces are $\mathscr{H}_A$ and $\mathscr{H}_B$, respectively. Defining $n = \dim \mathscr{H}_A$, $m = \dim \mathscr{H}_B$, the wave function $|\Psi\rangle$ is written by the orthonormal basis $\{|i\rangle_A\}, \{|j\rangle_B\}$ of the subsystems A and B as

$$|\Psi\rangle = \sum_{i=1}^{n}\sum_{j=1}^{m} C_{ij}|i\rangle_A|j\rangle_B \in \mathscr{H}_A \otimes \mathscr{H}_B. \tag{2.1.3}$$

The singular-value decomposition of the $n \times m$ matrix C is defined as

$$C = U\Lambda V \tag{2.1.4}$$

with U and V respectively are the generalized unitary matrices of dimensions $n \times \min(n, m)$ and $\min(n, m) \times m$ which satisfy

$$U^\dagger U = 1, \quad VV^\dagger = 1. \tag{2.1.5}$$

The matrix Λ is diagonal with non-negative real elements which are called singular values. The number χ of positive singular values $\{\lambda_\alpha\}$ is called the Schmidt number and satisfies $\chi \leq \min\{\dim \mathscr{H}_A, \dim \mathscr{H}_B\}$. The positive singular values are called the Schmidt eigenvalues. Then we can rewrite the above wave function as

$$|\Psi\rangle = \sum_{i=1}^{n}\sum_{j=1}^{m}\sum_{\alpha=1}^{\min(n,m)} U_{i\alpha}\Lambda_{\alpha\alpha}V_{\alpha j}|i\rangle_A|j\rangle_B. \tag{2.1.6}$$

From Eq. (2.1.5), we can define a new set of orthonormal basis of the subsystems A and B as

$$|\phi_\alpha\rangle_A = \sum_{i=1}^{n} U_{i\alpha}|i\rangle_A, \tag{2.1.7}$$

$$|\psi_\alpha\rangle_B = \sum_{j=1}^{m} V_{\alpha j}|j\rangle_B. \tag{2.1.8}$$

Now, from Eqs. (2.1.6)-(2.1.8), the following *Schmidt decomposition* of any normalized wave function $|\Psi\rangle$ results:

$$|\Psi\rangle = \sum_{\alpha=1}^{\chi} \lambda_\alpha |\phi_\alpha\rangle_A |\psi_\alpha\rangle_B. \tag{2.1.9}$$

Here the states $|\phi_\alpha\rangle_A$, $|\psi_\alpha\rangle_B$ are called the entanglement eigenstates or the Schmidt states. As the wave function is normalized, we obtain the following condition

$$\sum_{\alpha=1}^{\chi} \lambda_\alpha^2 = 1. \tag{2.1.10}$$

When only one Schmidt eigenvalue is finite ($\chi = 1$), the state is a direct product of the wave functions of the two subsystems. Note that although the two subsystems are not entangled in this partition, they may be entangled for some partition. On the other hand, when at least two Schmidt eigenvalues are finite, the state is said entangled.

2.1.3 Entanglement entropy

We define the entanglement entropy to quantify entanglement. To do that we divide a one-dimensional system into two subsystems A and B as in Fig. 2.1.1. Let the size of the subsystem A be L_{sub}. By using the Schmidt decomposition (2.1.9), the wave function $|\Psi\rangle$ is written in terms of the basis of the subsystems A and B as

$$|\Psi\rangle = \sum_{i=1}^{\chi} \lambda_i |\phi_i\rangle_A |\psi_i\rangle_B, \tag{2.1.11}$$

where, $\{|\phi_i\rangle_A\}$ and $\{|\psi_i\rangle_B\}$ are orthonormal basis of the subsystems A and B respectively, and positive real numbers $\{\lambda_i\}$ satisfy $\sum_{i=1}^{\chi} \lambda_i^2 = 1$. With this representation of the wave function, the reduced density matrix ρ_A of the subsystem A is easily calculated as

$$\rho_A = \mathrm{Tr}_B |\Psi\rangle\langle\Psi| \tag{2.1.12}$$

$$= \sum_{i=1}^{\chi} \lambda_i^2 |\phi_i\rangle_A \langle\phi_i|_A. \tag{2.1.13}$$

The trace with respect to subsystem B means that we hide the degree of freedom of B. To quantify entanglement between the subsystem A we observe and the subsystem B we hide, we define the *entanglement entropy* of the subsystem A as the von Neumann entropy for the reduced density matrix ρ_A:

$$S_A = -\mathrm{Tr}\rho_A \ln \rho_A = -\sum_{i=1}^{\chi} \lambda_i^2 \ln \lambda_i^2. \tag{2.1.14}$$

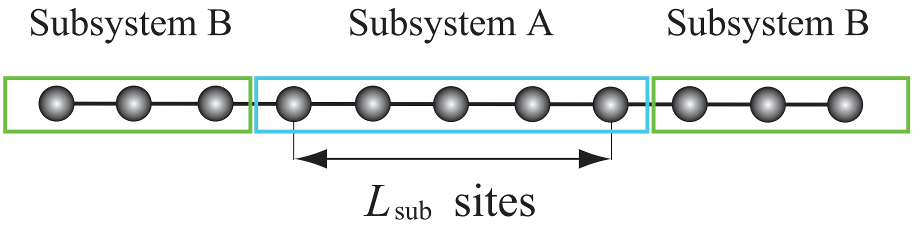

Figure2.1.1 Devision of the system in one dimension: we divide entire system into two subsystems A, B. Let the length of the subsystem A be L_{sub}.

As is easily confirmed, the entanglement entropy S_A equals the entanglement entropy S_B calculated from the reduced density matrix ρ_B

$$\rho_B = \mathrm{Tr}_A |\Psi\rangle\langle\Psi| \tag{2.1.15}$$

$$= \sum_{i=1}^{\chi} \lambda_i^2 |\psi_i\rangle_B \langle\psi_i|_B. \tag{2.1.16}$$

That is, entanglement entropy is related to the boundary of the subsystems A and B rather than themselves. The maximal value of the entanglement entropy $\ln\chi$ is attained when $\lambda_1 = \lambda_2 = \cdots = \lambda_\chi = \frac{1}{\sqrt{\chi}}$. In this case, the two subsystems are called *maximally entangled.*

As a simple example, we consider direct product state and singlet state of two spin one-halves. Let one spin be in the subsystem A and another spin in B. For a direct product state

$$|\Psi\rangle = |\uparrow_1\rangle|\uparrow_2\rangle, \tag{2.1.17}$$

we have $\chi = 1$ and $\lambda_1 = 1$, where the entanglement entropy equals 0. On the other hand, for the singlet state

$$|\Psi\rangle = \frac{1}{\sqrt{2}}\left(|\uparrow_1\rangle|\downarrow_2\rangle - |\downarrow_1\rangle|\uparrow_2\rangle\right), \tag{2.1.18}$$

we have $\chi = 2$ and $\lambda_1 = \lambda_2 = \frac{1}{\sqrt{2}}$. The entanglement entropy is $\ln 2$ and the subsystems are maximally entangled. We can see from above examples that the entanglement entropy quantifies quantum correlation of the system.

The entanglement entropy is useful in the study of quantum phase transitions in one dimension [36]. Here we consider the entanglement entropy of the ground state of a local Hamiltonian. Let $|\partial A|$ be the surface area of the subsystem A. If there is spectral gap above the ground state described by the local Hamiltonian, the correlation length ξ is finite [107]. Then the sites cannot be entangled over the distance ξ. This indicates that entanglement between subsystem A and its complement mainly comes from their boundary and the entanglement entropy of A is proportional to the surface area $|\partial A|$. This is called the *area law* *of the entanglement entropy* [44]. There is a rigorous proof for the area law in the quantum system in one dimension under some condition [39].

When a one-dimensional system is gapless, on the other hand, the entanglement entropy behaves logarithmically with respect to the length L_{sub} of the subsystem [36]. In this case, we obtain the area law with logarithmic correction. The similar behavior can be seen in the entanglement entropy in the (1+1)-dimensional conformal field theories (CFTs) [34, 35]. Generally, in the (1+1)-dimensional CFTs, the entanglement entropy scales logarithmically with respect to the subsystem size L_{sub} as

$$S_A(L_{\mathrm{sub}}) \sim \frac{c}{3} \ln L_{\mathrm{sub}}. \tag{2.1.19}$$

The constant c, called the central charge, is universal constant and classifies the CFTs.

As an example, we consider the transverse-field Ising model which shows quantum phase transition [108, 109]:

$$H_{\mathrm{TFIM}} = -\sum_{i=1}^{N} \sigma_i^x \sigma_{i+1}^x - h \sum_{i=1}^{N} \sigma_i^z. \tag{2.1.20}$$

This model shows a quantum phase transition at $h = 1$ where the energy gap closes. We show the entanglement entropy $S_A(L_{\mathrm{sub}})$ for various h in Fig. 2.1.2. Apart from the critical point, the energy gap is finite and the entanglement entropy becomes constant for sufficiently large L_{sub}. At the critical point $h = 1$, the entanglement entropy behaves logarithmically with respect to the subsystem size L_{sub}:

$$S_A(L_{\mathrm{sub}}) \sim \frac{\frac{1}{2}}{3} \ln L_{\mathrm{sub}}. \tag{2.1.21}$$

Therefore, the critical point of the transverse-field Ising model has $c = \frac{1}{2}$ and the underlying conformal field theory is the free Majorana fermion.

The entanglement entropy is also useful for higher dimensions. In two spatial dimensions, the ground state of gapped system can show topological order. It is known that the entanglement entropy of the subsystem A with a smooth boundary of length L has the following form [37, 38]:

$$S_A(L) = \alpha L - \gamma_{\mathrm{topo}} + \dots, \tag{2.1.22}$$

where the ellipsis represents terms that vanish in the thermodynamic limit. The coefficient α is not universal and arises from short wavelength modes localized near the boundary. The γ_{topo}, called the topological entanglement entropy, is universal constant characterizing a global constraint on the entanglement. This quantity reflects entanglement properties that survive at long distance, and therefore can be studied using an effective field theory (topological quantum field theory) that captures the far-infrared behavior of the system.

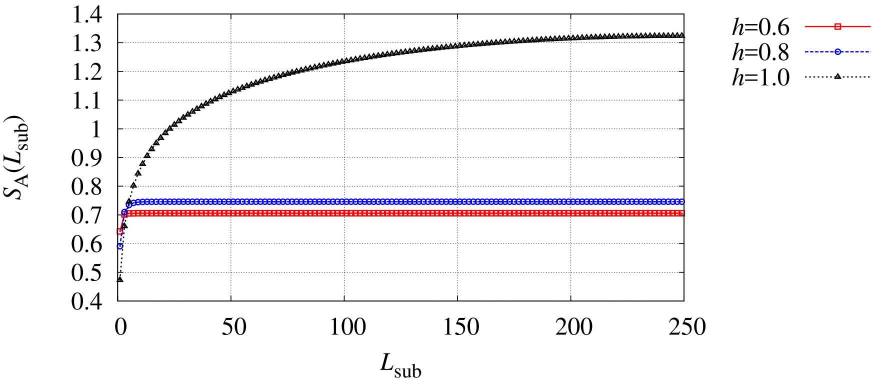

Figure2.1.2 The subsystem size dependence of the entanglement entropy of the transverse-field Ising model [36]: a quantum phase transition occurs at $h = 1$ where the energy gap closes. At $h = 0.6, 0.8$ where the energy gaps are finite, the entanglement entropy closes to constant values as the subsystem size L_{sub} becomes bigger. At the critical point $h = 1$, the entanglement entropy behaves logarithmically. The number of sites is 503 and $L_{\mathrm{sub}} = 249$. (Figure taken from Ref. [110].)

The are law of the entanglement entropy enables us to efficiently describe the wave function. Let us consider the wave function of the gapped Hamiltonian. As we will see in Sec. 2.2, the tensor network states exhibits area law and can express the ground-state wave functions of many-body states efficiently [111]. Since the entanglement entropy becomes constant in the thermodynamic limit in one dimension, the matrix-product state can express the wave function. We can numerically obtain the wave function by using the iTEBD or DMRG methods [89, 90, 97]. In two dimensions, we need other class of tensor networks, called the projected entangled pair state (PEPS) [112]. For critical system which exhibits area law with logarithmic correlation, a class of tensor networks, called the multiscale entanglement renormalization ansatz (MERA), is used to express the wave function [113].

2.1.4 Entanglement spectrum

We define other character, the entanglement spectrum, to quantify entanglement [46]. When we write the reduced density matrix ρ_A as

$$\rho_A = \sum_{i=1}^{\chi} \lambda_i^2 |\phi_i\rangle_A \langle\phi_i|_A \tag{2.1.23}$$

$$= \exp(-H_{\mathrm{E}}), \tag{2.1.24}$$

we can regard the entanglement entropy as the thermal entropy at temperature $T = 1$ with the "Hamiltonian" H_{E} which we call the entanglement Hamiltonian. We define the *entanglement* *spectrum* as the eigenvalues of the Hamiltonian:

$$\xi_i = -\ln \lambda_i^2. \tag{2.1.25}$$

This quantity represents the level structure of the entanglement Hamiltonian H_{E}, and is expected to contain more information than the entanglement entropy. In fact, Li and Haldane have found that the low-lying part of the entanglement spectrum of the ground state corresponds to the low-energy edge modes in the quantum Hall states [46]. After that work, the study of phase transitions of various quantum systems has been done from the perspective of the entanglement spectrum [47–59].

Let us confirm the relation between the entanglement spectrum and the edge modes in a one-dimensional quantum system. We divide an infinite system into two subsystems and focus on the cut end as shown in Fig. 2.1.3. A characteristic mode with zero energy, called the edge mode, may appear at the cut end depending on the interaction pattern. In the Haldane phase of spin-1 Heisenberg antiferromagnet [4, 5]

$$H = \sum_{i=1}^{N} \mathbf{S}_i \cdot \mathbf{S}_{i+1}, \tag{2.1.26}$$

spin-$\frac{1}{2}$ edge modes appear at the ends of the system (see App. A for details): the bulk has $SO(3)$ symmetry whereas the edges transform under under its projective representation $SU(2)$. This edge degree of freedom manifests itself in the two-fold degeneracy in the lowest entanglement level [47, 48]. In fact, we actually see it in the entanglement spectrum of the ground state of spin-1 Heisenberg antiferromagnet in Fig. 2.1.4. In the case of the Kitaev model of spinless p-wave superconductor introduced in Sec. 2.3, the Majorana fermion (real fermion), which is a fractional degree of freedom of the complex fermion, appears as the edge mode. This mode is also reflected in the degeneracy structure of the entanglement spectrum. (Chapter 4).

2.2 Matrix-product state

In this section, we introduce an efficient way of representing quantum states that satisfy the area law, and classify them using entanglement. In Sec. 2.2.1, we introduce the tensor network and its diagrammatic representation. In Sec. 2.2.2, we show how to obtain wave functions in the matrix-product state (MPS) representation, which gives us a very efficient way to represent gapped states in one dimension, and describe the SPT phases with the MPS. The MPS is not unique and has a gage degree of freedom. Using this degree of freedom, we can transform the MPS into a canonical form [114,115]. In Sec. 2.2.3, we give another method

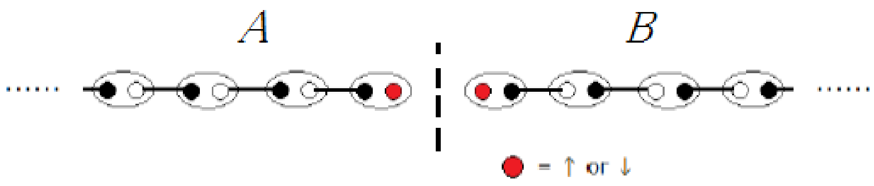

Figure2.1.3 Bipartition of the valence bond solid state: we divide an infinite system into two semi-infinite subsystems A and B. The ground state of the spin-1 Heisenberg antiferromagnet (2.1.26) is well described by the valence bond solid state (see Sec. 2.2.3). As we cut the system along the vertical dotted line, a pair of spin-$\frac{1}{2}$ edge modes appears there. (Figure taken from Ref. [110].)

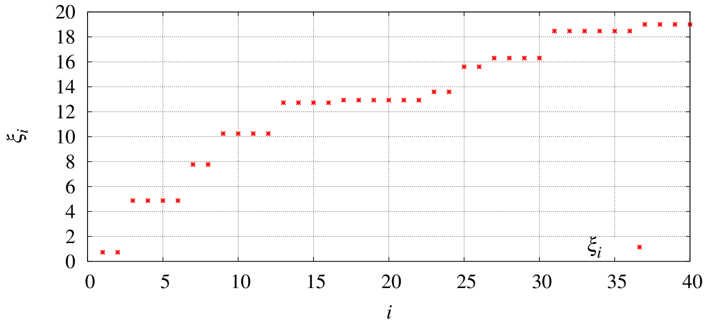

Figure2.1.4 The entanglement spectrum of the ground state of spin-1 Heisenberg antiferromagnet is calculated by the iTEBD method with bond dimension $\chi_{\rm b} = 40$ (see Sec. 2.2). Note that each level is even-fold degenerate. The two-fold degeneracy in the lowest level corresponds to the fictitious edge mode shown in Fig. 2.1.3. (Figure taken from Ref. [110].)

to obtain the matrix-product state and explicitly construct the matrices of the valence bond solid state. In Sec. 2.2.4, we show how the MPS transforms under the symmetry operators under which the Hamiltonian is invariant and how to classify the SPT phases. The review of the MPS and the canonical form is found in Ref. [106].

2.2.1 Tensor network

We define the notation of tensor networks. For a review of tensor networks, see Ref. [116]. Let $A_{i_1,i_2,,\ldots,i_N}$ be a tensor of rank N. In particular, we call the tensors of rank 0, 1, and 2 the scalar, the vector, and matrix, respectively. The diagrammatic representation is shown in Fig. 2.2.1(a). The tensor of rank N has N legs. We define the contraction of tensors A_{ijk} and B_{klm} as the summation over the same indices:

$$C_{ijlm} = \sum_k A_{ijk} B_{klm}, \tag{2.2.1}$$

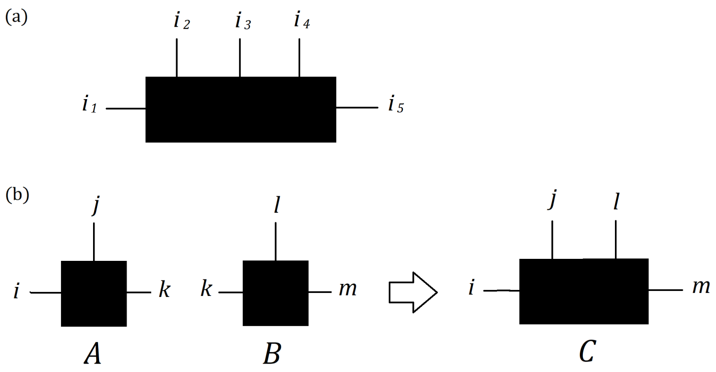

Figure2.2.1 Diagrammatic representation of the tensors. The black tetragons represent the tensors and the legs of them correspond the indices. (a) The tensor of rank 5. (b) The contraction of tensors.

which defines a new tensor C of rank 4. In the diagrammatic representation of Fig. 2.2.1(b), two connected legs are summed up. By contracting tensors, we obtain the tensor network.

2.2.2 Construction of matrix-product state

We construct the matrix representation of a wave function of N-site quantum system in one dimension. In the quantum mechanics, the wave function $|\psi\rangle$ of the system is expanded by the basis of the Hilbert space (physical space) $\{|m_1, \ldots, m_N\rangle\}$ as

$$|\Psi\rangle = \sum_{m_1,\ldots,m_N} C_{m_1,\ldots,m_N} |m_1, \ldots, m_N\rangle, \tag{2.2.2}$$

where the $|m_i\rangle$ is the basis of the local Hilbert space $\mathscr{H}_i$ at the i-th site and m_i represents the physical states at the site i. We call the dimension of $\mathscr{H}_i$ the physical dimension and denote it by d_i. For example, $m_i = 0, 1$ corresponds to the number of a fermion at the i-th site and $d_i = 2$ for a fermion system, and $m_i = -S, -S+1, \ldots, S-1, S$ labels the z-component of a spin at the i-th site and $d_i = 2S+1$ for a system with spin-S. Because the dimension of the Hilbert space (or the number of components of the tensor C) becomes exponentially larger as the size N of the quantum system gets larger, the problem of numerical cost arises in the numerical calculations. One can avoid this problem by rewriting the wave function in the matrix-product representation. Considering the wave function as the tensor of $(N+2)$ legs, we can express it as contraction of matrices as

$$|\Psi\rangle_{\alpha_L \beta_R} = \sum_{\{m_i\},\alpha_1,\ldots,\alpha_{N-1}} A_{\alpha_L,\alpha_1}(m_1) \cdots A_{\alpha_{i-1},\alpha_i}(m_i) A_{\alpha_i,\alpha_{i+1}}(m_i) \cdots A_{\alpha_{N-1},\beta_R}(m_N) |m_1\rangle \cdots |m_i\rangle \cdots |m_N\rangle, \tag{2.2.3}$$

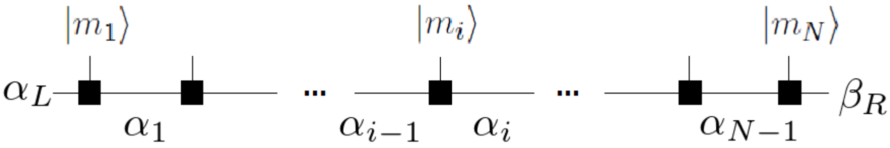

Figure2.2.2 Matrix-product state: black square box is the tensor A. The vertical and horizontal legs represent the physical and ancillary spaces, respectively. Two connected legs are summed up.

In Fig. 2.2.2, we show the diagrammatic representation of the wave function (2.2.3), which we call the *matrix-product state* (MPS). The indices $\{\alpha_i\}, \alpha_L$, $and \beta_R$ represent the ancillary Hilbert spaces, whose dimension is called the *bond dimension* and written as $\chi_{\mathrm{b},i}$. The d_i and $\chi_{\mathrm{b},i}$ may depend on the site index i in general. In the following, for simplicity, let them independent of i and write them d and χ_b, respectively. For large χ_b, the wave function (2.2.3) well approximate the true wave function [116]. As we will see later, if the ground state has a small amount of entanglement, a tensor network with a small bond dimension χ_b can efficiently simulate it .

Next, we consider the MPS representation from the information point of view. To express the wave function by the tensor C, we need d^N components, which grow exponentially in N. On the other hand, we need $\chi_\mathrm{b} \times \chi_\mathrm{b} \times d \times N$ components in Eq. (2.2.3), which grow linearly in N. Thus, this representation greatly reduces the computational cost in numerical calculations.

The MPS utilizes entanglement very well. To see this, we consider the singlet state of two spin-$\frac{1}{2}$, which is maximally entangled:

$$|\Psi\rangle = \frac{1}{\sqrt{2}} \left(|\uparrow_1\rangle |\downarrow_2\rangle - |\downarrow_1\rangle |\uparrow_2\rangle \right). \tag{2.2.4}$$

This state cannot be written in the direct product of two states. That is, there is no set of coefficients $\{C\}$ that satisfies

$$|\Psi\rangle = \sum_{i,j=\uparrow,\downarrow} C_{1,i} |i_1\rangle C_{2,j} |j_2\rangle. \tag{2.2.5}$$

On the other hand, if we define matrices as

$$A(\uparrow_1) = (\frac{1}{\sqrt[4]{2}}\ 0), \quad A(\downarrow_1) = (0\ \frac{1}{\sqrt[4]{2}}), \tag{2.2.6}$$

$$A(\uparrow_2) = (0\ \frac{1}{\sqrt[4]{2}})^\mathrm{T}, \quad A(\downarrow_2) = (-\frac{1}{\sqrt[4]{2}}\ 0)^\mathrm{T}, \tag{2.2.7}$$

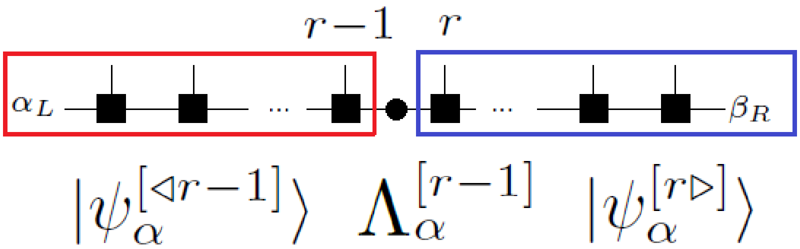

Figure2.2.3 Schmidt decomposition of the wave function $|\Psi\rangle$ between the $(r-1)$-th site and the r-th site. The black circle is the diagonal matrix $\Lambda^{[r-1]}$ of rank 2.

we can represent the singlet state as

$$|\Psi\rangle = \sum_{m_1,m_2=\uparrow,\downarrow} A(m_1)A(m_2)|m_1\rangle|m_2\rangle. \tag{2.2.8}$$

This means that by introducing the ancillary Hilbert spaces, non-local entanglement is encoded in the matrix multiplication. The entanglement structure is clearly seen through the Schmidt decomposition

$$|\Psi\rangle = \sum_\alpha \lambda_\alpha|\psi_\alpha\rangle|\phi_\alpha\rangle, \tag{2.2.9}$$

which we explain in the following.

We rewrite the MPS (2.2.3) by using the Schmidt decomposition [89]. First, we divide the system between the $(r-1)$-th site and the r-th site and perform the Schmidt decomposition (Fig. 2.2.3):

$$|\Psi\rangle = \sum_{\alpha=1}^{\chi_r} \lambda_\alpha^{[r-1]}|\psi_\alpha^{[\triangleleft r-1]}\rangle|\psi_\alpha^{[r\triangleright]}\rangle. \tag{2.2.10}$$

Here the bond dimension χ_r satisfies

$$\chi_r \leq \min\{\mathscr{H}^{[\triangleleft r-1]}, \mathscr{H}^{[r\triangleright]}\} \tag{2.2.11}$$

and the vectors $\{|\psi_\alpha^{[\triangleleft r-1]}\rangle\}$ and $\{|\psi_\alpha^{[r\triangleright]}\rangle\}$ are the orthonormal vectors of the Hilbert space $\mathscr{H}^{[\triangleleft r-1]}$ and $\mathscr{H}^{[r\triangleright]}$. The matrix $\Lambda^{[r-1]}$ of order χ_r is diagonal with positive elements $\Lambda_\alpha^{[r-1]} = \lambda_\alpha^{[r-1]}$.

We further perform the Schmidt decomposition on $|\psi_\alpha^{[r\triangleright]}\rangle$ between the r-th site and the $(r+1)$-th site:

$$|\psi_\alpha^{[r\triangleright]}\rangle = \sum_{\beta=1}^{\chi_{r+1}} \sum_{m_r=1}^{d} \Gamma_{\alpha\beta}^{[r]}(m_r)|m_r\rangle\Lambda_\beta^{[r]}|\psi_\beta^{[r+1\triangleright]}\rangle, \tag{2.2.12}$$

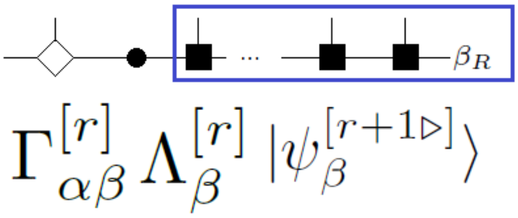

Figure2.2.4 Schmidt decomposition: the white diamond is the tensor $\Gamma^{[r]}$ of rank 3.

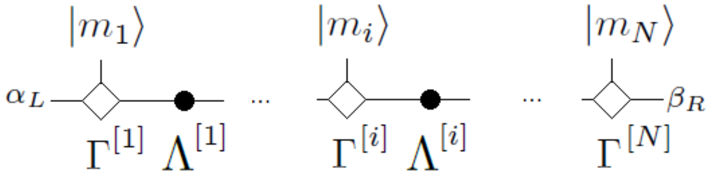

Figure2.2.5 Matrix-product state: the wave function is represented by the matrices $\{\Gamma\}$ and $\{\Lambda\}$.

where the bond dimension χ_r satisfies

$$\chi_r \leq \min\{\mathscr{H}^{[\triangleleft r]}, \mathscr{H}^{[r+1\triangleright]}\}. \tag{2.2.13}$$

Here, we expand the Schmidt basis at the r-th site with the basis of the local Hilbert space $\{|m_r\rangle\}$, whose coefficient we represent by the tensor $\Gamma^{[r]}$ (Fig. 2.2.4). After doing this manipulation for all the sites, we finally obtain the wave function in the matrix-product representation (Fig. 2.2.5) as

$$|\Psi\rangle_{\alpha_L\beta_R} = \sum_{\{m_i\},\{\alpha\},\{\beta\}} \Gamma^{[1]}_{\alpha_L\beta_1}(m_1)\Lambda^{[1]}_{\beta_1\alpha_2}\cdots\Gamma^{[i]}_{\alpha_i\beta_i}(m_i)\Lambda^{[i]}_{\beta_i\alpha_{i+1}}\cdots\Gamma^{[N]}_{\alpha_N\beta_R}(m_N)|m_1\rangle\cdots|m_i\rangle\cdots|m_N\rangle. \tag{2.2.14}$$

We say that the MPS (2.2.14) is in the canonical form [114,115]. Unlike Eq. (2.2.3), the wave function are represented by matrices $\{\Gamma\}$ and $\{\Lambda\}$ instead of $\{A\}$. As we saw above, $\{\lambda^2\}$ are the eigenvalues of the reduce density matrix which contains information on entanglement. If we cut the system between the r-th site and the $(r+1)$-th site and two subsystems are maximally entangled, the entanglement entropy S equals $\ln\chi$ for $\chi = \min\{\mathscr{H}^{[\triangleleft r]}, \mathscr{H}^{[r+1\triangleright]}\}$. Conversely the state in the form of the Schmidt decomposition with fixed χ can express state with the entanglement entropy $S = \ln\chi$ at most. Therefore the estimation of the bond dimension χ_{b} is obtained as

$$\chi_{\mathrm{b}} \sim \mathrm{e}^{S_{\max}}, \tag{2.2.15}$$

where $S_{\max}$ is the maximum value of the entanglement entropy for all possible divisions of the system.

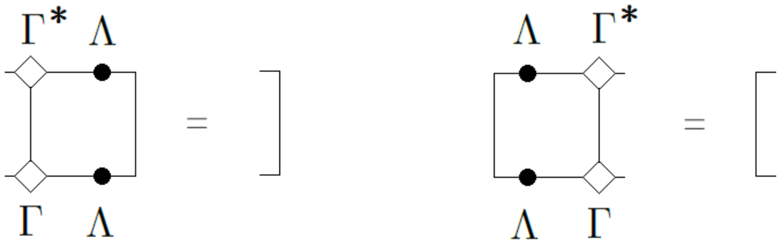

Figure2.2.6 Diagrammatic representation of a canonical form. The right (left) transfer matrix has right (left) eigenvector δ.

As we can easily see, the MPS we have constructed is not unique. Using this degree of freedom, we can transform the MPS into the canonical form [114, 115]. For the MPS of an infinite system, the condition for the canonical form is conveniently expressed in terms of the transfer matrix. We call that an MPS with matrices $\{\Gamma, \Lambda\}$ is a canonical form if the right transfer matrix

$$T^R_{\alpha\bar{\alpha},\beta\bar{\beta}} = \sum_i \Gamma(i)_{\alpha\beta}\Gamma^*(i)_{\bar{\alpha}\bar{\beta}}\Lambda_\beta\Lambda_{\bar{\beta}} \tag{2.2.16}$$

has a right eigenvector $\delta_{\beta\bar{\beta}}$ with the eigenvalue 1, and the left transfer matrix

$$T^L_{\alpha\bar{\alpha},\beta\bar{\beta}} = \sum_i \Lambda_\alpha\Lambda_{\bar{\alpha}}\Gamma(i)_{\alpha\beta}\Gamma^*(i)_{\bar{\alpha}\bar{\beta}} \tag{2.2.17}$$

has a left eigenvector $\delta_{\alpha\bar{\alpha}}$ with the eigenvalue 1. These conditions are diagrammatically shown in Fig. 2.2.6. We require the 1 is the non-degenerate largest (in its modulus) eigenvalue. This condition turns out to be that the state is not a cat state [117, 118].

There are some merits in using the canonical form. First, as we have already seen, it clarifies the entanglement structure of the state, which enables us to obtain the ground-state wave function efficiently in numerical calculations such as iTEBD and DMRG methods. Second, the calculations of physical quantities such as overlap of wave functions and correlation functions substantially are simplifies with the canonical form. Since the expectation values of local operators with respect to the wave function contains the products of transfer matrices, only the largest eigenvalue becomes important in the infinite system. This fact reduces the computational cost very much.

2.2.3 Valence bond construction

There is another method to construct the MPS, which we call the valence bond construction. In this construction, we put two spins of $S = \frac{1}{2}$ at each site and make singlet pairs (maximally entangled states) between neighboring spins. On top of the spin $|\alpha\rangle$, we introduce the conjugate spin $|\tilde{\alpha}\rangle$ by

$$|\tilde{\alpha}\rangle = \sum_{\beta=1}^{2} R_{\alpha,\beta}|\beta\rangle. \tag{2.2.18}$$

The orthogonal condition $\langle\tilde{\alpha}|\tilde{\beta}\rangle = \delta_{\alpha\beta}$ implies that the matrix R is unitary. We determine it so that the neighboring spin-$\frac{1}{2}$'s form a singlet

$$\sum_{\alpha=1}^{2} |\alpha\rangle|\tilde{\alpha}\rangle = \sum_{\alpha,\beta}^{2} R_{\alpha\beta}|\alpha\rangle|\beta\rangle, \tag{2.2.19}$$

$$R = \begin{pmatrix} 0 & 1 \\ -1 & 0 \end{pmatrix}. \tag{2.2.20}$$

Next, we consider an operator that projects two spin-$\frac{1}{2}$'s onto a spin-1 as

$$\hat{A}(i) = \sum_{\alpha,\beta,m_i} B_{\alpha\beta}(m_i)|m_i\rangle\langle\alpha\beta| \tag{2.2.21}$$

$$= \sum_{\alpha,\beta,\gamma,m_i} B_{\alpha\beta}(m_i)R_{\gamma\alpha}|m_i\rangle\langle\tilde{\gamma}\beta|, \tag{2.2.22}$$

$$B = \frac{1}{\sqrt{2}}\begin{pmatrix} \sqrt{2}|1\rangle & |0\rangle \\ |0\rangle & \sqrt{2}|-1\rangle \end{pmatrix}. \tag{2.2.23}$$

Thus from

$$\hat{A}(i) = \frac{1}{\sqrt{2}}\begin{pmatrix} |0_i\rangle & \sqrt{2}|-1_i\rangle \\ -\sqrt{2}|1_i\rangle & -|0_i\rangle \end{pmatrix}, \tag{2.2.24}$$

the MPS representation of the state is given by the matrices

$$\Gamma(1) = \begin{pmatrix} 0 & 0 \\ -1 & 0 \end{pmatrix}, \quad \Gamma(0) = \frac{1}{\sqrt{2}}\begin{pmatrix} 1 & 0 \\ 0 & -1 \end{pmatrix}, \tag{2.2.25}$$

$$\Gamma(-1) = \begin{pmatrix} 0 & 1 \\ 0 & 0 \end{pmatrix}, \quad \Lambda = \frac{1}{\sqrt{2}}\begin{pmatrix} 1 & 0 \\ 0 & 1 \end{pmatrix}. \tag{2.2.26}$$

We call the state the *valence bond solid (VBS) state*. The entanglement entropy of the state is $\ln 2$, which implies that it is a maximally entangled state.

Precisely speaking, the MPS we have obtained above is not in the canonical form. We can check that a simple renormalization

$$\tilde{\Gamma}(m) = \frac{2}{\sqrt{3}}\Gamma(m) \tag{2.2.27}$$

makes Eqs. (2.2.25) and (2.2.26) canonical:

$$\tilde{\Gamma}(1)=\begin{pmatrix}0 & 0\\ -\frac{2}{\sqrt{3}} & 0\end{pmatrix},\quad \tilde{\Gamma}(0)=\begin{pmatrix}\sqrt{\frac{2}{3}} & 0\\ 0 & -\sqrt{\frac{2}{3}}\end{pmatrix},\tag{2.2.28}$$

$$\tilde{\Gamma}(-1)=\begin{pmatrix}0 & \frac{2}{\sqrt{3}}\\ 0 & 0\end{pmatrix},\quad \Lambda=\frac{1}{\sqrt{2}}\begin{pmatrix}1 & 0\\ 0 & 1\end{pmatrix}.\tag{2.2.29}$$

This expression is used to study the Haldane phase.

The VBS state we have constructed above is the ground state of a certain Hamiltonian, which we construct in the following. We consider the four spin-$\frac{1}{2}$'s on the i-th and $(i+1)$-th sites. Since the two spin-$\frac{1}{2}$'s on the neighboring sites form the singlet by construction, the total spin of two neighboring sites is $S=0$ or 1. Thus the VBS is the eigenstate with zero energy (lowest energy) of the operator $P^{S=2}_{i,i+1}$ which projects the space of the two spin-1's at the i-th and $(i+1)$-th sites onto the space of total spin $S_{\mathrm{tot}}=2$. Using equations

$$(\mathbf{S}_i+\mathbf{S}_{i+1})^2=2S(S+1)+2\mathbf{S}_i\cdot\mathbf{S}_{i+1}\quad (S=1),\tag{2.2.30}$$

$$\mathbf{S}_i\cdot\mathbf{S}_{i+1}=\begin{cases}-2 & (S_{\mathrm{tot}}=0),\\ -1 & (S_{\mathrm{tot}}=1),\\ 1 & (S_{\mathrm{tot}}=2),\end{cases}\tag{2.2.31}$$

the projection operator $P^{S=2}_{i,i+1}$ is written as

$$P_{S=2}=\frac{1}{2}\left[(\mathbf{S}_i\cdot\mathbf{S}_{i+1})+\frac{1}{3}(\mathbf{S}_i\cdot\mathbf{S}_{i+1})^2+\frac{2}{3}\right].\tag{2.2.32}$$

The sum of the projection operators is called the Affleck–Kennedy–Lieb–Tasaki (AKLT) model [4, 5]

$$H=\sum_{i=1}^{N}\left[\mathbf{S}_i\cdot\mathbf{S}_{i+1}+\frac{1}{3}(\mathbf{S}_i\cdot\mathbf{S}_{i+1})^2+\frac{2}{3}\right],\tag{2.2.33}$$

whose ground state is the VBS state. With the periodic boundary condition, the VBS state is the unique ground state. However with the open boundary condition, it is not. In fact, there is a spin-$\frac{1}{2}$ degree of freedom at each end of the system which does not forms a singlet with other spins at neighboring sites. In the matrix-product representation, we can freely choose the matrix indices (α_L,β_R) of the VBS state. This degree of freedom is regarded as coming from the two $\frac{1}{2}$ spins at its edges, which are called the edge states. Therefore the ground states are four-fold degenerate due to the two free spin-$\frac{1}{2}$'s.

The VBS state has also been used to study the Haldane phase of the spin-1 Heisenberg antiferromagnet [4,5]

$$H = \sum_{i=1}^{N} \mathbf{S}_i \cdot \mathbf{S}_{i+1}. \tag{2.2.34}$$

Though the VBS state is not the exact ground state of the above Hamiltonian, it provides a good qualitative approximation to the true ground state. See App. A for detail of the Haldane phase.

2.2.4 Symmetry operation

If the state is invariant under a certain symmetry represented as a unitary matrix Σ_{ij}, the transformed matrix can be shown to satisfy

$$\sum_j \Sigma^g_{ij} A(j) = \mathrm{e}^{\mathrm{i}\theta_g} U_g^\dagger A(i) U_g, \quad A(i) = \Gamma(i)\Lambda, \tag{2.2.35}$$

where g is an element of the group G, the matrix U_g is unitary, and $\mathrm{e}^{\mathrm{i}\theta_g}$ is a phase factor. The diagrammatic representation is shown in Fig. 2.2.7. This equation is very important for classifying the SPT phases. The proof is as follows. We define a generalized transfer matrix

$$\begin{aligned} T^{\Sigma}_{\alpha\bar{\alpha},\beta\bar{\beta}} &= \sum_{i,j} A^*_{\bar{\alpha}\bar{\beta}}(j) A_{\alpha\beta}(i) \langle j|\Sigma|i\rangle & (2.2.36)\\ &= \sum_{i,j,n} A^*_{\bar{\alpha}\bar{\beta}}(j) A_{\alpha\beta}(i) \langle j|n\rangle \mathrm{e}^{\mathrm{i}\theta_n} \langle n|i\rangle & (2.2.37)\\ &= \sum_n \mathrm{e}^{\mathrm{i}\theta_n} \tilde{A}^*_{\bar{\alpha}\bar{\beta}}(n) \tilde{A}_{\alpha\beta}(n), & (2.2.38) \end{aligned}$$

where $\{|n\rangle\}$ are the eigenstates of Σ and

$$\begin{aligned} \Sigma|n\rangle &= \mathrm{e}^{\mathrm{i}\theta_n}|n\rangle, & (2.2.39)\\ \tilde{A}(n) &= \sum_i \langle n|i\rangle A(i). & (2.2.40)\\ & & (2.2.41) \end{aligned}$$

From the lemma 1 of Ref. [118], the eigenvalue λ_σ of the transfer matrix (2.2.36) satisfies

$$|\lambda_\sigma| \leq 1 \tag{2.2.42}$$

with equality holding if and only if there exist a unitary matrix U and θ such that

$$U\tilde{A}(n) = \tilde{A}(n) U \mathrm{e}^{\mathrm{i}(\theta - \theta_n)} \tag{2.2.43}$$

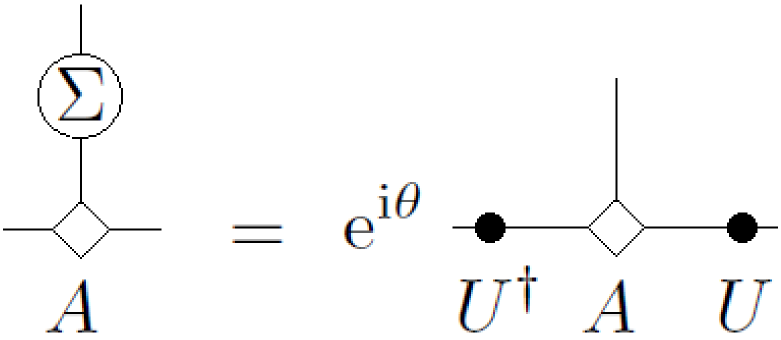

Figure2.2.7 Diagrammatic representation of the symmetry operation to the MPS. The matrix Σ acts on the physical index of tensor A. The black circles represent the unitary matrices U and $U^\dagger$.

and the transfer matrix has one non-degenerate eigenvalue of modulus 1. By following calculation using this lemma,

$$\sum_i \langle n|i\rangle U^\dagger A(i) U = \sum_i \mathrm{e}^{-\mathrm{i}(\theta-\theta_n)}\langle n|i\rangle A(i) \tag{2.2.44}$$

$$= \sum_i \mathrm{e}^{-\mathrm{i}\theta}\langle n|\Sigma|i\rangle A(i) \tag{2.2.45}$$

$$= \sum_{i,j} \mathrm{e}^{-\mathrm{i}\theta}\langle n|j\rangle\langle j|\Sigma|i\rangle A(i), \tag{2.2.46}$$

we complete the proof of Eq. (2.2.35).

We focus on the transformation law of the MPS under the symmetry operation. As we vary g over the whole group G, we obtain phase factors $\{\mathrm{e}^{\mathrm{i}\theta_g}\}$ and matrices $\{U_g\}$. The phases form one-dimensional representation of the symmetry group. The matrices $\{U_g\}$, however, may differ from the ordinary (linear) representation of the group G up to phase factor: for the representation satisfying

$$\Sigma^g\Sigma^h = \Sigma^{gh}, \quad g,h \in G, \tag{2.2.47}$$

the matrices $\{U_g\}$ satisfy

$$U_g U_h = \mathrm{e}^{\mathrm{i}\rho(g,h)} U_{gh}. \tag{2.2.48}$$

Here the phases $\rho(g,h)$ are called the factor system of the representation. Thus the matrices $\{U_g\}$ form the projective representation. If $\rho(g,h) = 0$ for all the element of the group G, the projective representation reduces to the usual linear representation.

The projective representation is used to classify the SPT phases. For later convenience, we rewrite the phase factor $\mathrm{e}^{\mathrm{i}\rho(g,h)}$ as

$$\omega(g,h)=\mathrm{e}^{\mathrm{i}\rho(g,h)}. \tag{2.2.49}$$

From the associativity condition of the representation

$$(\Sigma^{g_1}\Sigma^{g_2})\Sigma^{g_3}=\Sigma^{g_1}(\Sigma^{g_2}\Sigma^{g_3}),\quad g_1,g_2,g_3\in G, \tag{2.2.50}$$

the factor system satisfies

$$\omega(g_2,g_3)\omega(g_1,g_2g_3)=\omega(g_1,g_2)\omega(g_1g_2,g_3). \tag{2.2.51}$$

Because we have a different choice of pre-factor of the matrix U_g

$$U'_g=\beta(g)U_g, \tag{2.2.52}$$

we obtain the same physics with different factor system $\omega'(g_1)$

$$\omega'(g_1,g_2)=\frac{\beta(g_1g_2)}{\beta(g_1)\beta(g_2)}\omega(g_1,g_2). \tag{2.2.53}$$

Suppose we have projective representations U_{1g} and U_{2g} with factor systems $\omega_1(g,h)$ and $\omega_2(g,h)$, respectively. Then we can see that $U_{1g}\otimes U_{2g}$ is the projective representation with factor system $\omega_1(g,h)\omega_2(g,h)$ Under such a product rule and the equivalent condition in Eq. (2.2.53), the equivalent classes of factor systems form an Abelian group whose identity element is the class of the linear representation. This group is called the second cohomology group $H^2(G,U(1))$ of the group G with coefficients in the $U(1)$ group and classifies the SPT phases in one dimension [47, 48, 94–96].

For a given factor system $\omega(g_1,g_2)\in H^2(G,U(1))$, we can construct a state in the corresponding SPT phase as follows. As shown in Fig.2.2.8, we put two (left and right) spins with basis state $|g\rangle$ ($g\in G$) at each site and pair up left and right spins at neighboring sites

$$\sum_g|gg\rangle \tag{2.2.54}$$

as we do in Sec. 2.2.3. Then the symmetry operation on the left spin is given by

$$U_{g_2}|g_1\rangle=\omega(g_1^{-1}g_2^{-1},g_2)|g_2g_1\rangle. \tag{2.2.55}$$

Using the equivalent condition in Eq. (2.2.53), we can show that

$$U_{g_3}U_{g_2}|g_1\rangle=\omega(g_1^{-1}g_2^{-1},g_2)\omega(g_1^{-1}g_2^{-1}g_3^{-1},g_3)|g_3g_2g_1\rangle \tag{2.2.56}$$

$$=\omega(g_1^{-1}g_2^{-1}g_3^{-1},g_3g_2)\omega(g_3,g_2)|g_3g_2g_1\rangle, \tag{2.2.57}$$

$$U_{g_3g_2}|g_1\rangle=\omega(g_1^{-1}g_2^{-1}g_3^{-1},g_3g_2)|g_3g_2g_1\rangle \tag{2.2.58}$$

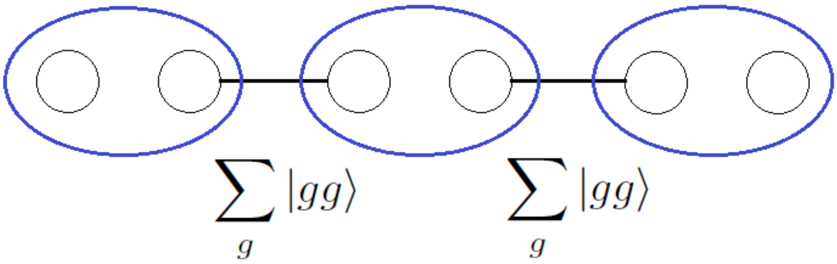

Figure2.2.8 Left and right spins (circles) are put on each site (blue ellipse). The edge spin carries the projective representation.

and therefore matrices $\{U_g\}$ forms the projective representation with the factor system ω

$$U_{g_3}U_{g_2} = \omega(g_3, g_2)U_{g_3 g_2}. \tag{2.2.59}$$

Similarly the symmetry operation on the right spin is given by

$$U_{g_2}^{-1}|g_1\rangle = \omega^{-1}(g_1^{-1}g_2^{-1}, g_2)|g_2 g_1\rangle \tag{2.2.60}$$

form the projective representation with the factor system ω^{-1}. When the system has a boundary, the edge spin carries the projective representation.

The non-trivial projective representation has a direct physical consequence. When we consider a state in an SPT phase with the open boundary condition, there appear localized spins at the edges of the system carrying the projective representation. Because the dimension of the representation space is at least two, the degree of freedom of these spins is at least two, which give rises to the ground-state degeneracy.

As we see that the project representation is useful for classifying the SPT phases, we show how to obtain it in the actual calculation [119]. The procedure is shown in the diagrammatic representation in Fig. 2.2.9. If the wave function $|\Psi\rangle$ in the canonical matrix-product representation is invariant under the symmetry operation of symmetry G, we have the condition

$$\left|\langle\Psi|\tilde{\Psi}\rangle\right| = 1, \tag{2.2.61}$$

where the state $|\tilde{\Psi}\rangle$ is the transformed wave function under $g \in G$. This implies that the generalized transfer matrix

$$T^{\Sigma^g}_{\alpha\bar{\alpha},\beta\bar{\beta}} = \sum_{i,j} \Sigma^g_{ij}\tilde{\Gamma}_{\alpha\beta}(j)\Gamma^*_{\bar{\alpha}\bar{\beta}}(i)\Lambda_\beta\Lambda_{\bar{\beta}} \tag{2.2.62}$$

has the largest eigenvalue η satisfying $|\eta| = 1$ [118]

$$\sum_{\beta\bar{\beta}} T^{\Sigma^g}_{\alpha\bar{\alpha},\beta\bar{\beta}} X_{\beta\bar{\beta}} = \eta X_{\alpha\bar{\alpha}}. \tag{2.2.63}$$

In fact, if $|\eta| < 1$, the overlap between the wave functions $|\Psi\rangle$ and $|\tilde{\Psi}\rangle$ decays exponentially with the length of the system and thus the state $|\Psi\rangle$ is not invariant under the symmetry operation. By using Eq. (2.2.35), the generalized transfer matrix becomes

$$T^{\Sigma^g}_{\alpha\bar{\alpha},\beta\bar{\beta}} = \sum_{i,j} \Sigma^g_{ij} \tilde{\Gamma}_{\alpha\beta}(j) \Gamma^*_{\bar{\alpha}\bar{\beta}}(i) \Lambda_\beta \Lambda_{\bar{\beta}} \tag{2.2.64}$$

$$= \mathrm{e}^{\mathrm{i}\theta_g} \sum_i (U_g^\dagger \tilde{\Gamma}(i) U_g)_{\alpha\beta} \Gamma^*_{\bar{\alpha}\bar{\beta}}(i) \Lambda_\beta \Lambda_{\bar{\beta}}. \tag{2.2.65}$$

Multiplying this equation by $U^\dagger_{g\beta\bar{\beta}}$, using

$$[\Lambda, U_g] = 0, \tag{2.2.66}$$

and taking the summation of β and $\bar{\beta}$, we can show

$$\sum_{\beta\bar{\beta}} T^{\Sigma^g}_{\alpha\bar{\alpha},\beta\bar{\beta}} U^\dagger_{g\beta\bar{\beta}} = \mathrm{e}^{\mathrm{i}\theta_g} U^\dagger_{g\alpha\bar{\alpha}}. \tag{2.2.67}$$

Therefore $U^\dagger_{g\beta\bar{\beta}}$ is the eigenstate with eigenvalue of modulus 1. Since the eigenvector of largest modulus is unique, we finally obtain

$$X_{\beta\bar{\beta}} = U^\dagger_{g\beta\bar{\beta}}. \tag{2.2.68}$$

That is, the matrix U_g is obtained by diagonalizing the transfer matrix T^{Σ^g} and choosing the largest eigenvector. As we vary the element g through the whole group G, we obtain the projective representation.

There is a relationship between the way how the edge states transform under the symmetry operation and how the symmetry operation acts on the Schmidt eigenstates [48]. We first show how an operator acts on the Schmidt eigenstates. We consider a bipartition of the system into a subsystem A and the subsystem B. The Schmidt decomposition of the ground-state wave function is given as

$$|\Psi\rangle = \sum_\alpha \mathrm{e}^{-\frac{E_\alpha}{2}} |\psi_\alpha\rangle_A |\phi_\alpha\rangle_B \tag{2.2.69}$$

and the reduced density matrix ρ_S of the subsystem A is

$$\rho_A = \mathrm{Tr}_B \left(|\Psi\rangle\langle\Psi|\right) = \mathrm{e}^{-H_\mathrm{E}}, \tag{2.2.70}$$

where H_E is the entanglement Hamiltonian. We focus on the low-lying entanglement states $|\psi_\alpha\rangle_A$ with $E_\alpha < E_\mathrm{cutoff}$ where E_cutoff is a certain cutoff constant. In a gapped system with a finite correlation length ξ, they cannot be distinguished from each other by an operator $\mathcal{O}_A$ acting on sites far enough from the edge of the subsystem A [48]:

$$\langle \mathcal{O}_A \rangle_{\psi_\alpha} \simeq \langle \mathcal{O}_A \rangle_\Psi. \tag{2.2.71}$$

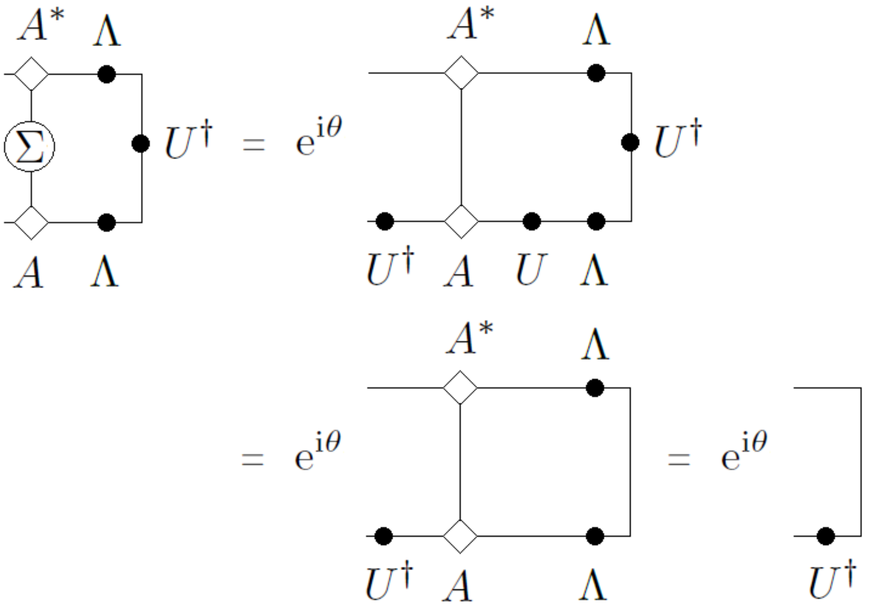

Figure2.2.9 Diagrammatic representation of the generalized transfer matrix and the symmetry operation to the MPS. The generalized transfer matrix has a right eigenvector $U^\dagger$.

On the other hand, an operator near the edge of the subsystem A acts non-trivially on the low-lying entanglement states. By acting the symmetry operator V_g ($g \in G$) on them, we obtain

$$V_g \simeq V_g^L V_g^R, \tag{2.2.72}$$

which is called the symmetry fractionalization. These effective operators V_g^L and V_g^R which encode how the Schmidt eigenstates transform under the symmetry operator are exponentially localized near the edge of the subsystem A on the length scale ξ. In the thermodynamic limit, the operators $\{V_g^L\}$ and $\{V_g^R\}$ do not have an overlap. As we vary g through the group G, we obtain sets of operators $\{V_g^L, V_h^L, \dots\}$ and $\{V_g^R, V_h^R, \dots\}$. The set has the same group structure as the group G up to a phase factor

$$V_g^L V_h^L = \rho(g,h) V_{gh}^L, \quad V_g^R V_h^R = \rho(g,h)^{-1} V_{gh}^R. \tag{2.2.73}$$

This is a projective representation of the group G with a factor system $\rho(g,h)$. Thus the Schmidt states transform projectively under the symmetry transformation. Although the matrices $\{U_g\}$ and operators $\{V_g\}$ may not be the same up to a phase, their factor system is identical [48]. We see examples of the symmetry fractionalization in Sec. 2.3.2.

2.3 Fermion model

In the previous section, we have shown how to classify the bosonic SPT phases. In this section, we consider some SPT phases and characterize them. In Sec. 2.3.1, we introduce the Kitaev model of spinless p-wave superconductor [20] and see its topological properties. Through the non-local Jordan–Wigner transformation [120,121], this fermion model is related to a spin model. In Sec. 2.3.2, we show some fermion and spin models and study them from the symmetry point of view. In Sec. 2.3.3, we introduce the Majorana fermions and how they emerge in the system of spinless fermions. In Sec. 2.3.4, we derive non-local correlation functions which characterize the topological phases. In the following, the number of sites is denoted by N, and the Pauli matrices satisfy $\sigma^\alpha_{N+1} = \sigma^\alpha_1$, $\sigma^\alpha_{N+2} = \sigma^\alpha_2$ $(\alpha = x, y, z)$ for the periodic boundary condition, and $\sigma^\alpha_{N+1} = \sigma^\alpha_{N+2} = 0$ $(\alpha = x, y, z)$ for the open boundary condition.

2.3.1 Topological superconductor

We study a model of spinless p-wave superconductor in one dimension. This model is one of the simplest models which exhibit topological phases hosting the Majorana edge modes. The Majorana fermion is a particle that is identical to its own antiparticle [122]. For the review of Majorana fermions and topological superconductors, see e.g., Ref. [63].

We first consider the continuum model and study its topological properties. The model is defined as

$$H_{p-\mathrm{wave}} = \int dx \left[\Psi^\dagger(x)\xi_k\Psi(x) + \Delta\left(\Psi^\dagger(x)\partial_x\Psi^\dagger(x) + \mathrm{h.c.}\right)\right], \tag{2.3.1}$$

where operator $\Psi(x)$ $(\Psi(x)^\dagger)$ annihilates (creates) a spinless fermion at position x, Δ is the strength of p-wave pairing (assumed to be real), and

$$\xi_k = \frac{k^2}{2m} - \mu \tag{2.3.2}$$

is the dispersion of the normal state with the mass m and the chemical potential μ. In reciprocal space with wave number k, the Hamiltonian has the form of the Bogoliubov–de Gennes Hamiltonian

$$H_{\mathrm{BdG}} = \begin{pmatrix} \xi_k & -\mathrm{i}\Delta k \\ \mathrm{i}\Delta k & -\xi_k \end{pmatrix} = \xi_k\tau^z + \Delta k\tau^y, \tag{2.3.3}$$

where τ denotes the Pauli matrices acting on particle-hole space

$$\begin{pmatrix} \Psi(x) \\ \Psi(x)^\dagger \end{pmatrix}. \tag{2.3.4}$$

We can easily diagonalize the Bogoliubov–de Gennes Hamiltonian and obtain the energy spectrum as

$$E_k = \pm\sqrt{\xi_k^2 + \Delta^2 k^2}. \tag{2.3.5}$$

We determine the critical points from the energy spectrum. For finite pairing Δ, the spectrum is gapless when $\xi_{k=0} = 0$, i.e., when $\mu = 0$. Otherwise, the system becomes gapped when $\mu \geq 0$. Thus the line $\mu = 0$ and line with $\Delta = 0$ for $\mu \geq 0$ indicate the phase transition.

To characterize the phases separated by the critical points, we rewrite the Hamiltonian as

$$H_{\text{BdG}} = \mathbf{b}_k \cdot \tau, \quad \mathbf{b}_k = (b_k^x, b_k^y, b_k^z) = (0, \Delta k, \xi_k). \tag{2.3.6}$$

The vector $\mathbf{b}_k$ can be considered as an effective Zeeman field acting in the particle-hole space. By defining a unit vector as $\hat{\mathbf{b}}_k = \frac{\mathbf{b}_k}{|\mathbf{b}_k|}$, we can consider the mapping from the reciprocal space to the unit vector as

$$k \to \hat{\mathbf{b}}_k. \tag{2.3.7}$$

In the absence of the matrix τ^x in the Hamiltonian, the unit vector $\hat{\mathbf{b}}_k$ is on the unit circle in the yz-plane and defines a map between one unit circle (the Brillouin zone) and another. Thus we can define the winding number which counts how many times the image winds around the circle. Let us calculate it for the model (2.3.1). When $\mu < 0$, the unit vector $\hat{\mathbf{b}}_k$ always stays in the upper half of the yz-plane, giving zero winding number. When $\mu > 0$, on the other hand, both b_y and b_z change their sign as we vary the wave number k. In fact, the unit vector $\hat{\mathbf{b}}_k$ winds once around the circle and we have the winding number ±1 depending on the sign of pairing Δ. Thus we can characterize the phases by the winding number. The phases with finite winding numbers are called topological and that with zero winding number is called trivial.

Let us consider the Hamiltonian from the view point of the topological classification [125–128]. In the absence of the matrix τ^x in the Hamiltonian H_k, we have

$$\{\tau^x, H_k\} = 0 \tag{2.3.8}$$

and the model belongs to the topological class BDI with the topological index $\mathbb{Z}$ [127, 128]. Note that if the matrix τ^x is present, the model belongs to the topological class D with the topological index $\mathbb{Z}_2$. We will study the topological phases from the view point of symmetry in Sec. 2.3.2.

As we have seen above, there is a phase transition between the trivial phase and the topological phases as we vary the chemical potential from negative to positive with finite pairing Δ. We introduce a domain wall between the trivial phase and the topological phase by spatially varying chemical potential

$$\mu(x) = \alpha x. \tag{2.3.9}$$

Because the excitation gap vanishes at the domain wall $x = 0$ and increase away from it, we could expect that there are bound states near it. In the following, we shall actually see that zero-energy mode appears as the bound state, which turns out to be a Majorana quasiparticle.

Let us explicitly construct the bound state [88]. In the calculation, we assume $\Delta > 0$ and $\alpha > 0$. For sufficiently smooth domain wall, we can neglect the kinetic term $\frac{k^2}{2m}$ in H_{BdG} (2.3.3) because the relevant momentum is small. Then the Hamiltonian (2.3.3) is written as

$$H_{BdG} = -\alpha x \tau^z + \Delta \frac{1}{\mathrm{i}} \frac{\partial}{\partial x} \tau^y. \tag{2.3.10}$$

Squaring it, we obtain

$$\begin{aligned} H^2 &= (\alpha x)^2 + (\Delta \frac{1}{\mathrm{i}} \frac{\partial}{\partial x})^2 - \Delta\alpha [x, \frac{1}{\mathrm{i}} \frac{\partial}{\partial x}] \tau^z \tau^y && (2.3.11) \\ &= (\alpha x)^2 + (\Delta \frac{1}{\mathrm{i}} \frac{\partial}{\partial x})^2 - \Delta\alpha \tau^x. && (2.3.12) \end{aligned}$$

The first two terms are the Hamiltonian of a harmonic oscillator, which is easily solved. Therefore the energy spectrum is given as

$$(E_n^{\pm})^2 = 2\Delta\alpha(n + \frac{1}{2}) \mp \Delta\alpha. \tag{2.3.13}$$

We can see that there is a zero-energy mode E_0^+ with the eigenstate

$$u_0(x) \begin{pmatrix} 1 \\ 1 \end{pmatrix}, \tag{2.3.14}$$

where u_0 is the Gaussian wave function of the ground state of the harmonic oscillator that is localized around $x = 0$. Thus the operator

$$\gamma = \int dx u_0(x) [\Psi(x) + \Psi^\dagger(x)] \tag{2.3.15}$$

is associated to a quasiparticle with zero energy localized near the domain wall $x = 0$. As we clearly see, the operator satisfies the Majorana condition [122]

$$\gamma = \gamma^\dagger. \tag{2.3.16}$$

Next we consider a finite system in the topological phase with the open boundary condition. The ends of the system can be considered as domain walls between the topological phase and the trivial phase (vacuum). Thus there are two Majorana bound states, say γ_1 and γ_2, localized at the ends of the system. They form a fermion operator that creates a zero-energy excited state, which is called the Majorana zero mode, in a non-local way as

$$c = \frac{\gamma_1 + \mathrm{i}\gamma_2}{2}. \tag{2.3.17}$$

Because this fermion mode can be occupied or empty, the ground states are two fold degenerate. Since the non-local property of the Majorana zero mode, it is robust against local perturbation and is stable until the energy gap closes.

In the following sections, we consider the following lattice version of the chain, called the Kitaev model [20], of spinless p-wave super conductor

$$H_{\text{Kitaev}} = \sum_{i=1}^{N} \left[-t(c_i^\dagger c_{i+1} + c_{i+1}^\dagger c_i) - (\Delta c_i^\dagger c_{i+1}^\dagger + \Delta c_{i+1} c_i) - \mu c_i^\dagger c_i \right]. \tag{2.3.18}$$

$$\tag{2.3.19}$$

Here the operator c_i ($c_i^\dagger$) annihilates (creates) a spinless fermion at site i, t is the hopping amplitude, and Δ stands for the strength of the p-wave pairing, and the μ is the chemical potential. In Secs. 2.3.2-2.3.4, we study the topological properties in detail.

2.3.2 Related models

In the previous section, we have introduced fermion models in one dimension. It is well known that the fermion models are equivalent to the spin (boson) models in one dimension [121,123,124]. By explicitly mapping to the corresponding spin models, we study the relation between the physical properties of the fermion models and that of the spin models. In the following, we investigate the topological properties of the models which we will study in Chapters 4 and 5.

First we consider the Kitaev model of spinless p-wave superconductor [20]. For simplicity, we set $t = \Delta = 1$ and $\mu = 2\lambda$ in Eq. (2.3.18), assume $\mu > 0$, and consider the following model

$$H_{\text{Kitaev}} = -\sum_{i=1}^{N} \left[(c_i^\dagger - c_i)(c_{i+1}^\dagger + c_{i+1}) + 2\lambda c_i^\dagger c_i \right] \tag{2.3.20}$$

$$= -\sum_{i=1}^{N} (c_i^\dagger c_{i+1} + c_{i+1}^\dagger c_i + c_i^\dagger c_{i+1}^\dagger + c_{i+1} c_i + 2\lambda c_i^\dagger c_i). \tag{2.3.21}$$

Here, $c_{i+1}^\dagger c_i$, $c_i^\dagger c_{i+1}$) are the hopping terms, $c_{i+1} c_i$ ($c_i^\dagger c_{i+1}^\dagger$) is the pairing term which annihilates (creates) two fermions, and $c_i^\dagger c_i$ is a chemical potential term. The Hamiltonian commutes with the parity operator

$$P = (-1)^{\sum_{i=1}^{N} c_i^\dagger c_i}, \tag{2.3.22}$$

and thus the total number of fermions modulo 2 is preserved. From $P^2 = 1$, we get $P = \pm 1$. We can obtain the energy dispersion by performing the Fourier transformation followed by the Bogoliubov transformation (App. B) as

$$\epsilon(k) = 2\sqrt{(\cos k + \lambda)^2 + \sin^2 k} \qquad (-\pi < k \leq \pi). \tag{2.3.23}$$

The energy gap closes at the critical point $\lambda = 1$. Depending on the coupling constant λ, there appear two distinct phases. For $0 < \lambda < 1$, the ground state is topological. As we will see in Sec. 2.3.3, the Majorana zero mode appears at the ends of the system and the ground states are two-fold degenerate in this range of λ. For $\lambda > 1$, on the other hand, the ground state is in a trivial phase and unique.

Let us consider this model in the spin representation. The Kitaev model H_{Kitaev} is transformed by the Jordan–Wigner transformation (App. C) [120, 121]

$$c_i = \prod_{j=1}^{i-1}(-\sigma_j^z)\sigma_i^-, \quad c_i^\dagger = \prod_{j=1}^{i-1}(-\sigma_j^z)\sigma_i^+ \tag{2.3.24}$$

into the transverse-field Ising model [108, 109]

$$H_{\text{TFIM}} = -\sum_{i=1}^{N}(\sigma_i^x\sigma_{i+1}^x + \lambda\sigma_i^z). \tag{2.3.25}$$

Here σ_i is the Pauli matrix at site i. By the Jordan–Wigner transformation, the fermion parity is mapped to the on-site $\mathbb{Z}_2$ symmetry

$$\sigma_i^x \to P\sigma_i^x P = -\sigma_i^x \tag{2.3.26}$$

generated by

$$P = \prod_{i=1}^{N}\sigma_i^z. \tag{2.3.27}$$

The model H_{TFIM} shows a quantum phase transition at $\lambda = 1$. For $0 < \lambda < 1$, the ground state shows the ferromagnetic phase which breaks the on-site $\mathbb{Z}_2$ symmetry with local magnetization $\langle\sigma_i^x\rangle$ as the order parameter. The ground states are two-fold degenerate and they are mapped to each other by the $\mathbb{Z}_2$ symmetry operator P. For $1 < \lambda$, on the other hand, the ground state is in the paramagnetic phase which does not break any symmetry.

The ground states of the fermion model (2.3.20) are related to that of the spin model (2.3.25) in the following way. For $0 < 1 < \lambda$, let the two symmetry-broken ground states of the spin model be $|\Psi_1\rangle$ and $|\Psi_2\rangle$, and $|\Psi_1^{\text{f}}\rangle$ and $|\Psi_2^{\text{f}}\rangle$ be the corresponding states in the fermion model. Provided that the fermion parity is not broken in the ground state of H_{Kitaev}

(2.3.20), $|\Psi^{\mathrm{f}}_1\rangle$ and $|\Psi^{\mathrm{f}}_2\rangle$ are not the proper eigenstates of H_{Kitaev} because they are not the eigenstates of the parity operator P. Instead, the cat states

$$|\tilde{\Psi}^{\mathrm{f}}_1\rangle = \frac{|\Psi^{\mathrm{f}}_1\rangle + |\Psi^{\mathrm{f}}_2\rangle}{\sqrt{2}}, \quad |\tilde{\Psi}^{\mathrm{f}}_2\rangle = \frac{|\Psi^{\mathrm{f}}_1\rangle - |\Psi^{\mathrm{f}}_2\rangle}{\sqrt{2}} \tag{2.3.28}$$

are the correct ground states with even and odd parity, respectively. Therefore, the non-trivial entanglement of the topological phases of the fermion model (2.3.20) is understood as that of cat states in the spin model (2.3.25). For $1 < \lambda$, on the other hand, the unique ground state with on-site $\mathbb{Z}_2$ symmetry of the spin model is correctly mapped to the fermion ground state with the fermion parity symmetry.

Let us see the Kitaev model from the view point of symmetry [125–128]. As we have seen, the model has the parity symmetry P. If we only have the parity symmetry, the model belongs to the class D with $\mathbb{Z}_2$ invariant [20] and there are only two phases. In addition to this symmetry, however, the Kitaev model has a time-reversal symmetry T which is the complex conjugation operator for the spinless fermions

$$c_i \to c_i, \quad c^\dagger_i \to c^\dagger_i. \tag{2.3.29}$$

Imposing both P and T symmetries, the model belongs to the class BDI [103]. Now the topological number is $\mathbb{Z}$ and counts the number of the Majorana zero modes. Note that in the presence of the interaction, there are only eight distinct phases, labeled by $\mathbb{Z}_8$. These topological invariants are constructed from the symmetry fractionalization of the symmetries P and T [48, 103, 129].

Next let us consider the fermion model with next-nearest hopping and pairing terms [130]

$$H_{\mathrm{C}} = \sum_{i=1}^{N} J^{XZX}(c^\dagger_i - c_i)(c^\dagger_{i+2} + c_{i+2}) \tag{2.3.30}$$

$$= \sum_{i=1}^{N} J^{XZX}(c^\dagger_i c_{i+2} + c^\dagger_{i+2} c_i - c_i c_{i+2} - c^\dagger_{i+2} c^\dagger_i). \tag{2.3.31}$$

This is a model of p-wave superconductor with next nearest couplings which belongs to the class BDI. The longer-range couplings introduce topologically nontrivial effects because the number of Majorana zero modes at the ends of the system may change. This model is transformed into a spin model as in the case of the Kitaev model:

$$H_{\mathrm{C}} = -\sum_{i=1}^{N} J^{XZX} \sigma^x_i \sigma^z_{i+1} \sigma^x_{i+2}. \tag{2.3.32}$$

This model is called the cluster model in one dimension [131]. In the following, we assume that J^{XZX} is positive.

The cluster model has attracted much attention in statistical physics, condensed-matter physics, and quantum-information science [131–140]. In the early stage of its studies, the one-dimensional cluster model and its variants were investigated as an example of a series of one-dimensional spin models that can be exactly solved by mapping to free fermions [131]. Looked upon as fermion models, this class of models may be thought of as one-dimensional p-wave superconductors with longer-range hopping and pairing including the Kitaev model [20]. The ground state of the cluster model, called the cluster state, possesses topological properties, e.g., the existence of the edge modes and hidden order detected by the string order parameters, as we will see below [133, 134]. In quantum-information science, the one-way quantum computation and the measurement-based quantum computation using the cluster state have been proposed [135–137]. The cluster state can be used to implement them since a highly entangled state must be prepared for the resource state [137]. Motivated by these proposals, extensive research has been done various aspect of on the cluster model such as the entanglement properties [132, 134] and the robustness of the cluster state against thermal excitations or randomness [137,138]. In addition, the one-dimensional cluster model is expected to be realized in experiments using cold atoms on a zigzag ladder by introducing three-spin exchange interaction [139].

From now, we show that the cluster state belongs to an SPT phase protected by $\mathbb{Z}_2 \times \mathbb{Z}_2$ symmetry, called the cluster phase [133]. Here we assume that the system size N is even. The model is symmetric under the on-site π-rotation around the z-axis at odd sites

$$P_1 = \prod_{i \in \mathrm{odd}} \sigma_i^z \tag{2.3.33}$$

and that at even sites

$$P_2 = \prod_{i \in \mathrm{even}} \sigma_i^z, \tag{2.3.34}$$

which are commuting

$$[P_1, P_2] = 0 \tag{2.3.35}$$

and form the group $\mathbb{Z}_2 \times \mathbb{Z}_2$. In the fermion language, the operators P_1 and P_2 correspond to the fermion parity operators at odd and even sites respectively. The three-site interaction in Eq. (5.1.4)

$$K_i = \sigma_{i-1}^x \sigma_i^z \sigma_{i+1}^x \tag{2.3.36}$$

is called the cluster interaction or the cluster stabilizer in quantum-information science. The stabilizers commute with each other

$$[K_i, K_j] = 0 \tag{2.3.37}$$

and thus the cluster state $|\psi\rangle$ is given by the eigenstate of them

$$|\psi\rangle = K_i|\psi\rangle \tag{2.3.38}$$

with $i = 1, \ldots, N$ for the periodic boundary condition and $i = 2, \ldots, N-1$ for the open boundary condition. For the periodic boundary condition, the ground state is unique. For the open boundary condition, there are edge operators that commute with the Hamiltonian and they give the ground-state degeneracy as we will see below.

We explicitly construct the edge operators for the open boundary condition. To get them, we consider how the symmetry operators in Eqs. (2.3.33) and (2.3.34) act on the ground state. By multiplying $K_i = 1$ for odd i (=3, 5, …, N-1),

$$1 = \prod_{i\in\mathrm{odd}} K_i = \sigma_2^x\sigma_3^z \cdots \sigma_{N-1}^z\sigma_N^x \tag{2.3.39}$$

$$= \sigma_2^x\sigma_1^z P_1\sigma_N^x, \tag{2.3.40}$$

we obtain

$$P_1 = \sigma_1^z\sigma_2^x\sigma_N^x = P_1^L P_1^R. \tag{2.3.41}$$

Here we have defined the operators P_1^L and P_1^R acting on the left and right edges of the system as

$$P_1^L = \sigma_1^z\sigma_2^x, \quad P_1^R = \sigma_N^x, \quad [P_1^L, P_1^R] = 0, \quad (P_1^L)^2 = (P_1^R)^2 = 1, \tag{2.3.42}$$

implying that the $\mathbb{Z}_2$ generated by P_1 fractionalizes into the two $\mathbb{Z}_2$ operators P_1^L and P_1^R. This is an example of the symmetry fractionalization in Sec. 2.2.4. By a similar calculation for the even sites,

$$1 = \prod_{i\in\mathrm{even}} K_i = \sigma_1^x\sigma_2^z \cdots \sigma_{N-2}^z\sigma_{N-1}^x \tag{2.3.43}$$

$$= \sigma_1^x P_2\sigma_N^z\sigma_{N-1}^x, \tag{2.3.44}$$

we see that the second $\mathbb{Z}_2$ generated by P_2 fractionalizes into the two $\mathbb{Z}_2$ pieces P_2^L and P_2^R:

$$P_2 = \sigma_1^x\sigma_{N-1}^x\sigma_N^z = P_2^L P_2^R, \tag{2.3.45}$$

where the operators P_2^L and P_2^R acting on the left and right edges are defined as

$$P_2^L = \sigma_1^x, \quad P_2^R = \sigma_{N-1}^x\sigma_N^z, \quad [P_2^L, P_2^R] = 0, \quad (P_2^L)^2 = (P_2^R)^2 = 1. \tag{2.3.46}$$

As we can easily show, the operators on the left (right) end of the system anticommute with each other

$$\{P_1^{L(R)}, P_2^{L(R)}\} = 0 \tag{2.3.47}$$

and commute with the Hamiltonian

$$[H_{\mathrm{C}}, P_1^{L(R)}] = 0, \quad [H_{\mathrm{C}}, P_2^{L(R)}] = 0. \tag{2.3.48}$$

The operators on different edges commute with each other

$$[P_1^L, P_2^R] = 0, \quad [P_2^L, P_1^R] = 0. \tag{2.3.49}$$

These operators are the edge operators we seek for.

The anticommutation relation of the edge operators P_1^L and P_2^L implies the ground-state degeneracy. In fact, they form the Pauli algebra and the free spin-$\frac{1}{2}$ degree of freedom at each end gives rise to two-fold degeneracy in the ground states. Note that though the symmetry fractionalization generally holds for the ground-state subspace, the edge operators commuting with the Hamiltonian (2.3.48) imply that all the energy levels are at least four-fold degenerate. Although adding to the cluster model (5.1.4) terms that respect the $\mathbb{Z}_2 \times \mathbb{Z}_2$ symmetry would change the form of the edge operators P_1^L and P_2^L, their mutual anticommutation relation does not smoothly change: from the commutation relation $P_1 P_2 = P_2 P_1$, we get

$$P_1^L P_2^L = \mathrm{e}^{\mathrm{i}\alpha} P_2^L P_1^L, \tag{2.3.50}$$

and from $(P_{1(2)}^L)^{\mathrm{T}} = P_{1(2)}^L$ and $(P_{1(2)}^L)^2 = 1$, we can show

$$\mathrm{e}^{\mathrm{i}\alpha} = \pm 1. \tag{2.3.51}$$

This labels the inequivalent projective representations of the group $\mathbb{Z}_2 \times \mathbb{Z}_2$. The case $\mathrm{e}^{\mathrm{i}\alpha} = -1$ occurs in the ground state of H_{C}. As long as the correlation length is finite, we can define the edge operators and get degenerate ground states whenever $P_{1(2)}^L$ and $P_{1(2)}^R$ belong to non-trivial projective representation ($\mathrm{e}^{\mathrm{i}\alpha} = -1$). Therefore, the cluster phase is an SPT phase protected by the $\mathbb{Z}_2 \times \mathbb{Z}_2$ symmetry.

2.3.3 Majorana representation

Topological nature of the Kitaev model is clearly seen in the Majorana representation [20]. We introduce the Majorana fermions on a one-dimensional chain with N sites. As shown in Fig. 2.3.1, we decompose the spinless fermions (black circles) into two Majorana fermions (yellow circles) at each sites: the two Majorana fermions are defined by real and imaginary parts of the spinless fermions at each site

$$\bar{c}_{2i-1} = c_i^\dagger + c_i, \quad \bar{c}_{2i} = \mathrm{i}\,(c_i - c_i^\dagger), \quad i = 1, 2, \dots, N. \tag{2.3.52}$$

The Majorana fermion operators are hermitian satisfying the Majorana condition

$$\bar{c}_i = \bar{c}_i^\dagger. \tag{2.3.53}$$

The standard anticommutataion relation of spinless fermions $\{c_i\}$ translates into the anti-commutation relation of the Majorana fermions $\{\bar{c}_i\}$

$$\{\bar{c}_i,\ \bar{c}_j\} = 2\delta_{ij}. \tag{2.3.54}$$

In this representation, the Kitaev model is written as [20]

$$H_{\text{Kitaev}} = -\sum_{i=1}^{N} \left[t(c_i^\dagger - c_i)(c_{i+1}^\dagger + c_{i+1}) + 2\lambda c_i^\dagger c_i \right] \tag{2.3.55}$$

$$= -\mathrm{i} \sum_{i=1}^{N} (t\bar{c}_{2i}\bar{c}_{2i+1} + \lambda \bar{c}_{2i}\bar{c}_{2i-1}). \tag{2.3.56}$$

For later convenience, we have recovered t. We show in Fig. 2.3.2 how the Majorana fermions interact with each other. The purple lines represent the on-site couplings $(\bar{c}_{2i-1}\bar{c}_{2i})$, and the red ones represent the nearest-neighbor couplings between neighboring sites $(\bar{c}_{2i}\bar{c}_{2i+1})$.

To see the topological properties, we consider two extreme cases: (i) $t = 1$, $\lambda = 0$ and (ii) $t = 0$, $\lambda = 1$. For the case (i), there are only red couplings in Fig. 2.3.2. By introducing new fermion operators

$$d_{i\backslash} = \frac{\bar{c}_{2i} + \mathrm{i}\bar{c}_{2i+1}}{2}, \tag{2.3.57}$$

we can rewrite the Hamiltonian as

$$H_{\text{Kitaev}} = \sum_{i=1}^{N-1} (d_{i\backslash}^\dagger d_{i\backslash} - 1). \tag{2.3.58}$$

Thus the vacuum of the fermion operators $\{d_{i\backslash}\}$ gives the ground states. Because the Hamiltonian does not contain the Majorana fermions $\bar{c}_1$ and $\bar{c}_{2N}$ which are localized at the left and right ends of the system respectively, we can construct the fermion operator for a zero-energy mode

$$Q = \frac{\bar{c}_1 + \mathrm{i}\bar{c}_{2N}}{2} \tag{2.3.59}$$

That does not change the eigenvalue of H_{Kitaev}. The two Majorana fermions localized at the ends of the system are combined in a non-local way to form a fermion with zero energy, which we call the Majorana edge mode or the Majorana zero mode. The total Hilbert space of H_{Kitaev} is spanned by the operators $\{d_{i\backslash}\}$ and Q. Thus the vacuum $|0\rangle$ of both $\{d_{i\backslash}\}$ and Q and the state $Q^\dagger|0\rangle$ are the degenerate ground states. This is the characteristic property of the topological phase of the Kitaev model. We can construct the edge mode for $0 < \lambda < 1$ as well. Using the method described in Sec. 3.1, we can numerically obtain the amplitudes of the localized Majorana fermions (see also App. D).

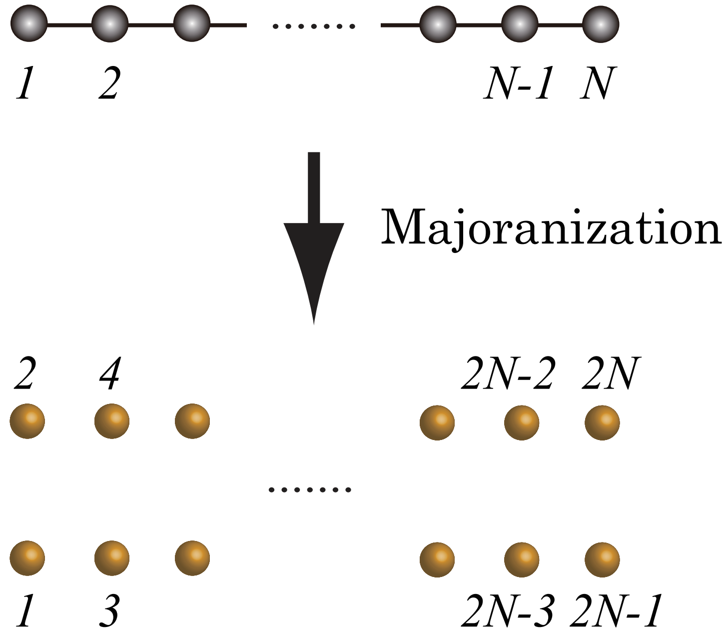

Figure2.3.1 Majorana representation: the spinless fermion c_i at site i is decomposed into two Majorana fermions $\bar{c}_{2i-1}$ and $\bar{c}_{2i}$ (yellow circles).

For the case (ii), on the other hand, there are only purple couplings shown in Fig. 2.3.2. By introducing new fermion operators

$$d_{i|} = \frac{\bar{c}_{2i} + \mathrm{i}\bar{c}_{2i-1}}{2}, \tag{2.3.60}$$

we can rewrite the Hamiltonian as

$$H_{\text{Kitaev}} = \sum_{i=1}^{N} (d_{i|}^{\dagger} d_{i|} - 1), \tag{2.3.61}$$

where all the Majorana fermions appear in the Hamiltonian. Thus the ground state is the vacuum of the fermion operators $\{d_{i|}\}$ and unique without edge modes.

We next study the Kitaev model in terms of fermion parity P in Eq. (2.3.22). Let us find an expression for P within the ground-state subspace. It has a form of

$$P = P^L P^R, \tag{2.3.62}$$

where the P^L and P^R are operators that act near the left and right ends of the system respectively. They satisfy

$$P^L P^R = \mathrm{e}^{\mathrm{i}\mu} P^R P^L \tag{2.3.63}$$

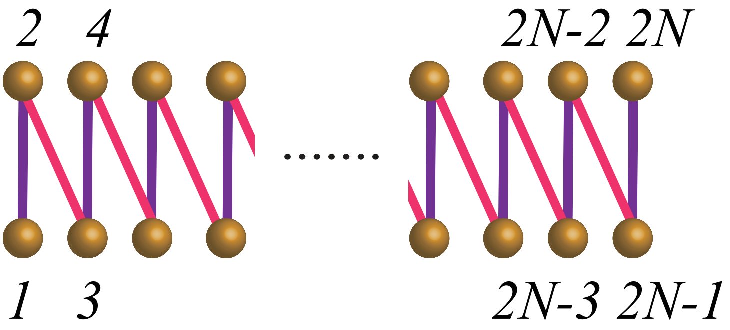

Figure2.3.2 The Majorana representation of the Kitaev model: two Majorana fermions connected by color lines interact. The purple lines are on-site couplings ($\bar{c}_{2i-1}\bar{c}_{2i}$), and red lines are nearest neighbor couplings ($\bar{c}_{2i}\bar{c}_{2i+1}$). When the couplings represented by the red lines are dominant ($0<\lambda<1$), the localizing Majorana edge mode appears near the ends of the system.

depending on how many operators they contain. For $t=1$, $\lambda=0$ (the case (i) above) we find

$$P^L=\bar{c}_1, \quad P^R=\bar{c}_{2N}. \tag{2.3.64}$$

They are the operators localizing near ends and satisfy anticommutation relation

$$\{P^L,P^R\}=0. \tag{2.3.65}$$

Thus we obtain $\mu=\pi$. In this case, the Majorana edge operator Q in Eq. (2.3.59) anticommute with the parity operator P

$$\{Q,P\}=0. \tag{2.3.66}$$

Since the Hamiltonian commute with both the edge operator and the parity operator

$$[H,Q]=0, \quad [H,P]=0, \tag{2.3.67}$$

we have two degenerate ground states with different parity.

Next we consider a model of the p-wave superconductor with next-nearest hopping and pairing terms. The Hamiltonian H_{C} [Eq. (2.3.30) in the fermion representation and Eq. (5.1.4) in the spin representation] is written by using the Majorana fermion $\{\bar{c}_i\}$ as

$$H_{\mathrm{C}}=\mathrm{i}\sum_{i=1}^{N}J^{XZX}\bar{c}_{2i}\bar{c}_{2i+3}. \tag{2.3.68}$$

We show the couplings of the Majorana fermion in Fig. 2.3.3(a). For the periodic boundary condition, all the Majorana fermions connected by the red lines are paired with each other, and the ground state is unique. For the open boundary condition, on the other hand, there are two unpaired Majorana fermions which do not appear in the Hamiltonian at each end of the system. These unpaired Majorana fermions $\{\bar{c}_1\bar{c}_3,\bar{c}_{2N-2},\bar{c}_{2N}\}$ form fermions so that

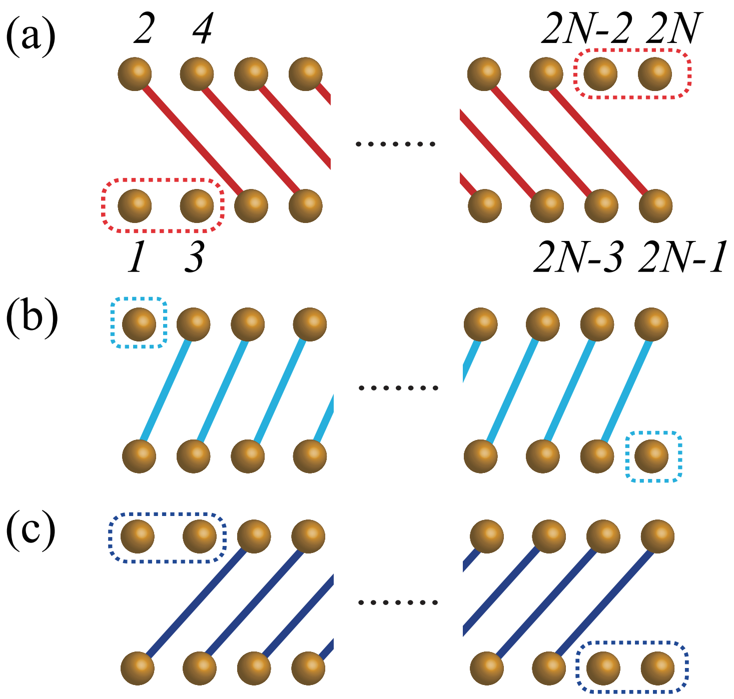

Figure2.3.3 (a)-(c) Schematic representation of the interactions by the Majorana language. (a), (b), and (c) depict the first, second, and third terms of the Hamiltonian in Eq. (2.3.69). Non-interacting Majorana fermions enclosed in dotted line appear at the ends of the system. (Figure taken from Ref. [92].)

the ground states are the eigenstate of the parity operators P_1 and P_2 [Eqs. 2.3.33 and 2.3.34]. For the Hamiltonian H_{C} which possesses the time-reversal symmetry and belongs to the topological class BDI, they form two Majorana zero modes in a non-local way and the ground states are four-fold degenerate (local pairing is forbidden in the presence of the time-reversal symmetry).

In Chapter 4, we study the quantum phase transitions of a generalized Kitaev model with several types of interactions that preserves the fermion parity. The Hamiltonian in the spin representation contains the Ising interactions and cluster interactions

$$H = \sum_{i=1}^{N} (-J^{XZX} \sigma_i^x \sigma_{i+1}^z \sigma_{i+2}^x + J^{YY} \sigma_i^y \sigma_{i+1}^y + J^{YZY} \sigma_i^y \sigma_{i+1}^z \sigma_{i+2}^y).$$

In the Majorana representation, the Hamiltonian is written as

$$H = \mathrm{i} \sum_{i=1}^{N} (J^{XZX} \bar{c}_{2i} \bar{c}_{2i+3} - J^{YY} \bar{c}_{2i-1} \bar{c}_{2i+2} + J^{YZY} \bar{c}_{2i-1} \bar{c}_{2i+4}). \tag{2.3.69}$$

Each term is schematically shown in Fig. 2.3.3.

2.3.4 String correlation function

In Sec. 2.3.3, we have seen that the topological phases of the Kitaev model and the cluster model are characterized by the number of the Majorana zero modes. These phases are also characterized by the non-local string order parameters [4, 133, 134]. In this section, we construct the string order parameters by using non-local transformations.

We first construct the string order parameter for the topological phase of the Kitaev model (2.3.20). The corresponding spin phase is the conventional ferromagnetic phase and thus characterized by the ferromagnetic correlation function of distance L

$$O_{XX}(L) = \langle \sigma_1^x \sigma_L^x \rangle. \tag{2.3.70}$$

By mapping back to the fermion model by the non-local Jordan–Wigner transformation, we obtain the non-local correlation function for the topological phase of the Kitaev model

$$O_{XX}(L) = \left\langle \prod_{i=1}^{L-1} \bar{c}_{2i} \bar{c}_{2i+1} \right\rangle. \tag{2.3.71}$$

Next we construct the string order parameter for the cluster phase by a duality transformation. We consider the cluster-Ising model [134]

$$H(\lambda) = \sum_{i=1}^{N} (-\sigma_i^x \sigma_{i+1}^z \sigma_{i+2}^x + \lambda \sigma_i^y \sigma_{i+1}^y) \tag{2.3.72}$$

for the open boundary condition. When the cluster interactions are dominant, the ground state is in the topological phase. When the Ising interactions are dominant, on the other hand, the ground state is in the (anti)ferromagnetic phase characterized by conventional local order parameters. This model has the same duality (Kramers–Wannier duality) as the transverse-field Ising model. That is, by the non-local transformation

$$\mu_i^z = \sigma_i^x \sigma_{i+1}^x, \quad \mu_i^x = \prod_{j=1}^{i} \sigma_j^z, \quad \mu_i^y = \mathrm{i} \mu_i^x \mu_i^z, \quad \sigma_{N+1}^x = 1, \tag{2.3.73}$$

we obtain the following relations

$$-\sigma_i^x \sigma_{i+1}^z \sigma_{i+2}^x = \mu_i^y \mu_{i+1}^y, \quad \sigma_i^y \sigma_{i+1}^y = -\mu_{i-1}^x \mu_i^z \mu_{i+1}^x, \quad \mu_0^x = 1. \tag{2.3.74}$$

Therefore the Hamiltonian has the following duality [134]

$$H^{\mathrm{dual}}(\lambda) = \lambda H\left(\frac{1}{\lambda}\right). \tag{2.3.75}$$

Table2.3.1 The relation between correlation functions which characterize the ground states of the models. Correlation function for each phase is shown. The local correlation function is mapped to the non-local correlation function by the non-local transformation.

Model	Two-point function	Non-local transformation	Non-local correlation function
Kitaev chain	Ferromagnetic (2.3.70)	Jordan–Wigner transformation (2.3.24)	Eq. (2.3.71)
Cluster-Ising model	Antiferromagnetic (2.3.76)	Kramers–Wannier duality (2.3.73)	Eq. (2.3.77)

The critical point $\lambda = 1$ is where the Hamiltonian is self-dual. The antiferromagnetic phase in the μ-spin representation is characterized by the local correlation function of distance L

$$O_{XZX}(L) = (-1)^L \left\langle \mu_1^y \mu_{L-1}^y \right\rangle . \tag{2.3.76}$$

By mapping back to the σ-spin representation, we obtain the string correlation function

$$O_{XZX}(L) = (-1)^L \left\langle \sigma_1^x \sigma_2^y \left(\prod_{j=3}^{L-2} \sigma_j^z \right) \sigma_{L-1}^y \sigma_L^x \right\rangle . \tag{2.3.77}$$

This function converges to a finite value in the long distance limit [134]. We call the infinite distance limit

$$O_{XZX} = \lim_{L\to\infty} O_{XZX}(L) \tag{2.3.78}$$

as the string order parameter. As in the case for the string correlation function of the Haldane phase [6] (see also App. A), the local correlation function [Eqs. (2.3.70) and (2.3.76)] becomes the non-local correlation function [Eqs. (2.3.71) and (2.3.77)], respectively by the non-local transformation [Eqs. (2.3.24) and (2.3.73)]. Table 2.3.1 summarizes the relationship between these models and correlation functions.

We introduce another model which shows topological phase and construct the string correlation function. We call the model obtained by applying the π rotation around z-axis to the cluster interaction K_i

$$H_{\mathrm{C}^*} = \sum_{i=1}^{N} \sigma_i^y \sigma_{i+1}^z \sigma_{i+2}^y \tag{2.3.79}$$

the dual cluster model. The ground states of the model are in a topological phase which we call the dual cluster phase, and are four-fold degenerate as in the cluster model. Thus the model

$$H(\lambda) = \sum_{i=1}^{N} (-\sigma_i^x \sigma_{i+1}^z \sigma_{i+2}^x + \lambda\, \sigma_i^y \sigma_{i+1}^z \sigma_{i+2}^y) \tag{2.3.80}$$

is apparently self-dual by the transformation which rotates it by angle π around z-axis. The string correlation function of the dual cluster model is obtained by applying this transformation to that of the cluster model as

$$O_{YZY}(L) = \left\langle \sigma_1^y \sigma_2^x \left(\prod_{j=3}^{L-2} \sigma_j^z \right) \sigma_{L-1}^x \sigma_L^y \right\rangle . \tag{2.3.81}$$

Chapter3

Methods

This chapter contains the methods we use for the analysis in Chapters 4 and 5. In Sec. 3.1, we explain the exact diagonalization method for Hamiltonians of non-interacting spinless fermions. We then detail the method to calculate the entanglement properties and the correlation functions. In Sec. 3.2, we explain the time-dependent Bogoliubov theory to study the dynamics. In Sec. 3.3, we describe the another method to obtain the ground states of infinite-size systems and the corresponding physical quantities basing on the MPS as shown in Sec. 2.2.

3.1 Exact diagonalization

In Sec. 3.1.1, we show the exact diagonalization method of free fermion model following the argument of Lieb–Schultz–Mattis [121]. Using this method, we calculate the entanglement quantities and the correlation functions in Sec. 3.1.2 and Sec. 3.1.3, respectively.

3.1.1 Bogoliubov transformation

In the following, we consider the following generic quadratic Hamiltonian of the spinless fermions $\{c_i\}$ defined on an N-site lattice:

$$H = \sum_{i,j=1}^{N} \left[c_i^\dagger A_{ij} c_j + \frac{1}{2} \left(c_i^\dagger B_{ij} c_j^\dagger + c_i B_{ji} c_j \right) \right] \tag{3.1.1}$$

where $c_i (c_i^\dagger)$ is the creation (annihilation) operator of fermion at the i-th site, A is a real symmetric matrix of order N, and B is a real antisymmetric matrix of the same size. In the model to be considered in Chapter 4, the matrix elements of A and B are given by $A_{i,i+1} = A_{i+1,i} = J^{YY}$, $A_{i,i+2} = A_{i+2,i} = J^{XZX} - J^{YZY}$, $B_{i,i+1} = -B_{i+1,i} = -J^{YY}$, $B_{i,i+2} = -B_{i+2,i} = J^{XZX} + J^{YZY}$, and 0 otherwise. The coupling constants may depend on site i as we will see in Chapter 5.

We exactly diagonalize the Hamiltonian (3.1.1) as [121]

$$H = \sum_{\mu=1}^{N} E_\mu \left(\eta_\mu^\dagger \eta_\mu - \frac{1}{2} \right), \quad E_\mu \geq 0 \tag{3.1.2}$$

by the Bogoliubov transformation:

$$\eta_\mu = \sum_{i=1}^{N} \left[\frac{\phi_{i\mu} + \psi_{i\mu}}{2} c_i + \frac{\phi_{i\mu} - \psi_{i\mu}}{2} c_i^\dagger \right]. \tag{3.1.3}$$

The matrices ϕ and ψ of order N are solutions of the following simultaneous equations and orthogonal:

$$\begin{cases} E_\mu \psi_{i\mu} = \displaystyle\sum_{j=1}^{N} (A+B)_{ij} \phi_{j\mu}, & \text{(3.1.4a)} \\ E_\mu \phi_{i\mu} = \displaystyle\sum_{j=1}^{N} (A-B)_{ij} \psi_{j\mu}. & \text{(3.1.4b)} \end{cases}$$

Here, the eigenenergies $\{E_\mu\}$ in Eq. (3.1.2) are labeled in ascending order; $E_1 \leq E_2 \leq \cdots \leq E_N$. We call the Bogoliubov quasiparticle as the bogolons. The details of the Bogoliubov transformation are given in App. B. We define the Bogoliubov vacuum $|\mathrm{vac}\rangle$ of the Bogoliubov operators $\{\eta_\mu\}$ as

$$\eta_\mu |\mathrm{vac}\rangle = 0, \quad \mu = 1, \ldots, N. \tag{3.1.5}$$

Obviously, it is a ground state of the Hamiltonian (3.1.2). The excited states are obtained by applying the Bogoliubov creation operators to the vacuum. For example, the excited state with a single bogolon is given by

$$\eta_\mu^\dagger |\mathrm{vac}\rangle. \tag{3.1.6}$$

When one of the bogolons has zero energy, $E_1 = 0$ for example, the excited state

$$\eta_0^\dagger |\mathrm{vac}\rangle \tag{3.1.7}$$

is also a ground state. In this case, the ground states are at least two-fold degenerate.

3.1.2 Entanglement of free fermion

The entanglement properties of the fermion model are encoded in the Majorana correlations. In the Majorana representation,

$$\bar{c}_{2i-1} = c_i^\dagger + c_i, \quad \bar{c}_{2i} = \mathrm{i}\,(c_i - c_i^\dagger), \quad i = 1, 2, \ldots, N. \tag{3.1.8}$$

the Bogoliubov operators $\{\eta_\mu\}$ can be rewritten as

$$\eta_\mu = \frac{1}{2}\sum_{i=1}^{N}(\phi_{i\mu}\bar{c}_{2i-1} - i\psi_{i\mu}\bar{c}_{2i}). \tag{3.1.9}$$

Therefore $\phi_{i\mu}$ and $\psi_{i\mu}$ (the coefficients of the Bogoliubov transformation) are the amplitudes of the Majorana fermions at the i-th site in the μ-th bogolon excited state. Because the matrices ϕ and ψ are orthogonal, the columns $\{\phi_\mu\}$ ($\{\psi_\mu\}$) are orthogonal unit vectors. By the inverse transformation, the Majorana fermions $\{\bar{c}\}$ are given by

$$\begin{cases} \bar{c}_{2i-1} = \sum_{\mu=1}^{N} \phi_{i\mu}\left(\eta_\mu + \eta_\mu^\dagger\right), & \text{(3.1.10a)} \\ \bar{c}_{2i} = \mathrm{i}\sum_{\mu=1}^{N} \psi_{i\mu}\left(\eta_\mu - \eta_\mu^\dagger\right). & \text{(3.1.10b)} \end{cases}$$

It is then easy to calculate the expectation values of the Majorana operators in the vacuum:

$$\langle \bar{c}_{2i-1}\bar{c}_{2j-1}\rangle = \sum_{\mu=1}^{N} \phi_{i\mu}\phi_{j\mu} = \delta_{ij}, \tag{3.1.11}$$

$$\langle \bar{c}_{2i}\bar{c}_{2j}\rangle = \sum_{\mu=1}^{N} \psi_{i\mu}\psi_{j\mu} = \delta_{ij}, \tag{3.1.12}$$

$$\langle \bar{c}_{2i}\bar{c}_{2j-1}\rangle = -\langle \bar{c}_{2j-1}\bar{c}_{2i}\rangle = \mathrm{i}\sum_{\mu=1}^{N} \psi_{i\mu}\phi_{j\mu}. \tag{3.1.13}$$

Let us write the above equations in the matrix form:

$$\langle \bar{c}_i\bar{c}_j\rangle = \delta_{ij} + \mathrm{i}\,\Gamma^A_{ij}. \tag{3.1.14}$$

The matrix Γ^A is an antisymmetric matrix of order $2N$ and carries the information on entanglement. With the Wick's theorem, we can express any physical quantities by this matrix. The entanglement structure becomes apparent by the following transformations: generally, an invertible antisymmetric matrix A of order $2N$ is block diagonalized by a special orthogonal matrix W of order $2N$. Using this fact, we can transform the antisymmetric matrix Γ^A into the following block-diagonalized form

$$W^{\mathrm{T}}\Gamma^A W = \bigoplus_{i=1}^{N} \nu_i \begin{pmatrix} 0 & 1 \\ -1 & 0 \end{pmatrix} =: \Gamma^C \tag{3.1.15}$$

and define a set of new fermions as

$$\tilde{c}_i = \sum_{j=1}^{2N} W_{ji} \bar{c}_j \tag{3.1.16}$$

The forms of the matrix Γ^C and (3.1.14) imply that the fermion $\tilde{c}_{2i-1} = \sum_{j=1}^{2N} W_{j,2i-1} \bar{c}_j$ only correlates with the fermion $\tilde{c}_{2i} = \sum_{j=1}^{2N} W_{j,2i} \bar{c}_j$:

$$\langle \tilde{c}_i \tilde{c}_j \rangle = \delta_{ij} + \mathrm{i}\, \Gamma^C_{ij}. \tag{3.1.17}$$

Finally, we introduce new Dirac fermions as

$$d_i = \frac{1}{2}(\tilde{c}_{2i-1} + \mathrm{i}\, \tilde{c}_{2i}). \tag{3.1.18}$$

The correlation functions of the fermions $\{d_i\}$ read as

$$\langle d_i^\dagger d_j \rangle = \delta_{ij} \frac{1+\nu_i}{2}. \tag{3.1.19}$$

This means that the N Dirac fermions do not correlate with each other. The entanglement structure of the subsystem of length L_{sub} is obvious from the reduced density matrix ρ which is also a direct product form as

$$\rho = \rho_1 \otimes \rho_2 \otimes \cdots \otimes \rho_{L_{\mathrm{sub}}}, \tag{3.1.20}$$

where the density matrix ρ_i has eigenvalues

$$\frac{1 \pm \nu_i}{2}. \tag{3.1.21}$$

We can immediately calculate the entanglement entropy

$$S(L_{\mathrm{sub}}) = \sum_{i=1}^{L_{\mathrm{sub}}} \left[-p_i \ln p_i - (1-p_i) \ln (1-p_i) \right], \quad p_i = \frac{1-\nu_i}{2}. \tag{3.1.22}$$

There are $2^{L_{\mathrm{sub}}}$ eigenvalues of the reduced density matrix and they are terms in the expansion of $[p_1 + (1-p_1)] \cdots [p_{L_{\mathrm{sub}}} + (1 - p_{L_{\mathrm{sub}}})]$:

$$\lambda_\nu(L_{\mathrm{sub}}) = \prod_{i=1}^{L_{\mathrm{sub}}} p_i^{1-s_i} (1-p_i)^{s_i}, \quad s_i = 0, 1. \tag{3.1.23}$$

Then entanglement spectrum is given by

$$\xi_\nu = -\ln \lambda_\nu(L_{\mathrm{sub}}). \tag{3.1.24}$$

We summarize the above procedure in Fig. 3.1.1.

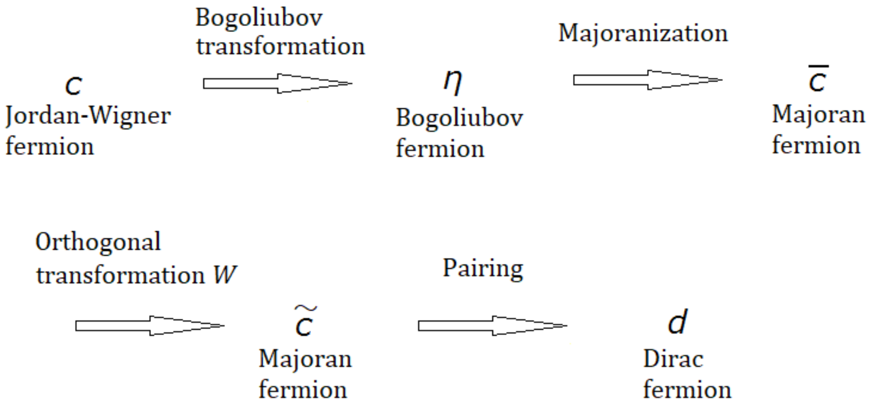

Figure3.1.1 The procedure to reveal entanglement properties.

3.1.3 Correlation functions

The topological phases are characterized by non-local correlation functions [6,10,134]. Here we show how to calculate the correlation functions $O_{XZX}(L)$ and $O_{XX}(L)$ defined in (2.3.77) and (2.3.71), respectively. The other correlation functions are obtained in the same way. For later convenience, we define the operators $\mathcal{A}$ and $\mathcal{B}$ as

$$\begin{aligned} \mathcal{A}_i &= c_i + c_i^\dagger = \bar{c}_{2i-1}, \\ \mathcal{B}_i &= c_i - c_i^\dagger = -\mathrm{i}\,\bar{c}_{2i}. \end{aligned} \tag{3.1.25}$$

Using these operators, we rewrite the string correlation function of distance L as

$$O_{XZX}(L) = (-1)^{L+1} \left\langle \mathcal{B}_1\mathcal{B}_2 \prod_{j=3}^{L-2} (\mathcal{A}_j\mathcal{B}_j)\, \mathcal{A}_{L-1}\mathcal{A}_L \right\rangle, \tag{3.1.26}$$

where $\langle\cdot\rangle$ denotes the expectation value taken with respect to the Bogoliubov vacuum $|\mathrm{vac}\rangle$. This expression consists of $(2L-4)$ fermion operators. To calculate this expectation value, we need the following contractions

$$\langle \mathcal{A}_i\mathcal{A}_j\rangle = \delta_{ij}, \tag{3.1.27}$$

$$\langle \mathcal{B}_i\mathcal{B}_j\rangle = -\delta_{ij}, \tag{3.1.28}$$

$$\langle \mathcal{B}_i\mathcal{A}_j\rangle = \sum_{\alpha=1}^{N} \psi_{i\alpha}\phi_{j\alpha} =: D(i,j). \tag{3.1.29}$$

In general, we need to calculate the Pfaffian of the antisymmetric matrix whose components are above contractions [141,142]. Because the operators $\mathcal{A}$ ($\mathcal{B}$) appearing in Eq. (3.1.26) do not have the same index j, the Pfaffian is reduced to the determinant of the matrix of order $(L-2)$ given as

$$\begin{pmatrix} D(1,L) & D(1,3) & \ldots & D(1,L-1) \\ D(2,L) & D(2,3) & \ldots & \vdots \\ \vdots & \vdots & \ddots & \vdots \\ D(L-2,L) & \ldots & \ldots & D(L-2,L-1) \end{pmatrix}. \tag{3.1.30}$$

When the excited states are concerned, we must handle the Pfaffian.

We show how to calculate the expectation value in the bogolon state. Because the Bogoliubov operators are fermionic, we need to know the expectation value of $2L$ fermion operators $\{\Psi_i\}$ with respect to the vacuum

$$P_{2L} = \langle \Psi_1 \Psi_2 \cdots \Psi_{2L-1} \Psi_{2L} \rangle. \tag{3.1.31}$$

We calculate this by using the Pfaffian as follows. The Pfaffian has a triangular form:

$$P_{2L} = \sum_{\pi \in S_{2L}^{<}} (-1)^{\pi} P_{\pi(1)\pi(2)} P_{\pi(3)\pi(4)} \cdots P_{\pi(2L-1)\pi(2L)} \tag{3.1.32}$$

$$= \begin{vmatrix} P_{1,2} & P_{1,3} & \ldots & P_{1,L} & P_{1,L+1} & P_{1,L+2} & \ldots & P_{1,2L} \\ & P_{2,3} & \ldots & \ldots & P_{2,L+1} & \ldots & \ldots & P_{2,2L} \\ & & \ddots & & \vdots & \ldots & \ldots & \vdots \\ & & & \ddots & \vdots & \ldots & \ldots & \vdots \\ & & & & P_{L,L+1} & P_{L,L+2} & \ldots & P_{L,2L} \\ & & & & & P_{L+1,L+2} & & \vdots \\ & & & & & & \ddots & \vdots \\ & & & & & & & P_{2L-1,2L} \end{vmatrix}. \tag{3.1.33}$$

Its elements are contractions of two operators

$$P_{ij} = \langle \Psi_i \Psi_j \rangle. \tag{3.1.34}$$

In Eq. (3.1.33), $S_{2L}^{<}$ is an ordered subset of symmetric group S_{2L} of order $2L$ in the following manner:

$$\pi(2i-1) < \pi(2i) \text{ and } \pi(2i-1) < \pi(2j-1), \quad 1 \le i < j \le L. \tag{3.1.35}$$

We use in the numerical calculation one of the important properties of the Pfaffian: for the antisymmetric matrix A of order $2L$ whose off-diagonal part is the triangular part in Eq. (3.1.33), the equation

$$\det A = (P_{2L})^2 \tag{3.1.36}$$

holds. Thus we need to handle the Pfaffian of the matrix of order $(2L-2)$ instead of the determinant of the matrix of order $(L-1)$.

We also calculate the correlation function which characterizes the ferromagnetic phase of the transverse-field Ising model. Because of the non-local nature of the Jordan–Wigner transformation, a local two-spin correlation function in the spin representation becomes non-local in the fermion representation. The correlation function between two spins in the distance L

$$O_{XX}(L) = \langle \sigma_1^x \sigma_L^x \rangle \tag{3.1.37}$$

is calculated in a similar manner:

$$O_{XX}(L) = \left\langle \mathcal{B}_1 \prod_{j=2}^{L-1} \left(\mathcal{B}_j \mathcal{A}_j\right) \mathcal{A}_L \right\rangle \tag{3.1.38}$$

$$= \begin{vmatrix} D(1,2) & D(1,3) & \dots & D(1,L) \\ D(2,2) & D(2,3) & \dots & \vdots \\ \vdots & \vdots & \ddots & \vdots \\ D(L-1,2) & \dots & \dots & D(L-1,L) \end{vmatrix} \tag{3.1.39}$$

is given by the determinant of the matrix of order $(L-1)$.

3.2 Time-dependent Bogoliubov theory

We describe the method to study the time evolution of the system by the time-dependent Bogoliubov theory [143, 144]. In the following, we consider general time-dependent Hamiltonians which are quadratic in the fermions $\{c_i\}$:

$$H(t) = \sum_{i,j=1}^{N} \left[c_i^\dagger A_{ij}(t) c_j + \frac{1}{2} \left(c_i^\dagger B_{ij}(t) c_j^\dagger + c_i B_{ji}^*(t) c_j \right) \right]. \tag{3.2.1}$$

Here, the coupling constants depend on time t. We deal with the time evolution in the Heisenberg representation. The fermions $\{c_{i,\mathrm{H}}(t)\}$ in the Heisenberg representation obey the Heisenberg equations of motion given by

$$\mathrm{i} \frac{d}{dt} c_{i,\mathrm{H}}(t) = \sum_{j=1}^{N} \left(A_{ij}(t) c_{j,\mathrm{H}}(t) + B_{ij}(t) c_{j,\mathrm{H}}^\dagger(t) \right). \tag{3.2.2}$$

We write the Bogoliubov operators which diagonalize the Hamiltonian $H(t^{\mathrm{in}})$ at the initial time t^{in} as $\{\eta_\alpha^{\mathrm{in}}\}$, and the corresponding eigenvectors as $\{\phi_\alpha^{\mathrm{in}}\}$ and $\{\psi_\alpha^{\mathrm{in}}\}$. With these eigenvectors, we define the vectors

$$u_\alpha^{\mathrm{in}} = \frac{\phi_\alpha^{\mathrm{in}} + \psi_\alpha^{\mathrm{in}}}{2}, \quad v_\alpha^{\mathrm{in}} = \frac{\phi_\alpha^{\mathrm{in}} - \psi_\alpha^{\mathrm{in}}}{2} \tag{3.2.3}$$

for later convenience. The Heisenberg equation of motion (3.2.2) is solved in the following way: let us write the fermions $\{c_{i,\mathrm{H}}(t)\}$ as

$$c_{i,\mathrm{H}}(t) = \sum_{\alpha=1}^{N} \left(u_{i,\alpha}(t)\eta_{\alpha}^{\mathrm{in}} + v_{i,\alpha}^{*}(t)\eta_{\alpha}^{\mathrm{in}\dagger} \right), \tag{3.2.4}$$

where $u_{i,\alpha}(t)$ and $v_{i,\alpha}(t)$ denote the i-th component of vectors $u_{\alpha}(t)$ and $v_{\alpha}(t)$, respectively. By substituting this expression for $c_{i,\mathrm{H}}(t)$ in Eq. (3.2.2), we obtain the following simultaneous linear differential equations of $u_{\alpha}(t)$ and $v_{\alpha}(t)$

$$\begin{cases} \mathrm{i}\dfrac{d}{dt}u_{i,\alpha}(t) = \displaystyle\sum_{j=1}^{N} \left(A_{ij}(t)u_{j,\alpha}(t) + B_{ij}(t)v_{j,\alpha}(t) \right), & (3.2.5\mathrm{a}) \\ \mathrm{i}\dfrac{d}{dt}v_{i,\alpha}(t) = -\displaystyle\sum_{j=1}^{N} \left(A_{ij}(t)v_{j,\alpha}(t) + B_{ij}(t)u_{j,\alpha}(t) \right) & (3.2.5\mathrm{b}) \end{cases}$$

with the initial condition

$$u_{\alpha}(t_{\mathrm{in}}) = u_{\alpha}^{\mathrm{in}}, \quad v_{\alpha}(t_{\mathrm{in}}) = v_{\alpha}^{\mathrm{in}}. \tag{3.2.6}$$

With the above setup, we calculate the expectation value of an operator $O(c_i, c_i^{\dagger})$ at time t

$$\langle \Psi(t)|O(c_i, c_i^{\dagger})|\Psi(t)\rangle = \langle \Psi(t_{\mathrm{in}})|O(c_{i,\mathrm{H}}(t), c_{i,\mathrm{H}}^{\dagger}(t))|\Psi(t_{\mathrm{in}})\rangle. \tag{3.2.7}$$

When the initial state $|\Psi(t_{\mathrm{in}})\rangle$ is set to the Bogoliubov vacuum, the expectation value can be calculated as in the case of the time-independent Hamiltonian. Because only $u_{\alpha}(t)$ and $v_{\alpha}(t)$ depend on time t, what we need to do is to calculate the time evolution of $u_{\alpha}(t)$ and $v_{\alpha}(t)$ using Eqs. (3.2.5).

Time dependence of entanglement is analyzed in much the same way as in the case of the ground state in Sec. 3.1.2. By constructing the Dirac fermions at time t, we obtain the time-dependent entanglement entropy $S(L_{\mathrm{sub}}, t)$ and entanglement spectrum $\{\lambda_i(L_{\mathrm{sub}}, t)\}$.

3.3 Infinite time evolving block decimation

In the previous sections, we have analyzed lattice models by exactly diagonalizing the Hamiltonians with the Bogoliubov transformation. Although this is useful, sometimes finite-size effects matter. Therefore we use the infinite time evolving block decimation (iTEBD) method [89, 90] to avoid this problem by dealing with infinite-size systems directly. This method is based on the MPS in Sec. 2.2 utilizing entanglement and enables us to efficiently obtain the ground-state wave functions of one-dimensional quantum systems of infinite size.

In Sec. 3.3.1, we show how to obtain the infinite-size ground-state wave function by imaginary-time evolution. In Sec. 3.3.2, we mention the real-time evolution of the state. In Sec. 3.3.3, we show how to extract entanglement properties and calculate correlation functions.

3.3.1 Imaginary time evolution

We introduce the iTEBD algorithm basing on the MPS. We assume the translation symmetry of the Hamiltonian H. When the interaction acts upon n_{int} adjacent sites, we group these n_{int} sites and consider them as the unit. To represent the states on an infinite chain, we only need the n_{int} sets of matrices $\{\Gamma^{[i]}(m_i), \Lambda^{[i]}\}$ $(i = 1, \ldots, n_{\text{int}})$ for the n_{int}-site unit. Here $m_i (= 1, \ldots, d)$ labels the physical states of the local Hilbert space on the i-th site, $\Gamma^{[i]}(m_i)$ is a square matrix of order χ_{b} (bond dimension), and $\Lambda^{[i]}$ is a diagonal matrix of order χ_{b}. Although the size of the matrices depends on the site in general, we here assume that it is independent of the site for simplicity. We call them *iMPS* (infinite matrix-product state). The wave function is written as

$$|\Psi_0\rangle = \sum_{\{m_i\},\{\alpha\},\{\beta\}} \cdots \Gamma^{[1]}_{\alpha_1\beta_1}(m_1)\Lambda^{[1]}_{\beta_1\alpha_2} \cdots \Gamma^{[n_{\text{int}}]}_{\alpha_{n_{\text{int}}}\beta_{n_{\text{int}}}}(m_{n_{\text{int}}})\Lambda^{[n_{\text{int}}]}_{\beta_{n_{\text{int}}}\alpha_{n_{\text{int}}+1}} \cdots |m_1\rangle \cdots |m_{n_{\text{int}}}\rangle \cdots . \tag{3.3.1}$$

First we make an initial state $|\Psi_0\rangle$ with iMPS whose data $\{\Gamma_0^{[i](m_i)}, \Lambda_0^{[i]}\}$ are randomly given. Then the imaginary-time evolution projects the state onto the ground state $|\Psi\rangle$ of the Hamiltonian H:

$$|\Psi\rangle = \lim_{\tau\to\infty} \frac{\exp(-H\tau)|\Psi_0\rangle}{|\exp(-H\tau)|\Psi_0\rangle|}. \tag{3.3.2}$$

The imaginary-time evolution is nothing but updating the iMPS data $\{\Gamma^{[i]}(m_i), \Lambda^{[i]}\}$ as we will see below. Let us consider the imaginary-time evolution operator by an infinitesimal time $d\tau$

$$U = \exp(-Hd\tau), \quad d\tau \ll 1. \tag{3.3.3}$$

This is a tensor operation acting on the physical index of the MPS. We simplify the calculation by using the *Suzuki–Trotter decomposition* [131]. For convenience, let the Hamiltonian have only nearest-neighbor interactions and $n_{\text{int}} = 2$. Then the iMPS is specified by the four matrices $\Gamma^{[A]}, \Lambda^{[A]}, \Gamma^{[B]}, \Lambda^{[B]}$ for each m_i (see Fig. 3.3.1). In this case, the Hamiltonian is decomposed into to parts

$$H = H_A + H_B = \sum_{\text{even } i} H^{i,i+1} + \sum_{\text{odd } i} H^{i,i+1}. \tag{3.3.4}$$

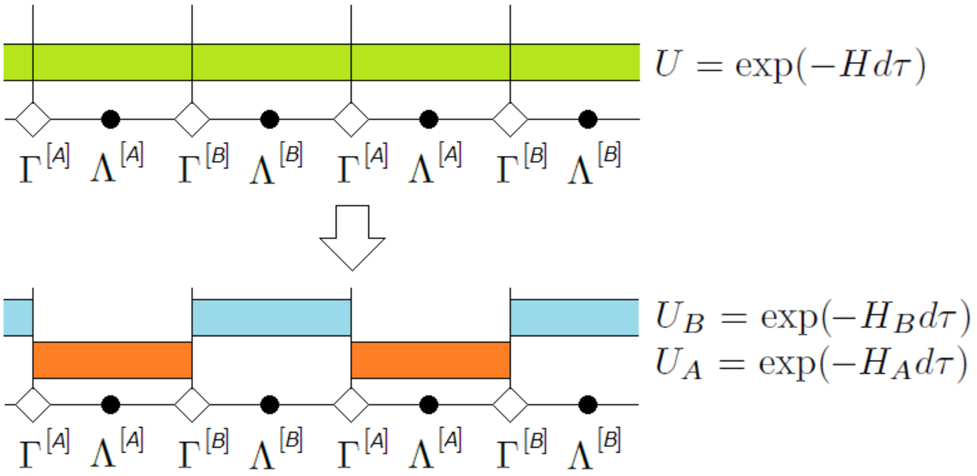

Figure3.3.1 Suzuki–Trotter decomposition: imaginary time evolution operator U by total Hamiltonian H is decomposed into the operators U_A, U_B by the Hamiltonian H_A, H_B, respectively. The rectangles represent the tensors U, U_A, and U_B.

Terms in H_A (H_B) commute with each other while H_A does not commute with H_B. Then, using the lowest-order Suzuki–Trotter decomposition

$$\exp(-\tau H) = \left(\exp(-\frac{\tau}{n}H)\right)^n \tag{3.3.5}$$

$$= \lim_{n\to\infty}\left(\exp(-\frac{\tau}{n}H_A)\exp(-\frac{\tau}{n}H_B)\right)^n, \tag{3.3.6}$$

we can trade the time-evolution under $U = \exp(-Hd\tau)$ ($d\tau = \frac{\tau}{n}$) with the successive application of the following tensors

$$U_A = \exp(-H_A d\tau), \quad U_B = \exp(-H_B d\tau) \tag{3.3.7}$$

on the iMPS (Fig. 3.3.1). In this way, the state evolves by $d\tau$ in imaginary time. Iterating this procedure until the energy converges, we obtain the desired ground state.

To improve the numerical accuracy, we may use the symmetric Suzuki–Trotter decomposition of order two [145]

$$\exp H = \lim_{n\to\infty}\left(\exp(\frac{1}{2n}H_A)\exp(\frac{1}{n}H_B)\exp(\frac{1}{2n}H_A)\right)^n \tag{3.3.8}$$

for the update. Because we use finite n in the numerical calculation, the numerical error is unavoidable. For the Suzuki–Trotter decomposition of order one and two, the error is of order $\frac{1}{n}$ and $\frac{1}{n^2}$, respectively [145].

Now we describe the details of the update of the iMPS specified by the MPS data $\{\Gamma^{[A]}, \Lambda^{[A]}, \Gamma^{[B]}, \Lambda^{[B]}\}$. Updating the iMPS by the operator U_A is done by the following four steps. The procedure is summarized in Fig. 3.3.2.

step1

We multiply the matrices $\Gamma^{[A]}$ and $\Gamma^{[B]}$ by the matrix U_A.

step2

Contracting the indices of the tensors $\Gamma^{[A]}, \Lambda^{[A]}, \Gamma^{[B]}, \Lambda^{[B]}$, and U_A, we define a new rank-4 tensor M:

$$M_{\alpha i;\beta j} = \sum_{k,l=1}^{d} \sum_{\gamma,\delta,\epsilon,\zeta=1}^{\chi_{\mathrm{b}}} \Lambda^{[B]}_{\alpha\gamma} \Gamma^{[A]}_{\gamma\delta}(k) \Lambda^{[A]}_{\delta\epsilon} \Gamma^{[B]}_{\epsilon\zeta}(l) \Lambda^{[B]}_{\zeta\beta} U^{[A]}_{ij;kl}. \tag{3.3.9}$$

step3

We consider the tensor M as the matrix of dimension $d\chi_{\mathrm{b}} \times d\chi_{\mathrm{b}}$ by taking the tensor product of the physical and the ancillary spaces. Then we perform the singular-value decomposition on the matrix M:

$$M_{\alpha i;\beta j} = \sum_{\gamma,\delta=1}^{d\chi_{\mathrm{b}}} M^{[A]}_{\alpha i;\gamma} \Lambda_{\gamma\delta} M^{[B]}_{\delta;\beta j}. \tag{3.3.10}$$

The Λ is a diagonal matrix of order $d\chi_{\mathrm{b}}$ whose elements are non-negative, and $M^{[A]}$ and $M^{[B]}$ are square matrices of order $d\chi_{\mathrm{b}}$. The size of these matrices do not match those of the original ones. To recover the size of the original ones, we keep only the largest χ_{b} singular values out of the $d\chi_{\mathrm{b}}$ singular values. Specifically, we define a new matrix $\tilde{\Lambda}^{[A]}$ by extracting matrix elements of Λ corresponding the retained singular values. Similarly, we choose corresponding column (row) of the matrix $M^{[A]}$ ($M^{[B]}$) of order $d\chi_{\mathrm{b}}$. Decomposing the tensor space to the original physical and ancillary spaces, we obtain the square tensors X (Y).

step4

By multiplying $1 = \Lambda^{[B]}\Lambda^{[B]-1}$ from the left of the matrix X, and $1 = \Lambda^{[B]-1}\Lambda^{[B]}$ from the right of Y,

$$\tilde{\Lambda}^{[A]} = \Lambda^{[B]-1} X, \quad \tilde{\Lambda}^{[B]} = Y \Lambda^{[B]-1}, \tag{3.3.11}$$

we finally obtain the updated iMPS $\{\tilde{\Gamma}^{[A]}, \tilde{\Lambda}^{[A]}, \tilde{\Gamma}^{[B]}, \tilde{\Lambda}^{[B]}\}$ which has the same bond dimension χ_{b} as the original iMPS.

With the above steps, we complete the update of iMPS when the tensor U_A is acted. The update by the tensor U_B goes similarly. It is clear how the procedure described above is generalized when we consider the Hamiltonian with the next-nearest interactions. The update of the iMPS is done in a similar manner except for the size of the matrices on which we perform the singular-value decomposition.

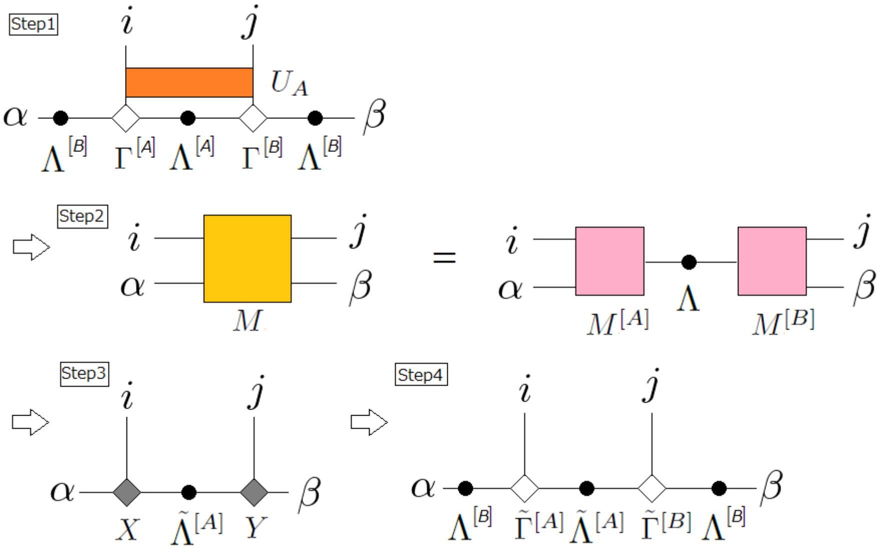

Figure3.3.2 Update of the iMPS: Transform the iMPS with the tensor U_A to the form of the original iMPS.

3.3.2 Real-time evolution

By the imaginary-time evolution, we obtain the ground state $|\Psi(0)\rangle$. We can study the real-time evolution of the state using the MPS. The wave function at time t is given as

$$|\Psi(t)\rangle = \exp(-\mathrm{i}Ht)|\Psi(0)\rangle. \tag{3.3.12}$$

To obtain the state, we can use the same strategy and update the iMPS as in the case of the imaginary time evolution [114]. The Hamiltonian may depend on time. In this case, the wave function at time t is given as

$$|\Psi(t)\rangle = \exp\left(-\mathrm{i}\int_0^t H(t)dt\right)|\Psi(0)\rangle. \tag{3.3.13}$$

3.3.3 Calculation of physical quantities

By using the wave function obtained by the imaginary and real time evolutions, we calculate physical quantities in the ground state. When we divide an infinite system into two semi-infinite systems by cutting the system between the i-th site and the $(i+1)$-th site, the entanglement entropy S and the entanglement spectrum $\{\xi_i\}$ are easily obtained as

$$S = -\sum_{\alpha=1}^{\chi_\mathrm{b}} \lambda_\alpha^2 \ln \lambda_\alpha^2, \tag{3.3.14}$$

$$\xi_\alpha = -\ln \lambda_\alpha^2, \tag{3.3.15}$$

where $\{\lambda_\alpha\}$ are diagonal elements of the matrix $\Lambda^{[i]}$. We next consider the correlation functions. Let us calculate an operator $O^{[i]}$ at the i-th site. From the orthogonality of the Schmidt basis, the expectation value is obtained as [89, 90]

$$\langle\Psi|O^{[i]}|\Psi\rangle = \sum_{\alpha,\beta,j,k} (\Lambda^{[i-1]}_{\alpha})^2 \Gamma^{[i]}_{\alpha\beta}(j) O^{[i]}_{jk} (\Gamma^{[i]}_{\alpha\beta}(k))^* (\Lambda^{[i]}_{\beta})^2. \tag{3.3.16}$$

The diagrammatic representation is shown in Fig. 3.3.3. The operator $O^{[i]}$ acts on the physical indices of the iMPS and its conjugate at the i-th site. Similarly, we can calculate a correlation function between the i-th and j-th sites (Fig. 3.3.4).

$$\begin{aligned}\langle\Psi|O^{[i]}O^{[j]}|\Psi\rangle = \sum_{\{\alpha\},\{\beta\},\{m\},\{m'\},\beta_L,\alpha_R} & (\Lambda^{[i-1]}_{\beta_L\alpha_i})^2 \Gamma^{[i]}_{\alpha_i\beta_i}(m_i) O^{[i]}_{m_i m'_i} (\Gamma^{[i]}_{\alpha_i\beta_i}(m'_i))^* (\Lambda^{[i]}_{\beta_i\alpha_{i+1}})^2 \\ & \Gamma^{[i+1]}_{\alpha_{i+1}\beta_{i+1}}(m_{i+1}) (\Gamma^{[i+1]}_{\alpha_{i+1}\beta_{i+1}}(m'_{i+1}))^* (\Lambda^{[i+1]}_{\beta_{i+1}\alpha_{i+2}})^2 \\ & \cdots \\ & \Gamma^{[j-1]}_{\alpha_{j-1}\beta_{j-1}}(m_{j-1}) (\Gamma^{[j-1]}_{\alpha_{j-1}\beta_{j-1}}(m'_{j-1}))^* (\Lambda^{[j-1]}_{\beta_{j-1}\alpha_j})^2 \\ & \Gamma^{[j]}_{\alpha_j\beta_j}(m_j) O^{[j]}_{m_j m'_j} (\Gamma^{[j]}_{\alpha_j\beta_j}(m'_j))^* (\Lambda^{[j]}_{\beta_j\alpha_R})^2.\end{aligned} \tag{3.3.17}$$

In the actual calculation, we need to multiply $|i-j|$ transfer matrices and contract the indices of them.

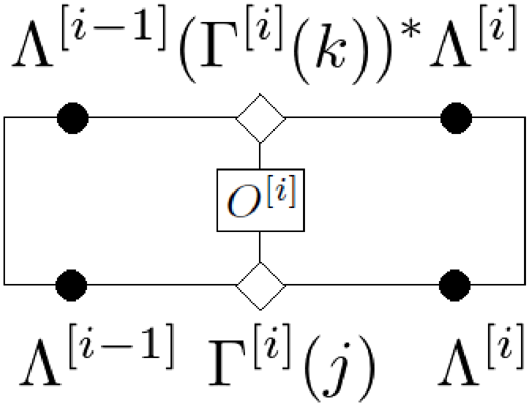

Figure3.3.3 The expectation value of an operator acting on the i-th site.

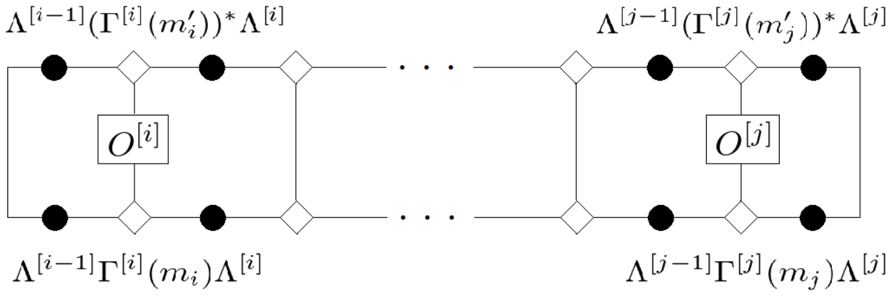

Figure3.3.4 The expectation value of a correlation function between the i-th and j-th sites.

Chapter4

Topological and dynamical properties of the generalized Kitaev model

In this chapter, we study the ground-state phase diagram and dynamical properties of Majorana fermions with several competing couplings in one dimension. In Sec. 4.1, we introduce the model that we consider throughout this section and explain the methods to analyze the model in the following sections. In Sec. 4.2, we determine the ground-state phase diagram and the nature of the quantum phase transitions among the phases with a combination of various analytical and numerical methods. Paying particular attention to the bulk–edge correspondence, we also characterize each phase separated by the critical points with the winding number calculated from the bulk Hamiltonian and the degeneracy structure of the entanglement spectrum. In Sec. 4.3, we investigate the dynamics during interaction sweeps across the critical points. Characteristic structures in the dynamics are observed, which can be understood from a viewpoint of the bogolons. In Sec. 4.4, we conclude and summarize this chapter.

4.1 Model

Throughout this chapter, we consider the generalized Kitaev model in one dimension introduced in Refs. [91, 92] to study the criticality of quantum phase transitions and the dynamical properties during the sweep dynamics associated with topological phase transitions.

The model is defined as

$$\begin{aligned} H =& - J^{XZX}\sum_{i=1}^{N}(c_i^\dagger - c_i)(c_{i+2}^\dagger + c_{i+2}) \\ & - J^{YY}\sum_{i=1}^{N}(c_i^\dagger + c_i)(c_{i+1}^\dagger - c_{i+1}) \\ & + J^{YZY}\sum_{i=1}^{N}(c_i^\dagger + c_i)(c_{i+2}^\dagger - c_{i+2}) \\ =& \mathrm{i}\sum_{i=1}^{N}(J^{XZX}\bar{c}_{2i}\bar{c}_{2i+3} - J^{YY}\bar{c}_{2i-1}\bar{c}_{2i+2} + J^{YZY}\bar{c}_{2i-1}\bar{c}_{2i+4}). \end{aligned} \tag{4.1.1}$$

This model contains hopping and superconductor pairing of spinless fermions on both nearest sites and next-nearest sites. For the open boundary condition, we take $c_{N+1} = c_{N+2} = 0$ whereas for the periodic boundary condition $c_{N+1} = c_1$ and $c_{N+2} = c_2$. In the spin representation, the model is rewritten as

$$H_{\mathrm{GC}} = \sum_{i=1}^{N}(-J^{XZX}\sigma_i^x\sigma_{i+1}^z\sigma_{i+2}^x + J^{YY}\sigma_i^y\sigma_{i+1}^y + J^{YZY}\sigma_i^y\sigma_{i+1}^z\sigma_{i+2}^y), \tag{4.1.2}$$

where N is the system size and $\sigma_i^{\alpha_0}$ $(\alpha_0 = x, y, z)$ are the Pauli matrices at site i. The open boundary condition corresponds to taking $\sigma_{N+1}^{\alpha_0} = \sigma_{N+2}^{\alpha_0} = 0$ $(\alpha_0 = x, y, z)$ whereas the periodic boundary condition to $\sigma_{N+1}^{\alpha_0} = \sigma_1^{\alpha_0}$ and $\sigma_{N+2}^{\alpha_0} = \sigma_2^{\alpha_0}$. The model contains the cluster interaction $\sigma_i^x\sigma_{i+1}^z\sigma_{i+2}^x$, the Ising interaction $\sigma_i^y\sigma_{i+1}^y$, and another cluster interaction $\sigma_i^y\sigma_{i+1}^z\sigma_{i+2}^y$. When $J^{YZY} = 0$, the model reduces to the cluster-Ising model whose statistical properties are studied in Refs. [133,134]. We can flip the sign of J^{YY} by the following unitary transformation:

$$\begin{aligned} & U^\dagger\sigma_i^x U \mapsto (-1)^i\sigma_i^x, \ \ U^\dagger\sigma_i^y U \mapsto (-1)^i\sigma_i^y, \\ & U = \exp\left(\mathrm{i}\frac{\pi}{2}\sum_j \sigma_j^z\right). \end{aligned} \tag{4.1.3}$$

Therefore the phase diagram is symmetric about $J^{YY} = 0$ line. In general, the model with only one of the three couplings $(J^{XZX}, J^{YY}, J^{YZY})$ being non-zero possesses a special property; all the terms of the Hamiltonian commute with each other and the entire spectrum is constructed by creating local (non-dispersive) excitations one by one.

4.2 Phase diagram

In this section, we solve the model (4.1.1) under the periodic boundary condition and characterize the ground-state phase diagram using several techniques. In Sec. 4.2.1, we study the energy dispersion of the model by the Fourier transformation followed by the Bogoliubov transformation. We then determine the critical points where the energy gap closes. In Sec. 4.2.2, we determine the universality class of these transitions analytically. In Sec. 4.2.3, we characterize each phase with the winding number calculated from the bulk Hamiltonian. We also characterize each phase by order parameters in Sec. 4.2.4 and by entanglement in Sec. 4.2.5.

4.2.1 Phases and critical points

To determine the phase boundaries of the ground-state phase diagram of the model (4.1.1), we calculate the energy spectrum when the periodic boundary condition is imposed. When the periodic boundary condition is imposed, there are no unpaired Majorana modes. By performing the Fourier transformation

$$H = 2 \sum_{0 \le k \le \pi} \left[\epsilon_k (c_k^\dagger c_k + c_{-k}^\dagger c_{-k}) + i\delta_k (c_k^\dagger c_{-k}^\dagger + c_k c_{-k}) \right] \tag{4.2.1}$$

followed by the Bogoliubov transformation (see App. B for details)

$$\eta_k = \cos\frac{\theta_k}{2} c_k - i \sin\frac{\theta_k}{2} c_{-k}^\dagger, \tag{4.2.2}$$

$$\{\eta_k, \eta_{k'}^\dagger\} = \delta_{kk'}, \tag{4.2.3}$$

$$\tan\theta_k = -\frac{\delta_k}{\epsilon_k}, \tag{4.2.4}$$

the model is expressed in momentum space as

$$H = \sum_{0 \le k \le \pi} E_k \, (\eta_k^\dagger \eta_k + \eta_{-k}^\dagger \eta_{-k}), \quad E_k = 2\sqrt{\epsilon_k^2 + \delta_k^2}, \tag{4.2.5}$$

where $E_k \geq 0$ is the excitation energy at the wave number k and

$$\epsilon_k = (J^{XZX} - J^{YZY}) \cos 2k + J^{YY} \cos k, \tag{4.2.6}$$

$$\delta_k = (J^{XZX} + J^{YZY}) \sin 2k - J^{YY} \sin k. \tag{4.2.7}$$

In the following, we use J^{XZX} as the energy unit and assume that J^{XZX} is positive for concreteness.

The Hamiltonian in the momentum space has the form of the Bogoliubov–de Gennes Hamiltonian with time reversal symmetry and the ground state is given by the vacuum of the Bogoliubov operators $\{\eta_k\}$:

$$\eta_k|\mathrm{GS}\rangle = 0, \quad \forall \mathrm{k}. \tag{4.2.8}$$

The critical points which separate phases are determined by the condition that the excitation energy E_k vanishes at a certain wave number k. The phase boundaries are depicted by the thick solid curves in Fig. 4.2.1. For example, we show the energy dispersion at critical points (a) $J^{YY}/J^{XZX} = 0$, $J^{YZY}/J^{XZX} = 1$ and (b) $J^{YY}/J^{XZX} = -1$, $J^{YZY}/J^{XZX} = 0$ in Figs. 4.2.2(a), (b). The dispersions around the zero-energy wave-numbers are linear.

In order to characterize each phase separated by the phase boundaries, we calculate the order parameters of the phases by using the time-evolving block decimation method for infinite systems (iTEBD, Sec. 3.3) or consider the extreme cases and use the adiabatic continuity [91]. For instance, the phase "P" is continuously connected to the quantum paramagnetic phase where σ^z are polarized. As we show in Sec. 4.2.4, the order parameters O_{XZX}, O_{YZY}, and O_{YY} have finite values in the C, C*, and AF$^{(y)}$ phases, respectively. The antiferromagnetic phase in the x direction (AF$^{(x)}$) is characterized by the AF order parameter O_{XX}

$$O_{XX} = \lim_{L\to\infty} (-1)^{L-1} \langle \sigma_1^x \sigma_L^x \rangle . \tag{4.2.9}$$

The results are summarized in Fig. 4.2.1. The phases on the right of the J^{YZY}-axis and the ones on the left are mapped onto each other by the unitary transformation (4.1.3); the AF phases are mapped onto the ferromagnetic (F) phases. The AF$^{(x)}$, F$^{(x)}$, and P phases appear as a result of competition among interactions in the model (4.1.1). We can see that all the phase transitions are continuous from the order parameters (not shown here).

4.2.2 Universality class

We determine the universality classes of the transitions for completeness. In fact, all the phase transitions that occur are continuous and described by Lorentz-invariant conformal field theories (CFTs) except at the points marked in Fig. 4.2.1 as "M3", where the dispersion E_k is quadratic in k and the dynamical critical exponent takes $z = 2$. The information on the universality class of quantum phase transition and the corresponding central charge c at each critical point can be most conveniently extracted from the finite-size energy spectrum [146,147] (or equivalently, from the low-temperature behavior of the free energy density [148]) or from the scaling behavior of the block entanglement entropy [34, 35]. In order to obtain more precise information on the universality class, we adopt the former and identify the contents of the scaling operators using the spectrum obtained exactly above. Throughout this subsection, we assume the periodic boundary condition.

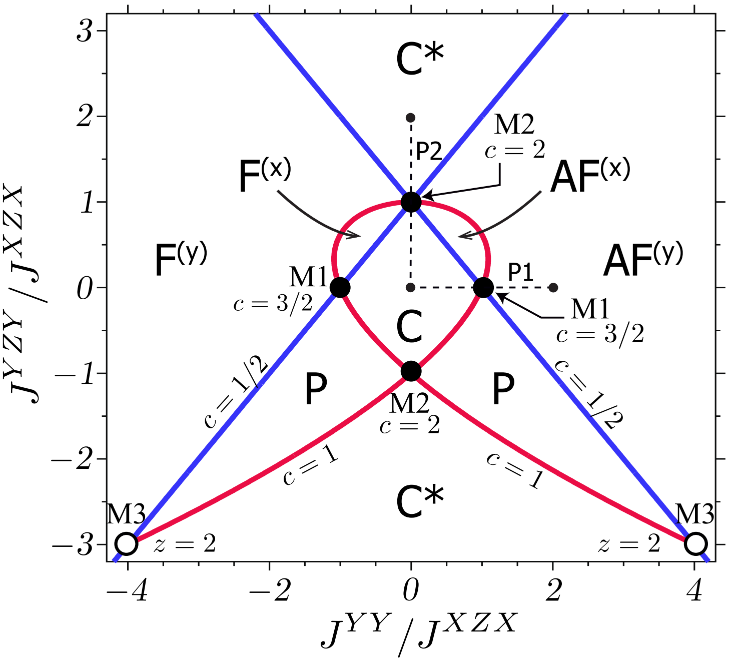

Figure4.2.1 Ground-state phase diagram of the generalized Kitaev model (4.1.1) for $J^{XZX} > 0$ [91,92]. On the thick solid curves, the excitation energy E_k vanishes at certain values of k. The abbreviations mean the cluster (C), dual cluster (C*), ferromagnetic (F), and antiferromagnetic (AF) phases. The quantum paramagnetic (P) phase cannot be characterized by string and (anti) ferromagnetic order parameters. The superscript represents the direction of the order. On the blue (red) phase boundaries, a second-order transition with $c = 1/2$ ($c = 1$) occurs. M1 and M2 denote multicritical points characterized by higher central charges. The two points M3 are non-Lorentz-invariant critical points. (Figure taken from Ref. [92].)

The method relies on the CFT prediction on the finite-size spectrum of a (1+1)-dimensional quantum system at the critical point [147]:

$$E_{h,\bar{h}}(N) = N\epsilon_\infty - \frac{\pi v_\mathrm{s}}{6N}c + \frac{2\pi}{N}v_\mathrm{s}(h + \bar{h} + n_\mathrm{L} + n_\mathrm{R}) \quad (n_\mathrm{L}, n_\mathrm{R} = 0, 1, 2, \ldots)\ , \tag{4.2.10}$$

where ϵ_∞ is the ground-state energy density in the infinite-size limit and v_s is the velocity that characterizes the k-linear dispersion of the critical excitations. In general, the entire spectrum decomposes into the several sectors labeled by the conformal weights $(h, \bar{h})$. The central charge c and the list of the pairs $(h, \bar{h})$ appearing in the actual spectrum (i.e., operator contents) determines the universality. As the exact spectrum is obtained in a closed form here, it is rather straightforward to obtain these data (see App. E for more details).

In Fig. 4.2.1, we show the universality classes obtained in this way. On the blue solid lines, there is only one gapless k-linear Majorana point at $k = 0$ or $k = \pi$. The quantum phase transition there belongs to the Ising universality class with $c = 1/2$. Extracting c for the phase boundaries shown by the red solid lines is tricky as the two Majorana points are located at

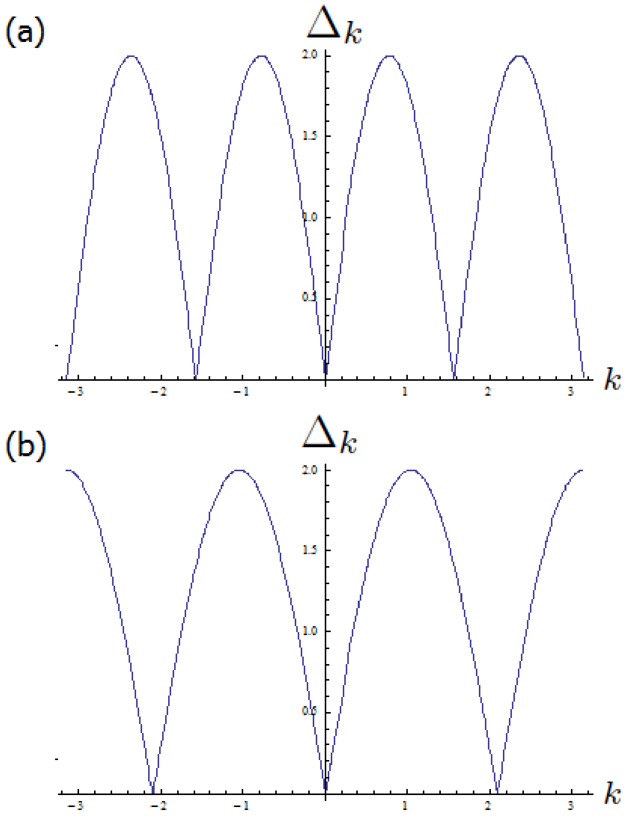

Figure4.2.2 Energy dispersion at the critical points: (a) $J^{YY}/J^{XZX} = 0$, $J^{YZY}/J^{XZX} = 1$, and (b) $J^{YY}/J^{XZX} = -1$, $J^{YZY}/J^{XZX} = 0$. (Figure taken from Ref. [110].)

incommensurate momenta and the approach to the infinite-size limit is quite irregular. So we used the free energy density instead and fitted the low-temperature (T) free energy density $F(T,N)/N$, which is calculated exactly using Eq. (4.2.5) by its CFT asymptotic form [148]

$$\frac{1}{N}F(T,N) \sim \epsilon_\infty - \frac{\pi c}{6v_{\mathrm{s}}}T^2 \tag{4.2.11}$$

to obtain $c = 1$.

At the multicritical points M1: $(J^{YY}/J^{XZX}, J^{YZY}/J^{XZX}) = (\pm 1, 0)$, the system has three gapless k-linear Majorana points at $k = 0$, $\pm 2\pi/3$ (or at $k = \pm\pi/3$, π) and, by fitting the ground-state energy to the scaling form (4.2.10), we readily obtain $c = 3/2$. However, there are several different universality classes with $c = 3/2$ and we need more precise analysis. Using the method sketched in App. E, we see that the universality class is the level-1 SO(3) Wess–Zumino–Witten (WZW) model with $c = 3/2$ [149]. A similar argument shows that the points $(J^{YY}/J^{XZX}, J^{YZY}/J^{XZX}) = (0, \pm 1)$ (M2) correspond to the universality class of the level-1 SO(4) WZW with $c = 2$ with four Majorana points at $k = 0$, $\pm\pi/2$, and π (or at $k = \pm\pi/4, \pm 3\pi/4$). These two SO(N) criticalities fit into the series of general SO(N) critical

Table4.2.1 Quantum phase transitions in the model (4.1.1). For the multicritical points, the critical exponents may depend on how we deviate from the critical point. In most cases, we consider the deviation in the J^{YY}-direction. The exponent ν characterizes the spatial correlation length ξ_x as $\xi_x \sim |J^{YY} - J_c^{YY}|^{-\nu}$. (Table taken from Ref. [92].)

Phase boundaries	c	Universality	Exponents
P/C*-F$^{(y)}$, P/C*-AF$^{(y)}$, C-F$^{(x)}$/AF$^{(x)}$	1/2	Ising	$z = 1$, $\nu = 1$
C-P, C*-P, F$^{(x)}$-F$^{(y)}$, AF$^{(x)}$-AF$^{(y)}$	1	XY	$z = 1$
M1	3/2	SO(3)$_1$ WZW	$z = 1$, $\nu = 1$
M2	2	SO(4)$_1$ WZW	$z = 1$, $\nu = 1$
M3	–	1D hardcore boson	$z = 2$, $\nu = 1$

points discussed in Ref. [140]. At the point M3: $(J^{YY}/J^{XZX}, J^{YZY}/J^{XZX}) = (-4, -3)$ $[(4, -3)]$ where the two second-order phase boundaries merge, the quasi-particle dispersion takes the non-relativistic form $E_k \sim k^2$ near $k = 0$ $[E_k \sim (k - \pi)^2$ near $k = \pi]$ and the continuous quantum phase transition is characterized by the dynamical exponent $z = 2$.

4.2.3 Pseudospin and winding number

Because the Hamiltonian (4.2.5) belongs to the topological class BDI, the ground state is characterized by a topological invariant called the winding number [130, 150]. By using the Anderson pseudospin $\boldsymbol{d}(k)$

$$\boldsymbol{d}(k) = \epsilon_k \hat{\boldsymbol{e}}_z + \delta_k \hat{\boldsymbol{e}}_y, \tag{4.2.12}$$

the Hamiltonian is rewritten as

$$H = \sum_k (c_k^\dagger,\ c_{-k}) H(k) (c_k,\ c_{-k}^\dagger)^{\mathrm{T}}, \quad H(k) = \boldsymbol{d}(k) \cdot \boldsymbol{\sigma}, \tag{4.2.13}$$

where $\hat{\boldsymbol{e}}_y$, $\hat{\boldsymbol{e}}_z$ are the unit vectors in the y, z directions, respectively, and $\boldsymbol{\sigma} = (\sigma^x, \sigma^y, \sigma^z)$ represents the Pauli matrices. We define the angle in the yz-plane by using the normalized Anderson pseudospin:

$$\hat{\boldsymbol{d}}(k) = \frac{\boldsymbol{d}(k)}{|\boldsymbol{d}(k)|} = \cos\theta_k \hat{\boldsymbol{e}}_z + \sin\theta_k \hat{\boldsymbol{e}}_y. \tag{4.2.14}$$

The angle θ_k maps one-dimensional Brillouin Zone (circle) to the Hilbert space (circle). Then we can define the winding number W as the topological invariant of the mapping

$$W = \int_{\mathrm{B.Z.}} \frac{d\theta_k}{2\pi} = \begin{cases} +2 & (\text{C phase}) \\ -2 & (\text{C}^* \text{ phase}) \\ +1 & (\text{F}^{(x)}/\text{AF}^{(x)} \text{ phases}) \\ -1 & (\text{F}^{(y)}/\text{AF}^{(y)} \text{ phases}) \\ 0 & (\text{P phase}) \end{cases}. \tag{4.2.15}$$

The winding number has an integer value and changes only if the system undergoes quantum phase transition. That is, at critical points with $\epsilon_k = \delta_k = 0$, we cannot define the winding number. Therefore each phase has definite value of the winding number. These numbers correspond to the number of zero modes appearing at the edge of the system when the open boundary condition is imposed.

As an illustration, let us calculate the winding number at some points in the phase diagram (Fig. 4.2.1). The direction of the pseudospin in yz-plane is shown on the left side of Fig. 4.2.3. On the right side of Fig. 4.2.3, we show how the direction of the pseudospin changes as we vary the wave number k from $-\pi$ to π. We find that it winds around the unit circle once, twice, and zero times in Figs. 4.2.3(a), (b), and (c), respectively.

4.2.4 Order parameters

To clarify the physical picture of the ground state, we explain each term of the model (4.1.1). The first term in Eq. (4.1.1) is called the cluster interaction or the cluster stabilizer in quantum-information science. In the ground state of the model with $J^{YY} = J^{YZY} = 0$ and positive J^{XZX}, the string order parameter $O_{XZX} = \lim_{L\to\infty} O_{XZX}(L)$ is unity, where

$$O_{XZX}(L) = \left\langle \prod_{j=1}^{L-2} \bar{c}_{2j}\bar{c}_{2j+3} \right\rangle \tag{4.2.16}$$

in the fermion representation and

$$O_{XZX}(L) = (-1)^L \left\langle \sigma_1^x \sigma_2^y \left(\prod_{i=3}^{L-2} \sigma_i^z \right) \sigma_{L-1}^y \sigma_L^x \right\rangle \tag{4.2.17}$$

in the spin representation are called the string correlation functions of distance L [6,10,134]. The phase characterized by the non-vanishing string order parameter is generally called the cluster (C) phase. In the ground state of the model with $J^{XZX} = J^{YZY} = 0$ and positive J^{YY}, the antiferromagnetic (AF) order parameter $O_{YY} = \lim_{L\to\infty} O_{YY}(L)$ is unity, where

$$O_{YY}(L) = \left\langle \prod_{j=1}^{L-1} \bar{c}_{2j-1}\bar{c}_{2j+2} \right\rangle \tag{4.2.18}$$

is called the string correlation function of distance L. In the spin representation,

$$O_{YY}(L) = (-1)^{L-1} \langle \sigma_1^y \sigma_L^y \rangle \tag{4.2.19}$$

is called the spin correlation function of distance L. The phase characterized by the non-vanishing AF order parameter is the AF phase.

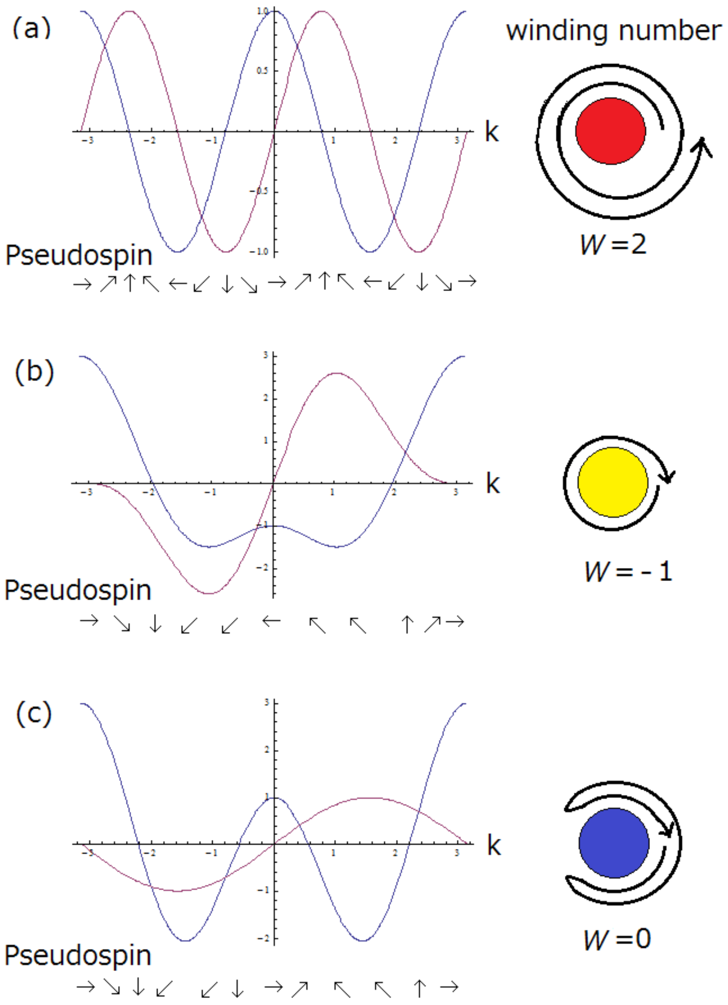

Figure4.2.3 The winding number: The blue curves represent ϵ_k, and red curves represent δ_k. The direction of the pseudospin is shown by the arrows. The winding number W counts how many times the pseudospin winds around the unit circle. Each figure corresponds to the points with parameters (a)$J^{YY}/J^{XZX} = 0, J^{YZY}/J^{XZX} = 0$ (C phase), (b)$J^{YY}/J^{XZX} = -2.0, J^{YZY}/J^{XZX} = 0$ (AF phase), (c)$J^{YY}/J^{XZX} = -1, J^{YZY}/J^{XZX} = -1$ (P phase) in Fig. 4.2.1. (Figure taken from Ref. [110].)

The last term (J^{YZY}) in Eq. (4.1.1) is similar to the cluster interaction. With the term there appears another topological phase, which we call the dual cluster (C*) phase. The phase is characterized by the dual string order parameter $O_{YZY} = \lim_{L\to\infty} O_{YZY}(L)$, where

$$O_{YZY}(L) = \left\langle \prod_{j=1}^{L-2} \bar{c}_{2j-1}\bar{c}_{2j+4} \right\rangle \tag{4.2.20}$$

in the fermion representation and

$$O_{YZY}(L) = \left\langle \sigma_1^y \sigma_2^x \left(\prod_{i=3}^{L-2} \sigma_i^z \right) \sigma_{L-1}^x \sigma_L^y \right\rangle \tag{4.2.21}$$

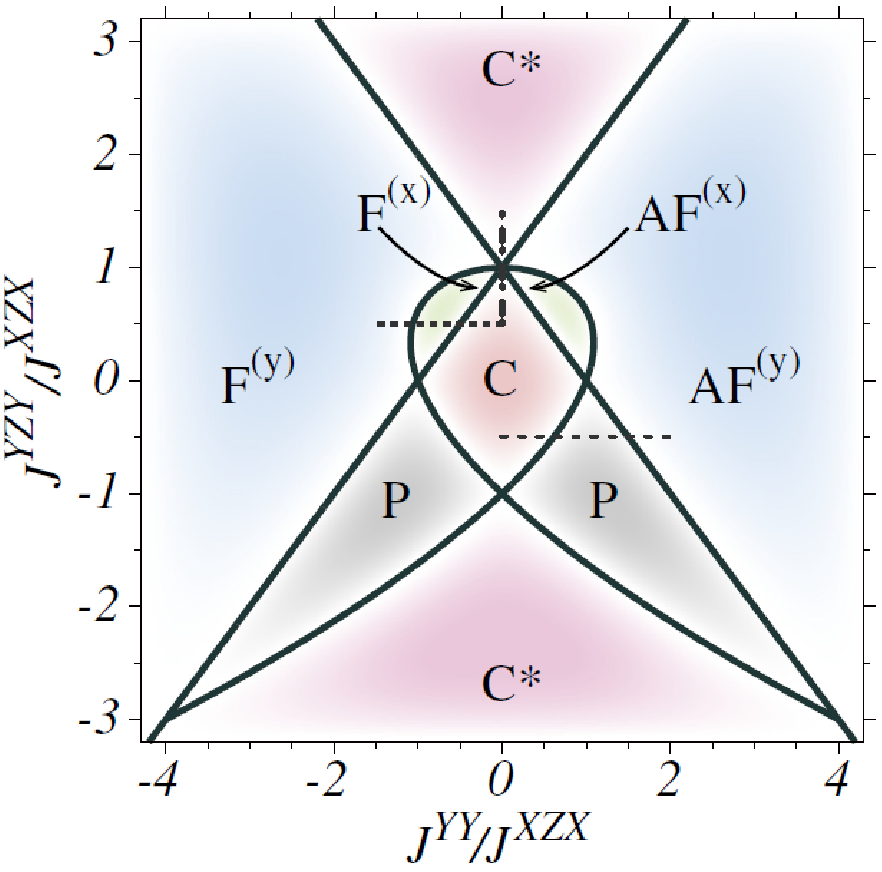

Figure4.2.4 Phase diagram of the generalized Kitaev model (4.1.1) for $J^{XZX} > 0$. On the thick solid curves, the excitation gap Δ_k vanishes at a certain k. C, C*, F, and AF represent cluster, dual cluster, ferromagnetic, and antiferromagnetic phases, respectively. The P phase cannot be characterized by string and (anti) ferromagnetic order parameters. The superscript represents the direction of the order. Each phase is determined by order parameters calculated with the iTEBD (Fig. 4.2.5). Along the thin dotted line and the dashed line, we calculated the entanglement spectrum in Fig. 4.2.6. (Figure taken from Ref. [92].)

in the spin representation are called the dual string correlation functions of distance L and characterizes the C* phase (see Sec. 4.2.1).

4.2.5 Entanglement properties

There is another way to characterize the phases found in Sec. 4.2.1 using quantum entanglement. Let us interpret these phases in terms of entanglement. To this end, we define two quantities, the entanglement entropy and the entanglement spectrum, which quantify entanglement [36, 46]. We divide the entire system into a subsystem A with the length L_{sub} and the rest B in a way symmetric with respect to the center of the system and measure the entanglement between them. We calculate the eigenvalues $\{\lambda_\beta\}$ of the reduced density matrix ρ_{A} of A which is obtained from the density matrix of the entire system ρ by tracing

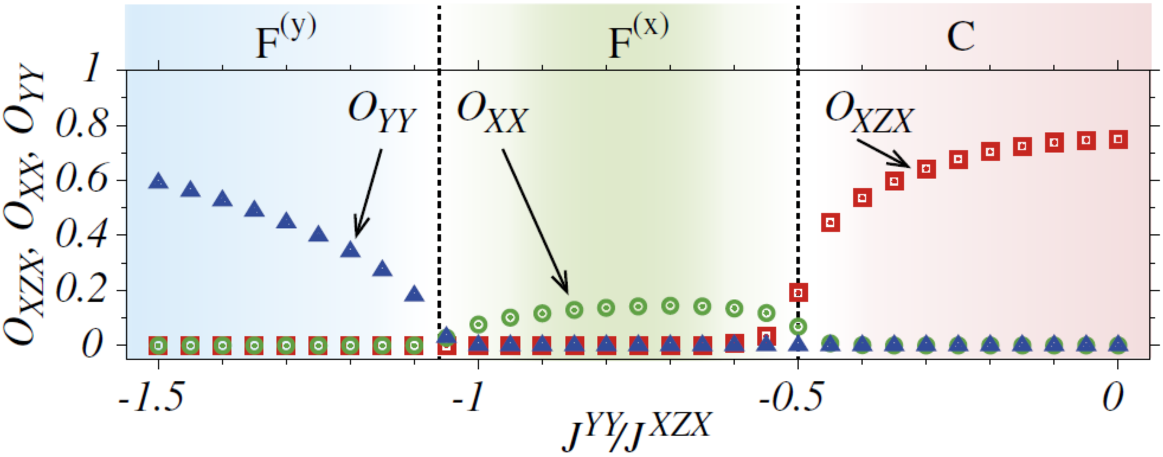

Figure4.2.5 String order parameters O_{XZX}, $O_{XX}, andO_{YY}$ along the thick dotted line ($J^{YY}/J^{XZX} \in [-1.5, 0], J^{YZY}/J^{XZX} = 0.5$) in Fig. 4.2.4 (d) ($J^{YZY}/J^{XZX} = 0.5$) by using the iTEBD with bond dimension $\chi = 60$. (Figure taken from Ref. [91].)

out the degree of freedom of the subsystem B:

$$\rho_{\mathrm{A}} = \mathrm{Tr}_{\mathrm{B}}\, \rho\ . \tag{4.2.22}$$

With the method developed in Refs. [151, 152], one obtains the reduced density matrix from the fermionic correlation functions for the excited states as well as the ground states. We define the entanglement entropy as the von Neumann entropy of the reduced density matrix ρ_{A}:

$$S = -\mathrm{Tr}(\rho_{\mathrm{A}} \ln \rho_{\mathrm{A}}). \tag{4.2.23}$$

On the other hand, the entanglement spectrum is defined as

$$\xi_\beta = -\ln \lambda_\beta, \tag{4.2.24}$$

where $\{\lambda_\beta\}$ are the eigenvalues of ρ_{A} [46]. Because we can consider the entanglement entropy as the thermal entropy at temperature 1 with some Hamiltonian with eigenenergies $\{\xi_\beta\}$, we can expect that the entanglement spectrum contains more information than entanglement entropy. Although the entanglement entropy and the entanglement spectrum are well-defined in the analysis of only the ground state, we expect that the entanglement entropy and the entanglement spectrum defined for the excited states can extract some physical properties in the excited states.

We characterize the phases in Fig. 4.2.1 by the entanglement spectrum [91]. Here we assume the open boundary condition. We focus on the number of degeneracy of the lowest level in the entanglement spectrum. It is the same as that of the ground states originating from the Majorana zero modes at the ends of the system. We thus confirm that for the generalized Kitaev model (4.1.1) the entanglement spectrum reflects the fictitious degree

Table4.2.2 The relation between the winding number and the number of degeneracy of the entanglement spectrum (bulk–edge correspondence). Dominant order parameter (OP) for each phase is also shown. (Table taken from Ref. [92].)

Phase	OP	Winding number	Degeneracy of the entanglement spectrum
C	O_{XZX}	2	four-fold
C*	O_{YZY}	-2	four-fold
$\mathrm{F}^{(x)}/\mathrm{AF}^{(x)}$	O_{XX}	1	two-fold
$\mathrm{F}^{(y)}/\mathrm{AF}^{(y)}$	O_{YY}	-1	two-fold
P	–	0	no degeneracy

of freedom appearing at the cut ends as in the case of other topological phases studied in previous works [46–48, 153].

Table 5.1.1 summarizes the relation between the winding number and the number of degeneracy of the lowest level in the entanglement spectrum. The former is calculated with the periodic boundary condition, while the latter is calculated with the open boundary condition and reflects the edge modes. We can clearly see that the absolute value of the winding number is equal to the number of zero-energy excitations in an open chain. This is a manifestation of the bulk–edge correspondence in the model (4.1.1). Note that the winding number or the degree of degeneracy of the entanglement spectrum alone does not tell anything about physical properties of the phases except for topological properties (e.g., the number of edge excitations). To determine the phases completely, we need to calculate the order parameters by other methods as we did in Sec. 4.2.1.

The entanglement entropy at the critical point shows a characteristic structure. The energy gap closes at $k = 0$, $k = \pm\pi$, and $k = \arccos\frac{J^{YY}}{2(1+J^{YZY})}$ on the line ($J^{YZY}/J^{XZX} = J^{YY}/J^{XZX} + 1$), the line ($J^{YZY}/J^{XZX} = -J^{YY}/J^{XZX} + 1$), and the curve (${J^{YY}/J^{XZX}}^2 - (1 - {J^{YZY}/J^{XZX}}^2)(1 + J^{YZY}/J^{XZX}) = 0$) in Fig. 4.2.4. In particular, at $(J^{YY}/J^{XZX}, J^{YZY}/J^{XZX}) = (0, -1)$, the energy gap closes at $k = \pm\frac{\pi}{4}, \pm\frac{3\pi}{4}$. At these critical points, the entanglement entropy diverges logarithmically as the length of the subsystem. The critical point $J^{YY}/J^{XZX} = 0, J^{YZY}/J^{XZX} = 1$ would be interesting. In fact, the entanglement entropy in Fig. 4.2.7 shows logarithmic behavior, and we find that the central charge is 2 from the coefficient. This is because there are four Ising dispersions as shown in Fig. 4.2.2(a) $(4 \times \frac{1}{2})$. Further, the critical point $(J^{YY}/J^{XZX} = 1, J^{YZY}/J^{XZX} = 0)$ are studied in Ref. [134] and the corresponding central charge is $\frac{3}{2}$. This is because there are three Ising dispersions $(3 \times \frac{1}{2})$.

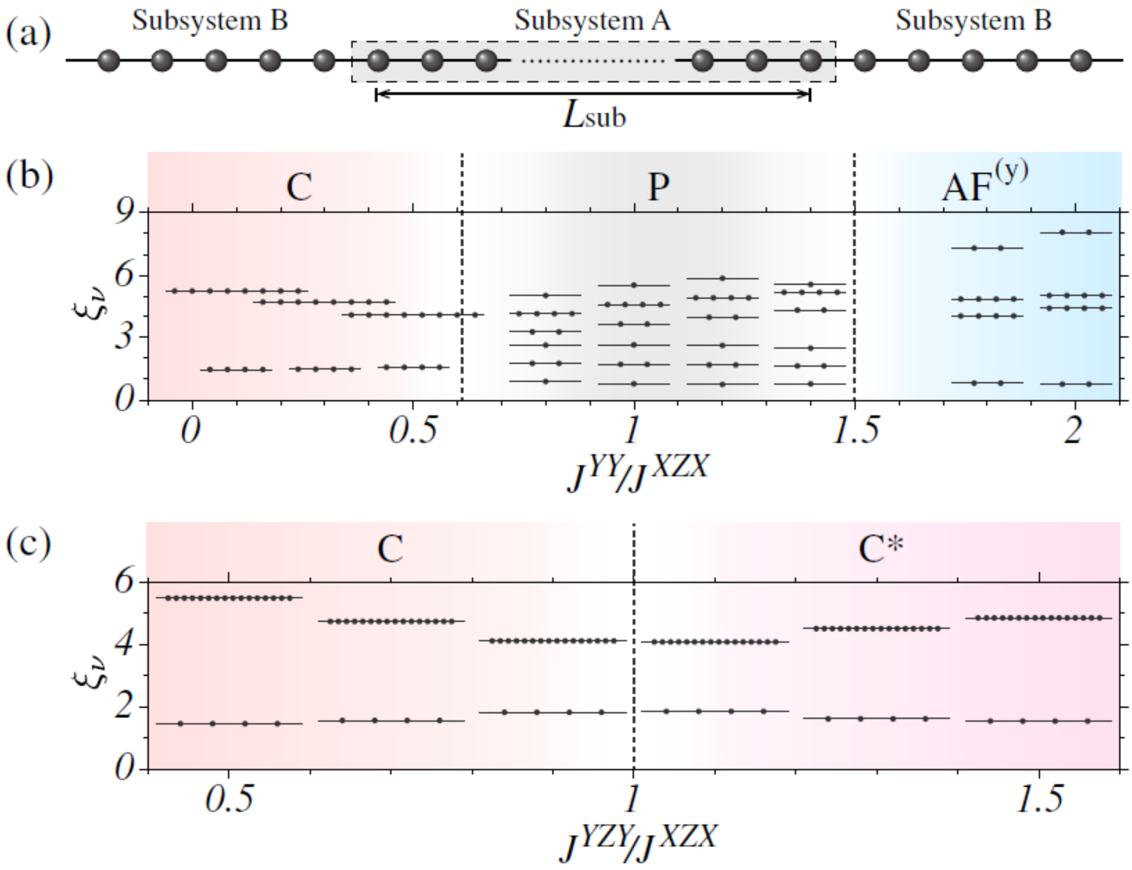

Figure4.2.6 (a) Schematics of subsystems A and B. The size of the system is $N = 503$ and that of the subsystem is $L_{\mathrm{sub}} = 249$. (b) The entanglement spectrum for $J^{YZY}/J^{XZX} = -0.5$ indicated by the horizontal dotted line in Fig. 4.2.4. (c) The entanglement spectrum for $J^{YY}/J^{XZX} = 0$ indicated by the vertical dashed line in Fig. 4.2.4. The degeneracy in the lowest level is four, four, two, one (no degeneracy) in C, C*, AF, P phases, respectively. (Figure taken from Ref. [91].)

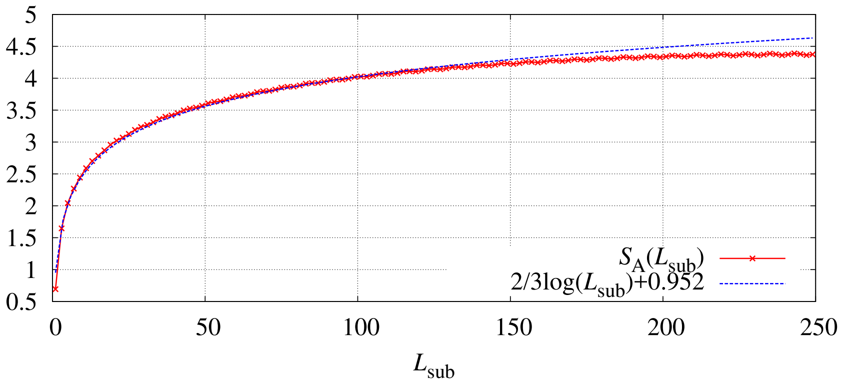

Figure4.2.7 The entanglement entropy at the critical point $(J^{YY}/J^{XZX}, J^{YZY}/J^{XZX}) = (0, 1)$: We can see that the it behaves logarithmically and the central charge is 2. N =503, $L_{\mathrm{sub}} = 249$, calculated with the exact diagonalization. (Figure taken from Ref. [110].)

4.3 Dynamics

In the previous section, the ground-state phases of the model (4.1.1) and topological quantum phase transitions were investigated from the viewpoint of the string correlation functions and entanglement. In this section, we study the dynamical properties of the model (4.1.1) when we change in time an interaction parameter across these critical points at a finite speed. The sweep dynamics captures the effects of the low-energy excitations more clearly than the quench dynamics in which the parameter is changed abruptly and all the excitations contribute to the dynamics. In Sec. 4.3.1, we set the initial condition paying attention to its parity. We study the dynamics under the sweep from the C phase to the AF$^{(y)}$ phase in Sec. 4.3.2 and to the C* phase in Sec. 4.3.3. In the former case, the ground-state degeneracy changes during the sweep. In the latter case, on the contrary, the ground-state degeneracy does not change in the sweep dynamics. In the dynamics, both the correlation functions and the entanglement entropy exhibits spatially periodic structure. On top of that, we observe the oscillating and splitting structure in the levels in the entanglement spectrum. We understand these structure by using excited states in Sec. 4.3.4 and Sec. 4.3.5. In Sec. 4.3.6, we confirm that the entanglement spectrum reflects the modes appearing at the cut ends by using a dimer model.

4.3.1 Parity

In the fermion representation, AF$^{(y)}$, C, and C* phases are the topological phases with ground-state degeneracy. As was pointed out in Refs. [82–85], the topological properties of the initial state strongly affect the time evolution of the system. Since the energies of the two lowest bogolons η_1 and η_2 vanish ($E_1 = E_2 = 0$) in the C phase, the states $\eta_1^\dagger |\mathrm{vac}\rangle$, $\eta_2^\dagger |\mathrm{vac}\rangle$, and $\eta_2^\dagger \eta_1^\dagger |\mathrm{vac}\rangle$ as well as the vacuum state $|\mathrm{vac}\rangle$ are the ground states. In the case of the Kitaev chain [20], the states are labeled by the fermionic parity operator defined by

$$\prod_{i=1}^{N} \sigma_i^z = \prod_{i=1}^{N} \mathrm{i}\bar{c}_{2i}\bar{c}_{2i-1}, \tag{4.3.1}$$

which is crucial to understand the topological properties.

In the cluster model, on the other hand, the states are labeled by the following set of parity operators defined by [134, 138]

$$\prod_{i\in\mathrm{even}} \sigma_i^z = \prod_{i\in\mathrm{even}} \mathrm{i}\bar{c}_{2i}\bar{c}_{2i-1}, \quad \prod_{i\in\mathrm{odd}} \sigma_i^z = \prod_{i\in\mathrm{odd}} \mathrm{i}\bar{c}_{2i}\bar{c}_{2i-1}. \tag{4.3.2}$$

In fact, the above two operators are conserved anywhere along the line $J^{YY} = 0$ and crucial in understanding the topological properties of the C phase. In the following, the initial state is prepared in the vacuum $|\mathrm{vac}\rangle$ of the Bogoliubov operators that is a ground state of the model (4.1.1). Because there is an ambiguity to construct the zero modes η_1 and η_2 in the initial state, we use the following expression for them:

$$\eta_1 = \frac{1}{2}(\bar{c}_1 - \mathrm{i}\bar{c}_{2N}), \quad \eta_2 = \frac{1}{2}(\bar{c}_3 - \mathrm{i}\bar{c}_{2N-2}), \tag{4.3.3}$$

where the eigenvalues of the fermionic parity operators (4.3.2) in the vacuum are both -1.

4.3.2 C to AF$^{(y)}$

We first study the dynamics during an interaction sweep across the critical point between the C and AF$^{(y)}$ phases with the open boundary condition. In this case, the degree of degeneracy of the ground states is four and two in the C and AF$^{(y)}$ phases, respectively. Therefore the situation is similar to the Kitaev model where the mismatch between the degeneracies in the topological and trivial phases occurs [84, 85]. Let us set $J^{YZY} = 0$ and consider the following time-dependent Hamiltonian:

$$H_1(t) = -J^{XZX} \sum_{i=1}^{N-2} (c_i^\dagger - c_i)(c_{i+2}^\dagger + c_{i+2}) - J^{YY}(t) \sum_{i=1}^{N-1} (c_i^\dagger + c_i)(c_{i+1}^\dagger - c_{i+1}), \tag{4.3.4}$$

where the interaction parameter changes linearly in time during the sweep time τ as

$$J^{YY}(t)/J^{XZX} = 2t/\tau, \quad 0 \le t \le \tau \tag{4.3.5}$$

tracing the path shown by the dashed line ‘P1’ in Fig. 4.2.1. At $t = 0$, $H_1(t)$ coincides with the cluster model and it gradually evolves into the final form $(J^{YY}/J^{XZX}, J^{YZY}/J^{XZX}) = (2, 0)$ whose instantaneous ground state shows the AF$^{(y)}$ phase. Note that at $t = \tau/2$ the system passes through the multicritical point M1 into the AF$^{(y)}$ phase (see Fig. 4.2.1). We calculated the distance (ℓ) dependence of the string correlation function $O_{YY}(\ell)$ [Eq. (4.2.18)] and the block-size dependence of the entanglement entropy $S(\ell)$ by using the time-dependent Bogoliubov transformation explained in Sec. 3.2 [143, 144], where ℓ is defined as Fig. 4.3.1. We show the ℓ-dependence of the string correlation function at time $t/\tau = 0.6, 0.8, 1$ for different sweep times $\tau = 25$ and 200 in Figs. 4.3.2(a) and (b), respectively. We can clearly see a triple-periodic structure in the ℓ-dependence for larger τ, i.e., slower sweep. We also plot the block-site (ℓ) dependence of the entanglement entropy at time $t/\tau = 0.6, 0.8, 1$ with $\tau =$ 25 and 200 in Figs. 4.3.2(c) and (d), respectively. We can clearly see a similar triple-periodic structure in the block-size dependence of the entanglement entropy for the slower sweep.

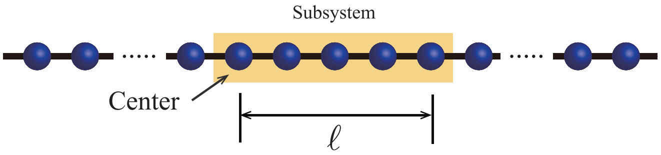

Figure4.3.1 The string correlation functions $\mathcal{O}_{YY}$ and O_{YZY} are measured between the central site (site 1) and the other at a distance ℓ. In calculating the entanglement entropy, we take a block of ℓ adjacent sites to the right of the central site. (Figure taken from Ref. [92].)

To see the change in the topological properties during the sweep, we calculated the time dependence of the entanglement spectrum. We choose the subsystem A of size $L_{\mathrm{sub}} = 49$ located symmetrically around the center of the entire system of length $N = 101$ (see Fig. 4.3.3). In Figs. 4.3.4(a)-(d), we show the lowest four entanglement levels for the sweep times $\tau = 25, 50, 100, 200$. Till the time $t = \tau/2$ when the instantaneous Hamiltonian undergoes a quantum phase transition from the C phase to the AF$^{(y)}$ phase, the levels remain four-fold degenerate. After passing the critical point, the degeneracy resolves: For faster sweeps the four levels oscillate in time [see Figs. 4.3.4(a)-(c)], whereas for slower sweeps the levels split into two pairs [see Fig. 4.3.4(d)].

4.3.3 C to C*

Next we turn to the dynamics during an interaction sweep across the critical point between the C and C* phases with the open boundary condition. Because the degree of degeneracy of the ground states is four in both the C and C* phases, the mismatch between the degeneracies does not occur. Therefore, the situation is different from that in Refs. [84,85] and in Sec. 4.3.2. Let us now set $J^{YY} = 0$ and consider the following time-dependent Hamiltonian:

$$H_2(t) = -J^{XZX} \sum_{i=1}^{N-2} (c_i^\dagger - c_i)(c_{i+2}^\dagger + c_{i+2}) + J^{YZY}(t) \sum_{i=1}^{N-2} (c_i^\dagger + c_i)(c_{i+2}^\dagger - c_{i+2}). \tag{4.3.6}$$

As the interaction parameter J^{YZY} changes linearly during the sweep time τ as

$$J^{YZY}(t)/J^{XZX} = 2t/\tau, \quad 0 \le t \le \tau\ , \tag{4.3.7}$$

the Hamiltonian evolves from the cluster model into the one with $(J^{YY}/J^{XZX}, J^{YZY}/J^{XZX}) = (0, 2)$ whose instantaneous ground state shows C* phase. Note that the $c = 2$ multicritical point M2 is passed at time $t = \tau/2$ (see the dashed line shown as ‘P2’ in Fig. 4.2.1).

We calculated the ℓ-dependence of the dual string correlation function $O_{YZY}(\ell)$ [Eq. (4.2.20); with ℓ being the distance between the two end points] and the block entanglement entropy $S(\ell)$ (with ℓ being the size of the block) in the same way as in the previous

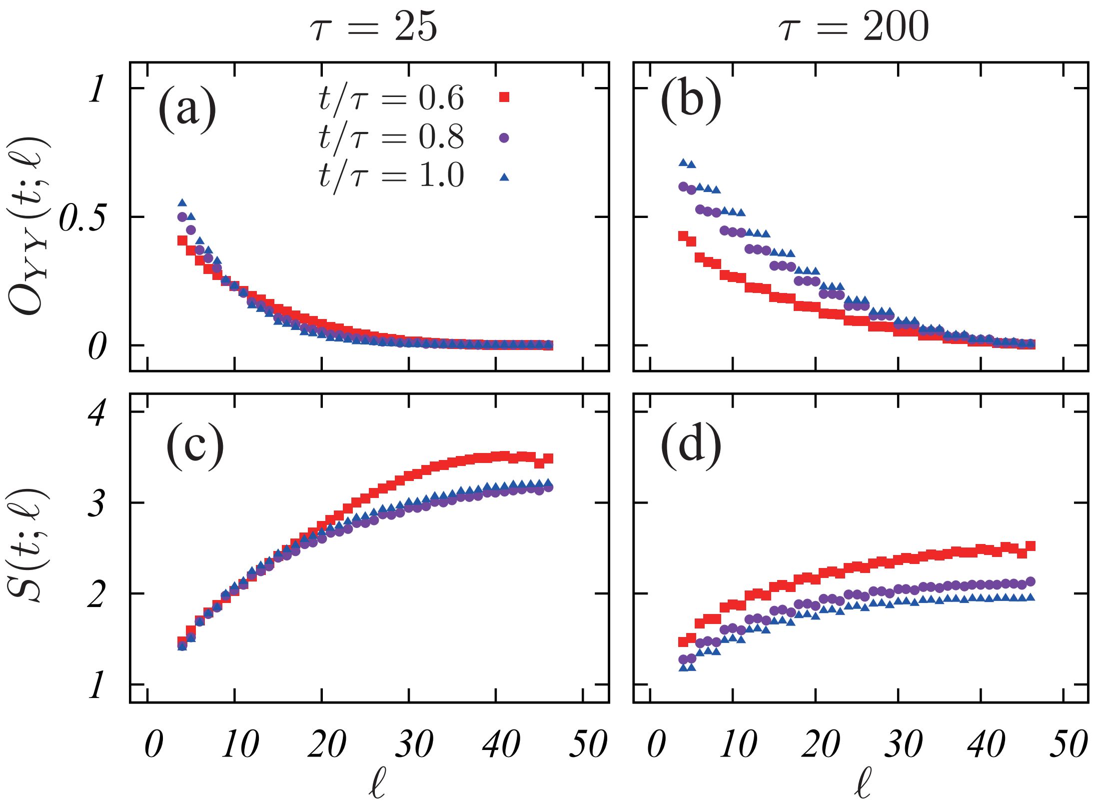

Figure4.3.2 Sweep dynamics from the C phase to the AF$^{(y)}$ phase. ℓ denotes the distance between the two end points (for the correlation function) or the size of the block (for the entanglement entropy). See Fig. 4.3.1 for more details. The system size is $N = 101$. (a) The distance dependence of the string correlation function $O_{YY}(\ell)$ at $t/\tau = 0.6, 0.8, 1$ with $\tau = 25$. (b) The same plot for $\tau = 200$. (c) The block-size dependence of the entanglement entropy $S(\ell)$ at $t/\tau = 0.6, 0.8, 1$ with $\tau = 25$. (d) The same plot for $\tau = 200$. (Figure taken from Ref. [92].)

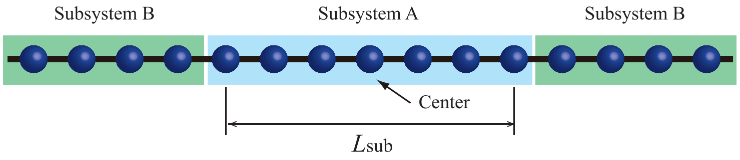

Figure4.3.3 Schematic of subsystems A and B. (Figure taken from Ref. [92].)

section. We show the ℓ-dependence of the dual string correlation function at different elapsed times $t/\tau = 0.6, 0.8, 1$ in Figs. 4.3.5(a) and (b) for $\tau = 25$ and 200, respectively. A period-4 structure in the ℓ-dependence is clearly seen for slower sweep (larger τ). Next, we calculated the block-size (ℓ) dependence of the entanglement entropy at elapsed times $t/\tau = 0.6, 0.8, 1$. The results for $\tau = 25$ and 200 are shown in Figs. 4.3.5(c) and (d), respectively. As in the case of the C-AF$^{(y)}$ sweep in Sec. 4.3.2, the block-size dependence of the entanglement entropy exhibits a similar periodic structure to that of the dual string correlation function $O_{YZY}(\ell)$.

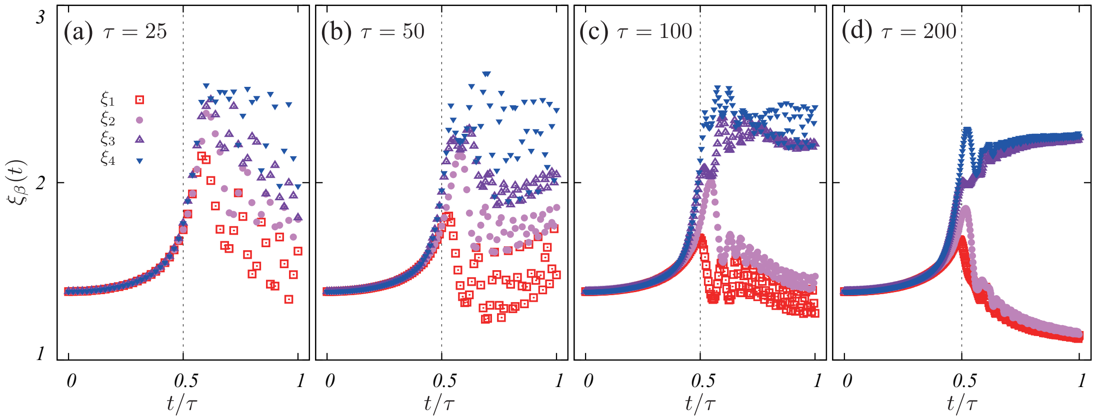

Figure4.3.4 Sweep dynamics from the C phase to the $\mathrm{AF}^{(y)}$ phase. We calculate the entanglement spectrum with $N = 101$ and $L_{\mathrm{sub}} = 49$ (see Fig. 4.3.3). The time evolution of the lowest four entanglement levels $\xi_\beta(t)$ $(\beta = 1, 2, 3, 4)$ with (a) $\tau = 25$, (b) $\tau = 50$, (c) $\tau = 100$, and (d) $\tau = 200$. (Figure taken from Ref. [92].)

We calculated the time-evolution of the entanglement spectrum to study the topological properties in detail. We take the same subsystem as in the previous section (see Fig. 4.3.3). In Figs. 4.3.6(a)-(d), we plot the lowest four entanglement levels for different sweep times $\tau = 25, 50, 100, 200$. Up to the time $t = \tau/2$, when the instantaneous Hamiltonian is located at the multicritical point M2 between the C phase and the C* phase, the levels retain four-fold degenerate. After passing the critical point, the degeneracy is lifted: For faster sweeps, the four levels oscillate in time [see Figs. 4.3.6(a)-(b)], while for slower sweeps the levels split into pairs [see Fig. 4.3.6(d)].

4.3.4 Periodic structure in correlation functions and the entanglement entropy

To clarify the origin of the periodic structure in the string correlation functions and the entanglement entropy found in the sweep dynamics shown in the previous sections, we calculate the string correlation functions and the entanglement entropy in certain excited states. Since it is expected that for slow sweeps the main contribution to the dynamical properties comes from low-lying excited states [91], we may focus only on the states with a single bogolon. That is, we consider only the excited states that are obtained by applying a single bogolon operator $\eta_\alpha^\dagger$ to the Bogoliubov vacuum:

$$|\alpha\rangle = \eta_\alpha^\dagger|\mathrm{vac}\rangle \quad (\alpha = 1, 2, \ldots, N), \tag{4.3.8}$$

where the Bogoliubov energy E_α is the eigenvalue of the instantaneous Hamiltonian at some given time t and is assumed to be labeled in the ascending order. The expression of the string

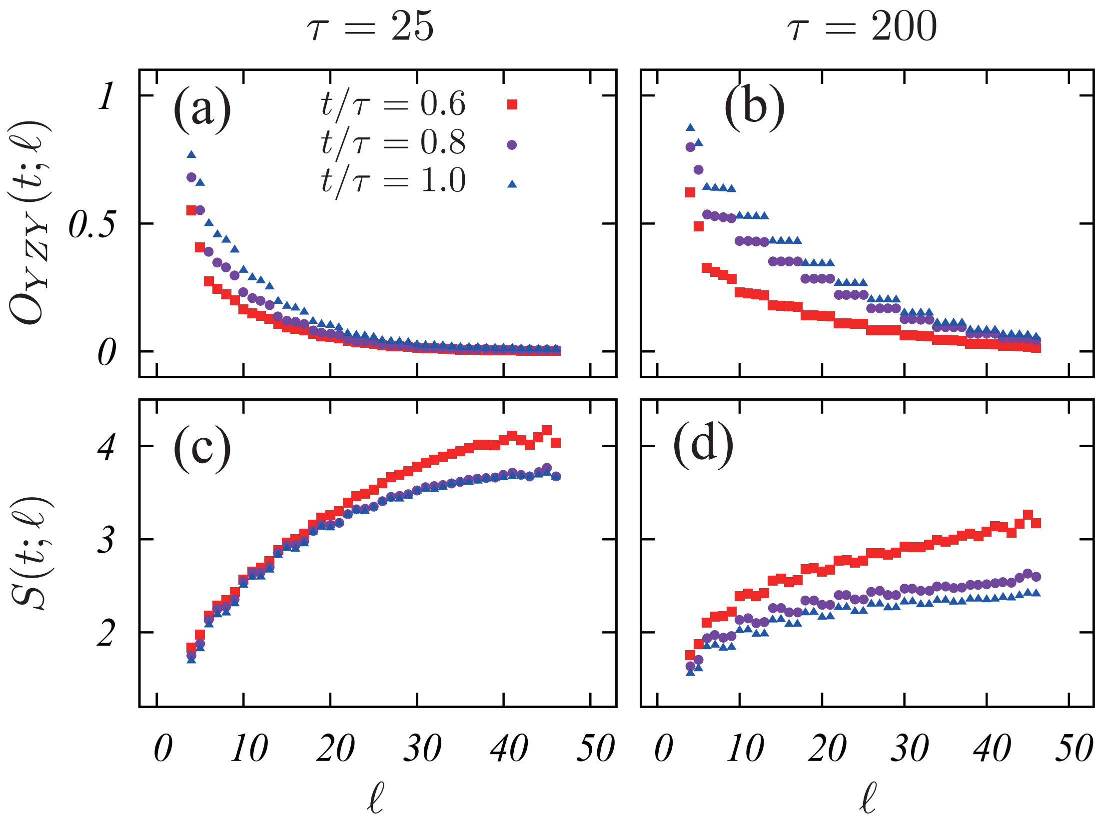

Figure4.3.5 Sweep dynamics from the C phase to the C* phase. ℓ denotes the distance between the two end points (for the string correlation function) or the size of the block (for the entanglement entropy). The system size is $N = 101$. (a) The distance dependence of the string correlation function $O_{YY}(\ell)$ at $t/\tau = 0.6, 0.8, 1$ with $\tau = 25$. (b) The same plot for $\tau = 200$. (c) The block-size dependence of the entanglement entropy $S(\ell)$ at $t/\tau = 0.6, 0.8, 1$ with $\tau = 25$. (d) The same plot for $\tau = 200$. (Figure taken from Ref. [92].)

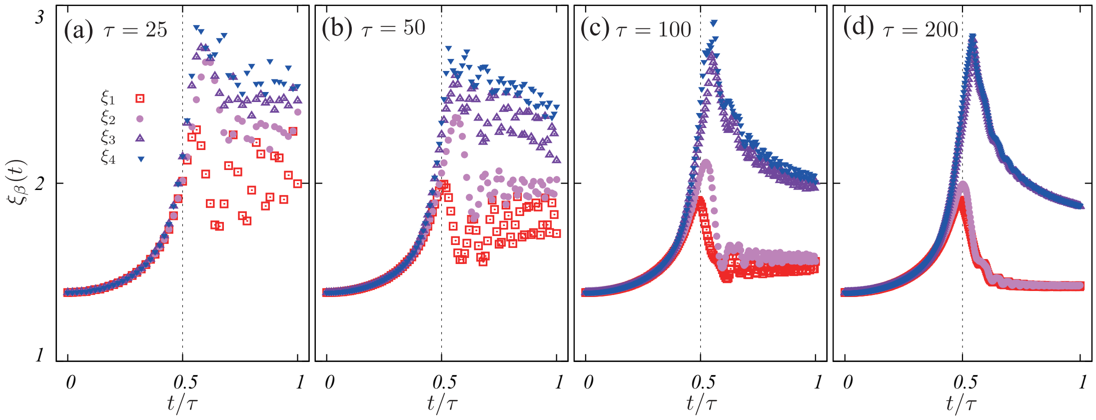

Figure4.3.6 Sweep dynamics from the C phase to the C* phase. We calculate the entanglement spectrum with $N = 101$ and $L_{\rm sub} = 49$. The time evolution of the lowest four entanglement levels $\xi_\beta(t)$ ($\beta = 1, 2, 3, 4$) with (a) $\tau = 25$, (b) $\tau = 50$, (c) $\tau = 100$, and (d) $\tau = 200$. (Figure taken from Ref. [92].)

correlation function $O_{XZX}(\ell)$ calculated for the excited states $|\alpha\rangle$ [see Eq. (3.1.26)]

$$O_{XZX}(\ell)_\alpha \equiv \left\langle \eta_\alpha \left\{ \mathcal{B}_1\mathcal{B}_2 \sum_{j=3}^{\ell-2} \left(\mathcal{A}_j\mathcal{B}_j\right) \mathcal{A}_{\ell-1}\mathcal{A}_\ell \right\} \eta_\alpha^\dagger \right\rangle \tag{4.3.9}$$

contains $(2\ell-2)$ fermion operators $\mathcal{A}$ and $\mathcal{B}$ [see Eq. (3.1.25) for the definition], where ℓ is measured from the center of the system as shown in Fig. 4.3.1. As we have additional contractions coming from the bogolon:

$$\begin{aligned} \langle \eta_\alpha \mathcal{A}_i \rangle &= \langle \mathcal{A}_i \eta_\alpha^\dagger \rangle = \phi_{i\alpha}, \\ \langle \eta_\alpha \mathcal{B}_i \rangle &= -\langle \mathcal{B}_i \eta_\alpha^\dagger \rangle = -\psi_{i\alpha}, \\ \langle \eta_\alpha \eta_\beta^\dagger \rangle &= \delta_{\alpha\beta} \ , \end{aligned} \tag{4.3.10}$$

we must adopt the method using the Pfaffian of the matrix of order $(2\ell-2)$ instead of determinant of matrix of order $(\ell-1)$ as shown in Sec. 3.1.3.

With the above setup, we calculated the correlation functions in the excited states $|\alpha\rangle$ of the instantaneous Hamiltonians $H_{1,2}(t=\tau)$ at the final time. We show the distance ℓ dependence of the string correlation functions $O_{YY}(\ell)_\alpha$ for $H_1(t=\tau)$ [i.e., H_{GC} with $(J^{YY}/J^{XZX}, J^{YZY}/J^{XZX}) = (2,0)$] in Fig. 4.3.7(a) and $O_{YZY}(\ell)_\alpha$ for $H_2(t=\tau)$ [i.e., $(J^{YY}/J^{XZX}, J^{YZY}/J^{XZX}) = (0,2)$] in Fig. 4.3.7(b). As mentioned before, the bogolons with zero energy are responsible for the ground-state degeneracy. Only the first bogolon has zero energy [Figs. 4.3.7(a) and (c)] in the AF$^{(y)}$ phase, whereas both the first and second bogolons have zero energy [Figs. 4.3.7(b) and (d)] in the C* phase. In fact, the string correlation functions in the zero-energy excited states are the same as those in the Bogoliubov vacuum, since these states, together with $|\mathrm{vac}\rangle$, form the degenerate set of ground states. In Figs. 4.3.7(a) and (b), we show the string correlation functions for the ground states and the bogolon excited states with *finite* energies. For the bogolon states with finite energy, the spatially periodic structures are observed in both cases. The periods 3 [for $H_1(t=\tau)$] and 4 [for $H_2(t=\tau)$] may be traced back to the wave lengths of the corresponding bogolons.

Next we calculated the entanglement entropy for the same single bogolon states. To obtain the entanglement entropy for excited states, we calculate the reduced density matrix by using Eq. (4.2.22), where the density matrix ρ is defined for the excited state in question. Then, the entanglement entropy for excited states is readily obtained by applying Eq. (4.2.23). We take a block of ℓ adjacent sites as the subsystem as shown in Fig. 4.3.1. We show the block-size dependence of the entanglement entropy at $(J^{YY}/J^{XZX}, J^{YZY}/J^{XZX}) = (2,0)$ in Fig. 4.3.7(c) and at $(J^{YY}/J^{XZX}, J^{YZY}/J^{XZX}) = (0,2)$ in Fig. 4.3.7(d). Again, the excitation of a single zero-energy bogolon yields the same entanglement entropy as that for the Bogoliubov vacuum. In Figs. 4.3.7(c) and (d), we show the entanglement entropy for

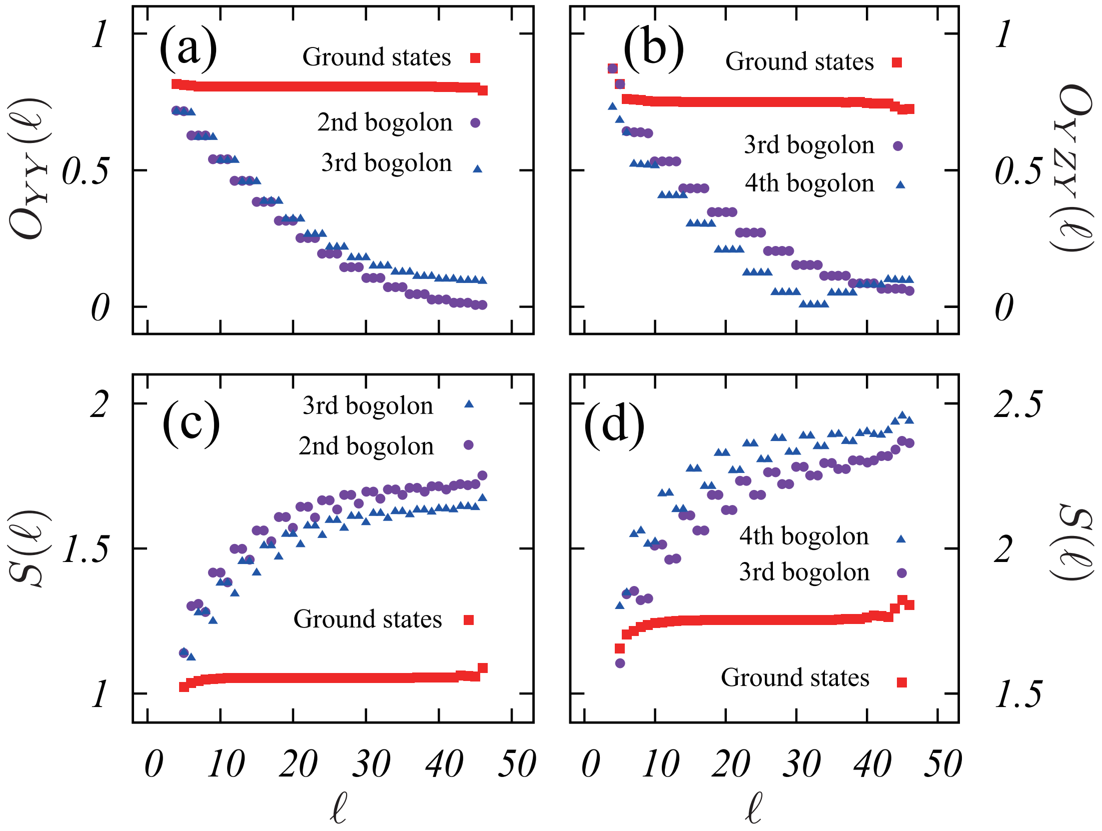

Figure4.3.7 The correlation functions and the block-size (ℓ) dependence of entanglement entropy with $N = 101$. (a) The distance dependence of the string correlation function $O_{YY}(\ell)$ in the ground state and the single bogolon states $\eta_2^\dagger|\text{vac}\rangle$ and $\eta_3^\dagger|\text{vac}\rangle$ for $(J^{YY}/J^{XZX}, J^{YZY}/J^{XZX}) = (2, 0)$. A triple structure appear for the single bogolon states with a finite energy. (b) The distance dependence of the string correlation function $O_{YZY}(\ell)$ in the ground state and the single bogolon states at $(J^{YY}/J^{XZX}, J^{YZY}/J^{XZX}) = (0, 2)$. A quadruple structure appear for the single bogolon states with a finite energy. (c) The block-size dependence of the entanglement entropy $S(\ell)$ in the ground state and the single bogolon states at $(J^{YY}/J^{XZX}, J^{YZY}/J^{XZX}) = (2, 0)$. (d) The block-size dependence of the entanglement entropy $S(\ell)$ in the ground state and the single bogolon states at $(J^{YY}/J^{XZX}, J^{YZY}/J^{XZX}) = (0, 2)$. (Figure taken from Ref. [92].)

the ground states $|\text{vac}\rangle$ and the two finite-energy bogolon states $|\alpha\rangle = \eta_\alpha^\dagger|\text{vac}\rangle$ ($\alpha = 2, 3$ or $3, 4$) of the two instantaneous Hamiltonians $H_1(t = \tau)$ and $H_2(t = \tau)$, respectively. For the bogolon states with finite energies, we observe spatially periodic (period-3 and 4) structures that are reminiscent of what we have seen during the sweep after passing the critical points [i.e., $t > \tau/2$; see Figs. 4.3.2(d) and 4.3.5(d)]. From these results, we may conclude that the single-bogolon state $|\alpha\rangle$ with the lowest non-zero energy dominates the dynamics in slow sweeps and that the periodic structure found in the string correlation functions and the entanglement entropy (see Figs. 4.3.2 and 4.3.5) essentially originates from it. We can observe these structures when the sweep time is larger enough than typical time at the critical point (i.e. $\tau > N$), which is a manifestation of the breakdown of adiabaticity.

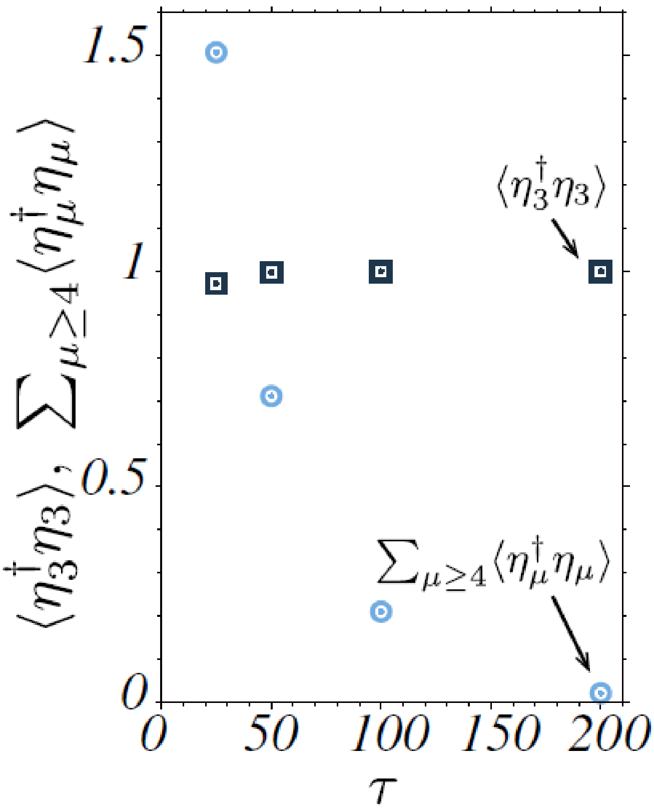

Figure4.3.8 The expectation values of the number of bogolons in the final state of C-C* sweep. (Figure taken from Ref. [91].)

To see explicitly the breakdown of adiabaticity, we calculated the number of bogolons excited during the sweep. In Fig. 4.3.8, we show the expectation values of the Bogoliubov number operator $\eta_\mu^\dagger\eta_\mu$ with respect to the final state ($t = \tau$) of the C-C* sweep. As the sweep rate becomes slower, the sum of expectation value of the bogolon whose index is larger than 3 decreases. On the other hand, that of the third bogolon, which has the lowest finite energy, approaches to 1. This indicates that the third bogolon dominates the slower sweep (larger τ). Because the typical time scale at the critical point is given by the system size N, the third bogolon must be excited for sufficiently slow sweep.

This breakdown of adiabaticity is due to the topological properties of the system. In the C and C* phases, the four ground states $|\mathrm{vac}\rangle$, $\eta_1^\dagger|\mathrm{vac}\rangle$, $\eta_2^\dagger|\mathrm{vac}\rangle$, $\eta_2^\dagger\eta_1^\dagger|\mathrm{vac}\rangle$ are labeled by the eigenvalues of two parity operators (4.3.2). In the AF$^{(y)}$ phase, the two ground states $|\mathrm{vac}\rangle$, $\eta_1^\dagger|\mathrm{vac}\rangle$ are labeled by the eigenvalues of the parity operators (4.3.1). As shown in Sec. 4.3.2, the system undergoes the phase transition between the C and AF$^{(y)}$ phases. Because these two phases differ in the degree of the ground-state degeneracy, some of the degenerate ground states must leave the ground state subspace after the sweep and the breakdown of adiabaticity occurs for the reason discussed in Refs. [84,85]. In Fig. 4.3.9(a), we show the low-lying energy spectrum of the instantaneous Hamiltonian along the path P1 in Fig. 4.2.1. Two of the four states, which constitute the degenerate ground states in the C phase, are lifted up as we increase the parameter J^{YY}/J^{XZX} across the critical point M1 ($J^{YY}/J^{XZX} = 1$). Since the initial state in the sweep dynamics, i.e., $|\mathrm{vac}\rangle$, is one of the two states leaving the ground-state subspace, the initial state must be lifted to an excited state of the final Hamiltonian in the AF$^{(y)}$ side even after a slow sweep.

On the other hand, the degree of the degeneracy is four both in the C and C* phases as shown in Sec. 4.3.3. In this case, the breakdown of adiabaticity is *not* due to the mismatch between the numbers of the ground states as in the case of Sec. 4.3.2. Rather the system size matters in the following manner. The model (4.3.6) is rewritten as two independent Kitaev chains [see Figs. 2.3.3(a) and (c)]:

$$\begin{aligned} H_2(t) &= H_{2,\mathrm{odd}}(t) + H_{2,\mathrm{even}}(t), \\ H_{2,\mathrm{odd}}(t) &= J^{XZX} \sum_{i\in\mathrm{odd}} (-c_i + c_i^\dagger)(c_{i+2} + c_{i+2}^\dagger) \\ &\quad + J^{YZY}(t) \sum_{i\in\mathrm{odd}} (c_i + c_i^\dagger)(-c_{i+2} + c_{i+2}^\dagger), \\ H_{2,\mathrm{even}}(t) &= J^{XZX} \sum_{i\in\mathrm{even}} (-c_i + c_i^\dagger)(c_{i+2} + c_{i+2}^\dagger) \\ &\quad + J^{YZY}(t) \sum_{i\in\mathrm{even}} (c_i + c_i^\dagger)(-c_{i+2} + c_{i+2}^\dagger). \end{aligned} \tag{4.3.11}$$

The energy-level structure of the Kitaev chain near the transition point is qualitatively different depending on the parity of the system size as pointed out in Ref. [83]; when the size of the chain is even, a level crossing between zero-energy level and finite one occurs at the critical point, while we observe an avoided level crossing when the size of the chain is odd. We show the change in the low-lying energy spectrum along the path P1 for the system sizes $N = 101 = 51 + 50$ and $N = 102 = 51 + 51$ in Figs. 4.3.9(b) and (c), respectively. We observe the level crossing for the former case and the avoided level crossing for the latter case. In the case of $N = 101$ studied in Sec. 4.3.3, two of the four degenerate ground states in the C phase are lifted and two of excited states come down to merge with the ground-state level in the C* side as we increase the parameter J^{YZY}/J^{XZX} [See Fig. 4.3.9(b)]. Since we choose the initial state in the sweep dynamics from the ground states which are lifted to excited states, we observe the breakdown of adiabaticity in the dynamics.

4.3.5 Oscillating and splitting structures of the entanglement spectrum

We elucidate the origin of the oscillating and splitting structures of the entanglement spectrum in dynamics shown in Figs. 4.3.4(a)-(d) and 4.3.6(a)-(d). In the previous section, we

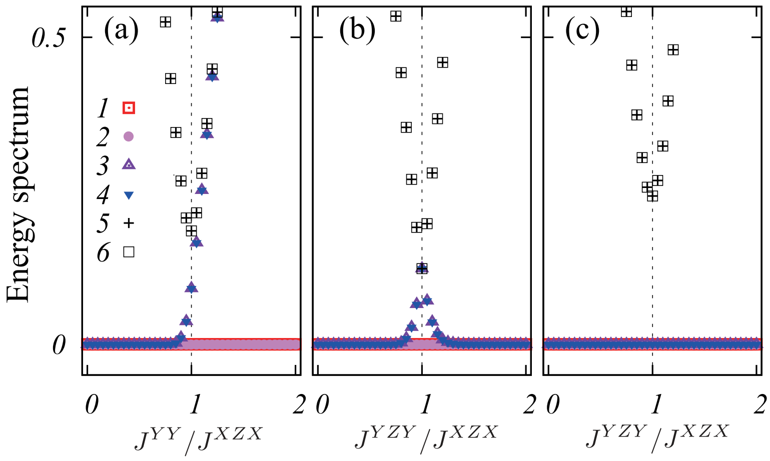

Figure4.3.9 The plot of the lowest-lying six energies of $H_{\rm GC}$ along the path 'P1' or 'P2' (see Fig. 4.2.1). (a) Along the path P1 ($J^{YZY}=0$) for $N=101$. Along the path P2 ($J^{YY}=0$) for $N=101$ [(b)], and for $N=102$ [(c)]. The level crossing occurs at $J^{YZY}/J^{XZX}=1$ for $N=101$, while an avoided crossing occurs for $N=102$. (Figure taken from Ref. [92].)

concluded that the bogolon states with lowest non-zero energy play a crucial role in the sweep dynamics across the critical points. In the following, we consider the case of the sweep dynamics from the C phase to the C* phase (path P2). Since the third bogolon state has the lowest non-zero energy in the C* phase, we focus on the third bogolon state. In Fig. 4.3.10(a), we show the real-space amplitudes ϕ and ψ of the third bogolon state [see Eq. (3.1.3)]. They are delocalized into the bulk of the system, whereas the zero-energy modes are localized only at the ends. Also, there are characteristic structure in the amplitudes; the amplitudes ϕ and ψ are finite every four sites. As we have seen before, the spatial pattern of the Majorana correlation [Figs. 2.3.3(a), (b), and (c)] determines the topological properties in the ground states. Therefore it would be important to know how the excitation affects the spatial pattern. (See Sec. 4.3.6 for the relationship between the Majorana correlation and the entanglement spectrum.)

To quantify the Majorana correlation, we first introduce the correlation function between the i-th and the j-th Majorana fermions in the vacuum by

$$\mathrm{i}\,\langle \bar{c}_i \bar{c}_j \rangle. \tag{4.3.12}$$

For example, the cluster interaction $\sigma_i^x\sigma_{i+1}^z\sigma_{i+2}^x \sim \bar{c}_{2i}\bar{c}_{2i+3}$ contributes to the correlation between the $2i$-th and $(2i+3)$-th Majorana fermions. In other words, in the cluster phase, $\mathrm{i}\,\langle \bar{c}_{2i}\bar{c}_{2i+3}\rangle$ is finite. In the analysis of the excited states, we calculate the Majorana correlations (4.3.12) in the excited states $|\alpha\rangle$, that is, $\mathrm{i}\,\langle \eta_\alpha \bar{c}_{2i}\bar{c}_{2i+3}\eta_\alpha^\dagger\rangle$. Since we here consider only the third bogolon state, we set $\alpha=3$. In Figs. 4.3.10(b), (c), we show the spatial dependence of the correlation between the $2i$-th and $(2i+3)$-th Majorana fermions ('XZX

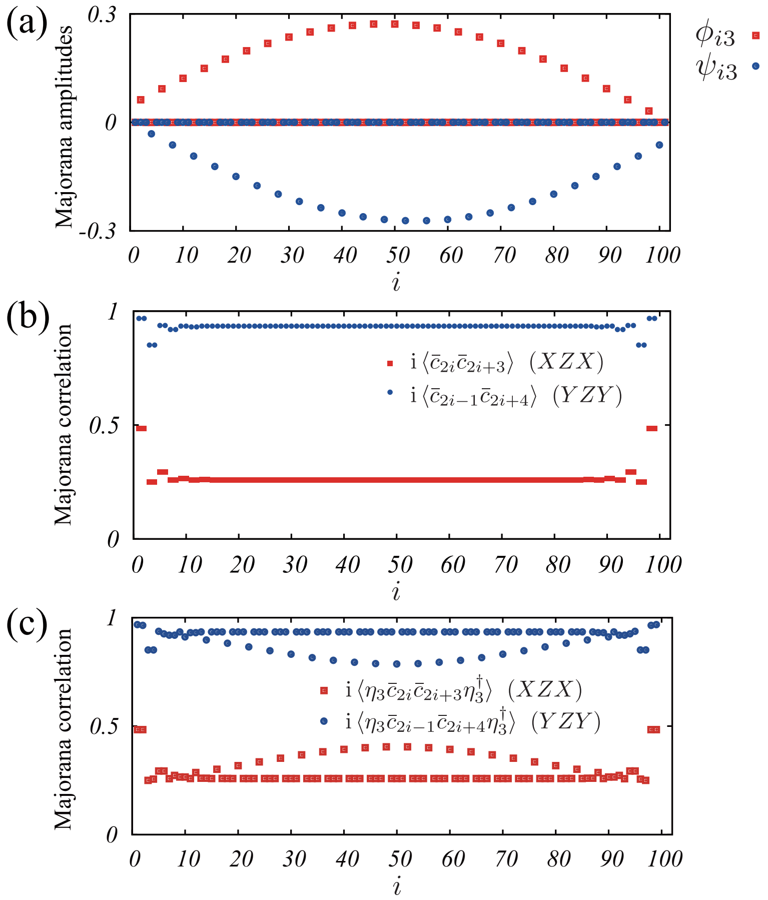

Figure4.3.10 (a) The real-space amplitudes (ϕ, ψ) of the third bogolon with $N = 101$ at $(J^{YY}/J^{XZX}, J^{YZY}/J^{XZX}) = (0, 2)$. (b) The strength of the Majorana correlations in the ground states with $N = 101$ at $(J^{YY}/J^{XZX}, J^{YZY}/J^{XZX}) = (0, 2)$. (c) The strength of the Majorana correlations in the third bogolon state $\eta_3^\dagger|\mathrm{vac}\rangle$ with $N = 101$ at $(J^{YY}/J^{XZX}, J^{YZY}/J^{XZX}) = (0, 2)$. (Figure taken from Ref. [92].)

bond') and that between the $(2i-1)$-th and $(2i+4)$-th Majorana fermions ('YZY bond'). The former (latter) detects the correlation characteristic of the cluster interaction (J^{XZX}) [the dual cluster interaction (J^{YZY})]. The Majorana correlations in the ground states do not depend on the position of the bond except near the ends as is seen in Fig. 4.3.10(b). For the third bogolon state $\eta_3^\dagger|\mathrm{vac}\rangle$, on the other hand, they exhibit peculiar structures as shown in Fig. 4.3.10(c); the Majorana correlations are significantly affected by the bogolon every four bonds, while they are almost intact at the other bonds [see Fig. 4.3.11(a)]. This suggests that we may explain the dynamics of the entanglement spectrum in terms of the Majorana correlations. To substantiate this, we represent the strength of the Majorana correlations by the thickness of the bonds in Fig. 4.3.11(a). For example, when the YZY bond between the $(2i-1)$-th and $(2i+4)$-th Majorana fermions becomes weaker, the XZX bond between the $(2i-4)$-th and $(2i-1)$-th Majorana fermions becomes stronger. However the YZY bonds are always stronger than XZX bonds.

Next we discuss the relationship between the Majorana correlations and the entanglement spectrum calculated for an excited state. Because the entanglement spectrum in the ground state is believed to reflect the emergent degrees of freedom at the boundaries [46], we expect that some information in the *excited states* can be obtained from the entanglement spectrum as well as the entanglement entropy shown in the previous section. As in the previous section, we consider the reduced density matrix for the excited state, where $\rho = |\Psi\rangle\langle\Psi|$ is the density matrix of the third bogolon state $|\Psi\rangle = \eta_3^\dagger|\mathrm{vac}\rangle$. Substituting the eigenvalues of the reduced density matrix ρ, we can obtain the entanglement spectrum for the excited state in question. Here we cut the system as shown in Fig. 4.3.3. We calculated the block-size (L_{sub}) dependence of the entanglement spectrum for the third bogolon state. The lowest four entanglement levels are shown in Fig. 4.3.11(b). We can see that the degeneracy depends on the length of the subsystem and the lower level is almost two or four-fold degenerate.

Let us focus on two specific cases: $L_{\mathrm{sub}} = 45$ and 49. First, when $L_{\mathrm{sub}} = 45$, the boundaries between two subsystems are indicated by the dashed lines in Fig. 4.3.11(a). In this case, we cut four thick YZY (blue) bonds which are not affected at all by the third bogolon, and as a consequence we have four unpaired Majorana fermions at the ends. Because they form two fermionic edge modes as in the case of the ground state, the lowest level of the entanglement spectrum shows four-fold quasi-degeneracy shown in Fig. 4.3.11(b) (the level indicated by the left arrow).

Second, when $L_{\mathrm{sub}} = 49$, the boundaries between two subsystems are shown by the dotted lines in Fig. 4.3.11(a). Now we cut two thick and two thin YZY bonds. In this case, only two unpaired Majorana fermions appear at the cut ends and can contribute to the double degeneracy of the entanglement spectrum in Fig. 4.3.11(b) (see the level shown by the right arrow). The other Majorana fermions from thin YZY bonds are disturbed by the third bogolon and cannot form edge modes which causes the two-fold degeneracy in the entanglement spectrum. Therefore the entanglement spectrum for the excited states reflects the strength of the Majorana correlation when the model is quadratic in the Majorana fermions.

Finally we explain the peculiar time evolution of the entanglement spectrum observed in Sec. 4.3.3 (see Fig. 4.3.6): the oscillating and splitting structures. Here we set $L_{\mathrm{sub}} = 49$ in the calculation. Because the dynamics after passing the critical point is dominated by the third bogolon for slow enough sweeps, we may expect that the dynamical behavior of the entanglement spectrum may be captured essentially by the third bogolon state. As we have seen in Fig. 4.3.11(b), the number of degeneracy of the entanglement spectrum is almost two. This is the origin of the splitting of the entanglement spectrum for the slower sweep. On the other hand, for faster sweeps, the excitations whose energies are higher than that of the

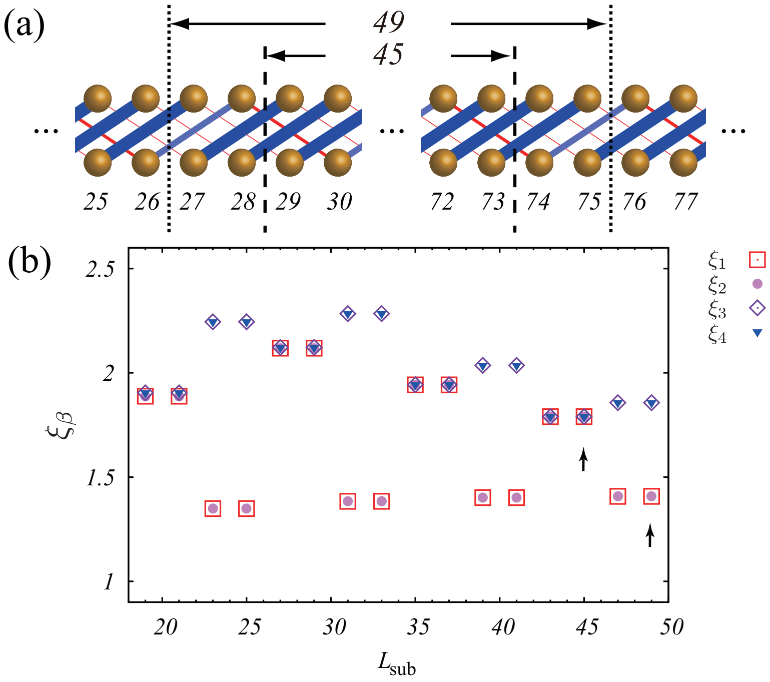

Figure4.3.11 (a) Schematics of the Majorana correlations with $N = 101$. The strength of the Majorana correlations in Fig. 4.3.10(c) is shown by the thickness of the bonds. (b) The entanglement spectrum $\{\xi_\beta(L_\text{sub})\}$ for the third bogolon state at $(J^{YY}/J^{XZX}, J^{YZY}/J^{XZX}) = (0, 2)$ plotted against the size L_sub of the subsystem (see Fig. 4.3.3 for the arrangement of the subsystem). $L_\text{sub} = 45$ and 49 are marked by the arrows. (Figure taken from Ref. [92].)

third bogolon also get involved in the dynamics after passing the critical point. The final state at $t = \tau$ is a superposition of those excited states as shown in Fig. 4.3.8. Because the state is not the eigenstate of the instantaneous Hamiltonian at time $t > \tau/2$, the expectation values of the Majorana correlation in the state oscillate in time. Therefore the entanglement spectrum oscillates in time for a faster sweep. A similar argument applies to the oscillating structure in Fig. 4.3.4.

4.3.6 Dimer model

In Sec. 4.3.5, we investigated the relationship between the Majorana correlation defined by Eq. (4.3.12) and the entanglement spectrum for the excited state. To confirm the relationship between the Majorana correlation and the entanglement spectrum, we calculate the entanglement spectrum of a model whose Majorana correlation is obvious. We consider a model defined by

$$H_\text{D} = \sum_{i=1}^{N-2} \left(-J_i^{XZX} (c_i^\dagger - c_i)(c_{i+2}^\dagger + c_{i+2}) + J_i^{YZY} (c_i^\dagger + c_i)(c_{i+2}^\dagger - c_{i+2}) \right), \tag{4.3.13}$$

where

$$J_i^{XZX} = \begin{cases} 0 & \text{if } i \neq 0 \,(\mathrm{mod} 4) \\ 2 & \text{if } i = 0 \,(\mathrm{mod} 4) \end{cases} \quad J_i^{YZY} = \begin{cases} 1 & \text{if } i \neq 2 \,(\mathrm{mod} 4) \\ 0 & \text{if } i = 2 \,(\mathrm{mod} 4) \end{cases} . \tag{4.3.14}$$

Although degenerate ground states exist as well as the generalized Kitaev model we considered, we here focus on the Bogoliubov vacuum state. In Fig. 4.3.12(a), we show the Majorana correlations between the $2i$-th and $(2i+3)$-th Majorana fermions (XZX) and the $(2i-1)$-th and $(2i+4)$-th Majorana fermions (YZY). The Majorana correlation in the vacuum state is depicted in Fig. 4.3.12(b). Here a Majorana fermion interacts with at most one Majorana fermion. The block-size dependence of the entanglement spectrum in the vacuum state is shown in Fig. 4.3.12(c). When $L_{\mathrm{sub}} = 45$, for example, the boundaries between two subsystems are indicated by the dashed lines in Fig. 4.3.12(b). We cut four YZY bonds and two XZX bonds. Therefore six unpaired Majorana fermions exist at the cut ends. Because they form three fermionic edge modes, the lowest level of the entanglement spectrum shows the eight-fold degeneracy in Fig. 4.3.12(c). On the other hand, when $L_{\mathrm{sub}} = 49$, the boundaries between two subsystems are indicated by the dotted lines in Fig. 4.3.12(b). We cut two YZY bonds (see Fig. 4.3.12(c)). In this case, we have two unpaired Majorana fermions at the cut ends, which contribute to the two-fold degeneracy of the entanglement spectrum in Fig. 4.3.12(c). We thus see that the number of unpaired Majorana fermions at the cut ends in the dimer model (4.3.13) is reflected in the degeneracy structure of the entanglement spectrum, as in the case of the Su–Schrieffer–Heeger model [153].

4.4 Summary of this chapter

We have studied the ground-state phase diagram and dynamics of the generalized Kitaev model in one dimension with several competing interactions (4.1.1). First, we have determined boundaries among several quantum phases of the model by the energy gap and identified the universality classes of the critical points using several CFT techniques. The phases are characterized by the winding number, string correlation functions, and the entanglement spectrum. A lot of phases appear as a result of the competition among several Majorana interactions.

Second, we have investigated dynamical properties during two types of interaction sweep through the critical points which separate two topological phases: the C phase to the $\mathrm{AF}^{(y)}$ phase and the C phase to the C* phase. After slow sweeps across the critical points, spatially periodic structures have been observed both in the string correlation functions and in the entanglement entropy and oscillating and splitting structures have been observed in the entanglement spectrum. This implies that even for slow enough sweeps, the ground state of

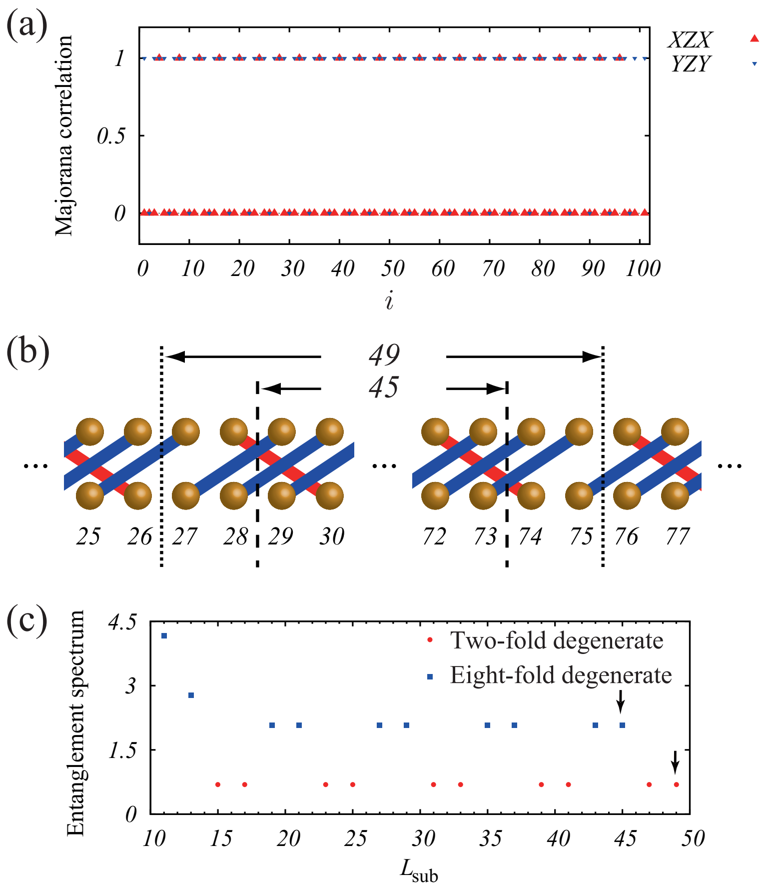

Figure4.3.12 (a) The strength of the Majorana correlations for the ground state of the model (4.3.13) with $N = 101$. (b) The picture of the Majorana correlations with $N = 101$. The strength of the Majorana correlations in Fig. 4.3.12(a) is shown by the bonds. (c) The block-size dependence of the entanglement spectrum $\xi_\beta(L_{\mathrm{sub}})$ for the vacuum with $N = 101$. (Figure taken from Ref. [92].)

one phase evolves into the final state which is no longer the ground state of the instantaneous Hamiltonian of final time. This breakdown of adiabaticity is due to the fact that the degenerate ground states are labeled by the eigenvalues of the fermionic parity operators which determine the topological properties of the system. Unlike the usual sweep dynamics across critical points [144, 154–156], the dynamical behavior observed here is not characterized by the critical exponents but the fermion-number parity of the initial state. Finally, we have reproduced the similar structures by using the low-lying excited states and verified that the structures come from a single bogolon excited near the critical points. In addition, we have found that the entanglement spectrum reflects the strength of the Majorana correlations for the excited states a well as for the ground states.

Chapter5

Topological properties of the Kitaev model with spatially periodic modulation

In this chapter, we study the quantum phase transitions in the one-dimensional Kitaev model with spatially periodic modulation. In Sec. 5.1, we define our model and give its Majorana representation. We introduce the string correlation functions and the entanglement spectrum to characterize the topological phases. In Sec. 5.2, we study the quantum phase transitions of the model with the open boundary condition as we change the amplitude, the wave number, and the phase of the periodic modulation. We characterize each phase by the string correlation functions and the entanglement spectrum. Focusing on the topological phases, we discuss the topological phase transitions and the stability of the Majorana edge modes. In Sec. 5.3, we characterize each phase by the topological invariant under the periodic boundary condition. We confirm that the bulk-edge correspondence holds for non-uniform system. In Sec. 5.4, we summarize our results and conclude this chapter.

5.1 Model

In this chapter, we consider a generalized Kitaev model in one dimension with spatially periodic modulation (Fig. 5.1.1):

$$H = \sum_{i=1}^{N} \left(t c_i^\dagger c_{i+2} + t c_i^\dagger c_{i+2}^\dagger + \text{h.c.} - 2h \cos(Qi + \delta) c_i^\dagger c_i \right), \tag{5.1.1}$$

where N and t respectively are the system size and the hopping (or superconducting pairing) amplitude. The periodic modulation of the chemical potential is controlled by the amplitude h, the wave number Q, and the phase δ. Throughout this chapter, we set the lattice constant equal to 1 and we only consider the cases when $Q/2\pi$ takes rational numbers. The above

Hamiltonian may be written in the matrix form as

$$H=\sum_{i,j=1}^{N}\left[c_i^{\dagger}A_{ij}c_j+\frac{1}{2}\left(c_i^{\dagger}B_{ij}c_j^{\dagger}+c_iB_{ji}c_j\right)\right], \tag{5.1.2}$$

where A and B respectively are real symmetric and real antisymmetric matrices with $A_{i,i}=-2h\cos(Qi+\delta)$, $A_{i,i+2}=A_{i+2,i}=t$, $B_{i,i+2}=-B_{i+2,i}=t$, and 0 otherwise. Note that a similar Hamiltonian with nearest-neighbor interaction has been studied in Ref. [66]. The next-nearest-neighbor part of the Hamiltonian [Eq. (5.1.1)] (i.e., H with $h=0$) is transformed by the Jordan–Wigner transformation [121]

$$c_i=\prod_{j=1}^{i-1}(-\sigma_j^z)\,\sigma_i^-,\quad c_i^{\dagger}=\prod_{j=1}^{i-1}(-\sigma_j^z)\,\sigma_i^+ \tag{5.1.3}$$

into the cluster model [131,132,134]

$$H_{\mathrm{C}}=-\sum_{i=1}^{N}t\sigma_i^x\sigma_{i+1}^z\sigma_{i+2}^x, \tag{5.1.4}$$

where σ_i^{α} $(\alpha=x,y,z)$ are the Pauli matrices at site i. For the open boundary condition, we take $\sigma_{N+1}^{\alpha}=\sigma_{N+2}^{\alpha}=0$ $(\alpha=x,y,z)$. The three-spin interaction in Eq. (5.1.4) and the ground state of the Hamiltonian H_{C} are respectively called the cluster interaction (or the cluster stabilizer) and the cluster state in quantum-information science [135–137]. On the other hand, the chemical potential is transformed into an magnetic field in the spin language. Thus the modulating chemical potential corresponds to inhomogeneous magnetic field

$$H_{\text{field}}=-\sum_{i=1}^{N}h\cos(Qi+\delta)\sigma_i^z. \tag{5.1.5}$$

This magnetic field forces the spins polarized along the z-direction and locally changes the topological properties of the cluster phase. The wave number Q determines the distance between the nodes where the magnetic field scarcely affects the topological properties. The phase δ shifts the position of the nodes.

The topological properties of the ground state of the model defined by Eq. (5.1.2) become clear in the Majorana representation [20]. The Majorana fermions $\{\bar{c}_i\}$ consist of the real and imaginary parts of the spinless fermions $\{c_i\}$ at each site:

$$\bar{c}_{2i-1}=c_i^{\dagger}+c_i,\quad \bar{c}_{2i}=\mathrm{i}\,(c_i-c_i^{\dagger}),\quad i=1,2,\ldots,N. \tag{5.1.6}$$

The standard anticommutation relations of the spinless fermions $\{c_i\}$, $\{c_i^{\dagger}\}$ translate into

$$\bar{c}_i=\bar{c}_i^{\dagger},\quad \{\bar{c}_i,\ \bar{c}_j\}=2\delta_{ij}. \tag{5.1.7}$$

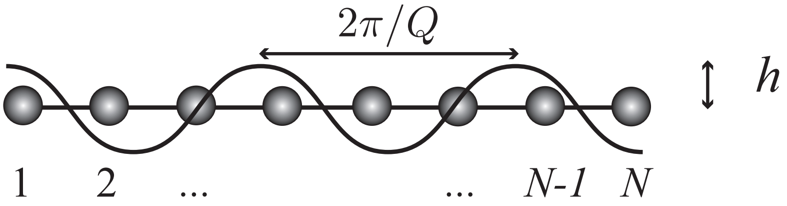

Figure5.1.1 One-dimensional chain [Eq. (5.1.2)] of N sites with spatially periodic modulation whose amplitude, the wave number, and the phase are h, Q, and δ respectively. The black circles mean the sites where the fermions are defined. (Figure taken from Ref. [93].)

Let us introduce a vector $\bar{c} = (\bar{c}_1, \bar{c}_2, \dots, \bar{c}_{2N})^{\mathrm{T}}$ and a real skew-symmetric matrix M with the matrix elements $M_{2i-1,2i} = -M_{2i,2i-1} = h\cos(Qi+\delta), M_{2i,2i+3} = -M_{2i+3,2i} = t$, and 0 otherwise. Then, in terms of the Majorana fermions, the model (5.1.2) is written compactly as

$$H = \frac{\mathrm{i}}{2}\bar{c}^{\mathrm{T}} M \bar{c}. \tag{5.1.8}$$

Since time-reversal operation (complex conjugation) acts on the Majorana fermions as

$$\bar{c}_{2i-1} \to \bar{c}_{2i-1}, \quad \bar{c}_{2i} \to -\bar{c}_{2i}, \tag{5.1.9}$$

we can readily verify that the fermion Hamiltonian H [Eq. (5.1.1) or (5.1.8)] is time-reversal invariant and belongs to BDI class supporting an integer number of Majorana edge modes. For the open boundary condition, we can easily find the Majorana zero modes and degree of degeneracy in the ground states [20, 103]. When the hopping amplitude t is dominant, there are two unpaired Majorana fermions at each end of the system, as shown in Fig. 5.1.2 (a). They non-locally form two zero-energy excitations localized at each end of the system and consequently the four-fold degeneracy in the ground states results. Note that because of the time-reversal symmetry, a pairing of two Majorana fermions at one end of the system is forbidden. On the other hand, when the amplitude h of the modulation is dominant at each site, the Majorana fermions $(\bar{c}_{2i-1}, \bar{c}_{2i})$ pair up locally and form a fermion excitation with finite energy; in general, there are no unpaired Majorana fermions in the system [Fig. 5.1.2 (b)] and the ground state is unique without zero-energy modes.

The topological phases are characterized by string correlation functions. In our case, they detect the pattern of the Majorana correlations [91, 92]. Here we show how to calculate the

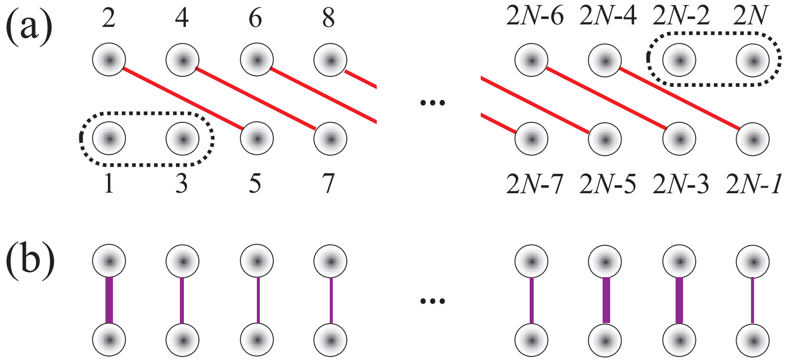

Figure5.1.2 (a), (b) Schematic representation of the interactions in Eq. (5.1.2) by the pairing of the Majorana fermions. Fermion on each site is decomposed into two Majorana fermions (white circles). (a) depicts the next-nearest-neighbor interaction. The Majorana fermions enclosed by dotted circles are not contained in the Hamiltonian. Thus forming the gapless edge modes. (b) represents the modulating chemical potential (or the magnetic field). The strength is shown by the thickness of the bond. (Figure taken from Ref. [93].)

string correlation function $O_{\mathrm{XZX}}(L)$ of distance L [134]:

$$O_{\mathrm{XZX}}(L) =(-1)^L \left\langle \sigma_1^x \sigma_2^y \left(\prod_{i=3}^{L-2} \sigma_i^z \right) \sigma_{L-1}^y \sigma_L^x \right\rangle \tag{5.1.10}$$

$$\sim \left\langle \prod_{j=1}^{L-2} \bar{c}_{2j} \bar{c}_{2j+3} \right\rangle . \tag{5.1.11}$$

In the ground state of the model H_{C} (5.1.4), $\langle \bar{c}_{2j} \bar{c}_{2j+3} \rangle$ is finite and so is the string correlation functions for long-distance limit. We define the string order parameter as

$$O_{\mathrm{XZX}} = \lim_{L\to\infty} O_{\mathrm{XZX}}(L). \tag{5.1.12}$$

In the following, we take the expectation values with respect to the Bogoliubov vacuum $|\mathrm{vac}\rangle$. A phase characterized by the non-vanishing string order parameter O_{XZX} is generally called the cluster phase. Note that the ferromagnetic phase of the Ising Hamiltonian

$$H_{\mathrm{Ising}} = - \sum_{i=1}^{N} \sigma_i^x \sigma_{i+1}^x \tag{5.1.13}$$

corresponds to the topological phase in the fermion representation by the Jordan–Wigner transformation; the ground state has a pair of Majorana fermions at the ends of the system [20]. The usual spin-spin correlation function which converges to a finite value in the long-

Table5.1.1 The relation between the fermion and spin representations. We show the number of the Majorana zero modes, degree of degeneracy in the lowest entanglement level, and the winding number W in each phase. The entanglement spectrum and the winding number are calculated in Sec. 5.2 and Sec. 5.3, respectively. (Table taken from Ref. [93].)

	cluster	ferromagnetic	paramagnetic
spin	$\langle O_{\mathrm{XZX}}\rangle \neq 0$	$\langle O_{\mathrm{XX}}\rangle \neq 0$	disordered
fermion	topological (see Fig. 5.1.2 (a))	topological	trivial
Majorana zero modes	2	1	0
degeneracy in entanglement spectrum	four-fold	two-fold	not degenerate
winding number W	2	1	0

distance limit is transformed into the following fermionic correlation function:

$$O_{\mathrm{XX}}(L) = \langle \sigma_1^x \sigma_L^x \rangle \tag{5.1.14}$$

$$\sim \left\langle \prod_{j=1}^{L-1} \bar{c}_{2j}\bar{c}_{2j+1} \right\rangle . \tag{5.1.15}$$

Since $O_{\mathrm{XX}}(L)$ has a non-local form in the fermion language, we also call it the string correlation function in the following. We summarize the relationship between the fermion and spin representations in Table 5.1.1.

5.2 Quantum phase transitions

We study the quantum phase transitions of the model (5.1.2) when we vary (i) the amplitude h, (ii) the wave number Q, and (iii) the phase δ of the modulation $-2h\cos(Qi+\delta)$. Depending on the phase δ, the nodes of the modulation exist on or between sites. Near the nodes, the topological properties of the sites are slightly affected. The number of nodes is determined by the wave number Q. In fact, because of the cluster interaction in Eq. (5.1.4), the Majorana fermions on the next-nearest-neighbor sites are interacting, which is attributed to the wave length of the Majorana fermions encoded in the real-space wave functions ϕ and ψ (the coefficient of the Bogoliubov transformation). Therefore it would be important to consider the two cases when the nodes are separated by even or odd times the lattice constant. In the following, we take $Q = \pi/2$ or $\pi/3$. In principle, we could consider the nearest neighbor interaction in addition to the next-nearest neighbor interaction. However, to understand the essence of the physical picture, we only consider the next-nearest neighbor interaction. Note that the system with uniform field ($Q = \delta = 0$) undergoes the quantum phase transition to the quantum-paramagnetic phase [132] at $h = 1$.

5.2.1 Transitions with varying the phase δ

We first study the quantum phase transitions when we vary the position of the nodes of the modulation by varying the phase δ of the modulation. We determine the critical points where the energy gap closes which are marked by the dotted lines in Figs. 5.2.2 and 5.2.3. We show the excitation energy between the vacuum and the three lowest-lying excited states $E_1 = \epsilon_1$, $E_2 = \epsilon_2$, $E_3 = \min\{\epsilon_3, \epsilon_1 + \epsilon_2\}$ for $(h, Q) = (2, \pi/2)$ and $(2, \pi/3)$ in Figs. 5.2.2 (a) and 5.2.3 (a), respectively. To characterize the phases from topological point of view, we calculate the entanglement spectrum, which are plotted against the phase δ for $(h, Q) = (2, \pi/2)$ and $(2, \pi/3)$ in Figs. 5.2.2 (b) and 5.2.3 (b), respectively. In the calculation, we divide the entire system into a subsystems A with length L centered in the whole system and the rest B (Fig. 5.2.1). The numbers in the circles in Figs. 5.2.2 (a) and 5.2.3 (a) [Figs. 5.2.2 (b) and 5.2.3 (b)] represent the degree of the degeneracy of the lowest energy level (entanglement level). In each phase, the degree of degeneracy of the ground states coincides with that of the lowest level in the entanglement spectrum. The Majorana fermions localized at the ends non-locally form fermion excitations with zero energy, which causes the ground-state degeneracy in the topological phases. Therefore we confirm that the entanglement spectrum does reflect the fictitious edge modes at the cut ends even for the non-uniform system. As the phase δ changes, we observe several quantum phase transitions. At the critical points, the energy gap closes and the degeneracy structures disappear in both the energy spectrum and the entanglement spectrum. Because the degeneracy changes discontinuously across the critical points, we can use the degree of degeneracy to characterize the phases and locate their boundaries.

To determine the phases, we calculate the string correlation functions. In the calculation, the locations of the two end points (separated by a distance L) are crucial. We take the two points in a symmetric way (i.e., $i = \frac{N-L+2}{2}$ and $i = \frac{N+L}{2}$) with respect to the center of the system as shown in Fig. 5.2.1. Now the system consists of $N = 201$ sites obeying the open boundary condition. The N sites of the system are labeled as in Fig. 5.1.1. In Figs. 5.2.2 (c) and 5.2.3 (c), we show the string correlation functions $O_{\mathrm{XZX}}(L)$ and $O_{\mathrm{XX}}(L)$ for $(h, Q) = (2, \pi/2)$ and $(2, \pi/3)$, respectively. The $O_{\mathrm{XZX}}(L)$ in Eq. (5.1.10) is plotted for $L = 99$. We found that $O_{\mathrm{XX}}(L)$ strongly depends on the distance L and we show both $O_{\mathrm{XX}}(L = 99)$ between even sites (dubbed $O_{\mathrm{XX,even}}$) and $O_{\mathrm{XX}}(L = 101)$ between odd sites ($O_{\mathrm{XX,odd}}$) in the same plots. As we can see from Figs. 5.2.2 (c) and 5.2.3 (c), the string correlation functions have finite values in the phases with ground-state degeneracy: $O_{\mathrm{XZX}} \neq 0, O_{\mathrm{XX}} = 0$ ($O_{\mathrm{XZX}} = 0, O_{\mathrm{XX}} \neq 0$) when the ground states are four-fold (two-fold) degenerate. On the

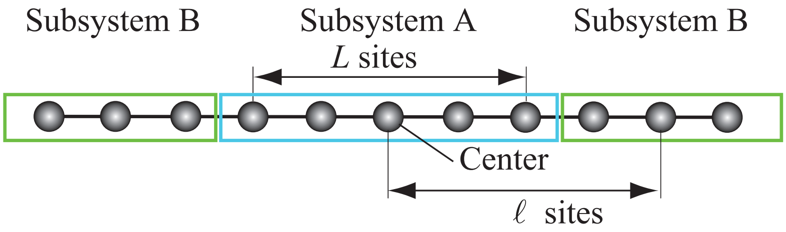

Figure5.2.1 We measure the length L symmetrically around the center of the system and the length ℓ from the center to calculate the physical quantities. We calculate the string correlation functions of length L or ℓ and take L adjacent sites as the subsystem to calculate the ES. (Figure taken from Ref. [93].)

other hand, we can find a phase where both O_{XZX} and O_{XX} vanish. This phase is the paramagnetic phase because it is adiabatically connected to the disordered (i.e., σ^z-ordered) phase of the transverse-field Ising model without gap closing. Thus we may identify the phases whose degree of the ground-state degeneracy are 4, 2, and 1 with the cluster phase, the ferromagnetic phase, and the paramagnetic phase, respectively. In Sec. 5.2.2, we will explain why these topological phases in Figs. 5.2.2 and 5.2.3 appear.

5.2.2 Transitions with varying the amplitude h

In this subsection, we study the quantum phase transitions and the stability of the Majorana edge modes by focusing on the change in the degeneracy of the entanglement spectrum when we vary the amplitude h of the modulation. For the wave number $Q = \frac{\pi}{2}$ and the phase $\delta = 0$, we plot the entanglement levels $\xi_1, \ldots, \xi_4$ against the amplitude h in Fig. 5.2.4 (a). As the amplitude h increases from 0 to 5, the lowest level with four-fold degeneracy splits at $h = 1$ into a pair of levels with two-fold degeneracy. This signals the topological phase transition from the cluster phase to the ferromagnetic phase. We give the detailed explanation in the following. With the wave number $Q = \frac{\pi}{2}$ and the phase $\delta = 0$, the local magnetic field has the form $h \cos(\frac{\pi i}{2})$ and takes the value $\pm h$ (0) at even (odd) sites. When the amplitude h is smaller than 1, the perturbation is not strong enough to close the energy gap and slightly modifies the wave functions of the Majorana zero modes. In fact, we can see in Fig. 5.2.4 (a) the four-fold degeneracy in the entanglement spectrum for $h < 1$, which implies localized edge modes. Thus the entire system is still in the cluster phase as is illustrated in Fig 5.2.4 (b).

On the other hand, this is not the case when the amplitude h is larger than 1. It is helpful to consider the case of strong field $h \gg 1$. Then, the magnetic field on even sites is strong enough to destroy the ordered state, while the fermions on the odd sites do not feel the magnetic field at all. In this case, the lowest level of the entanglement spectrum is two-fold

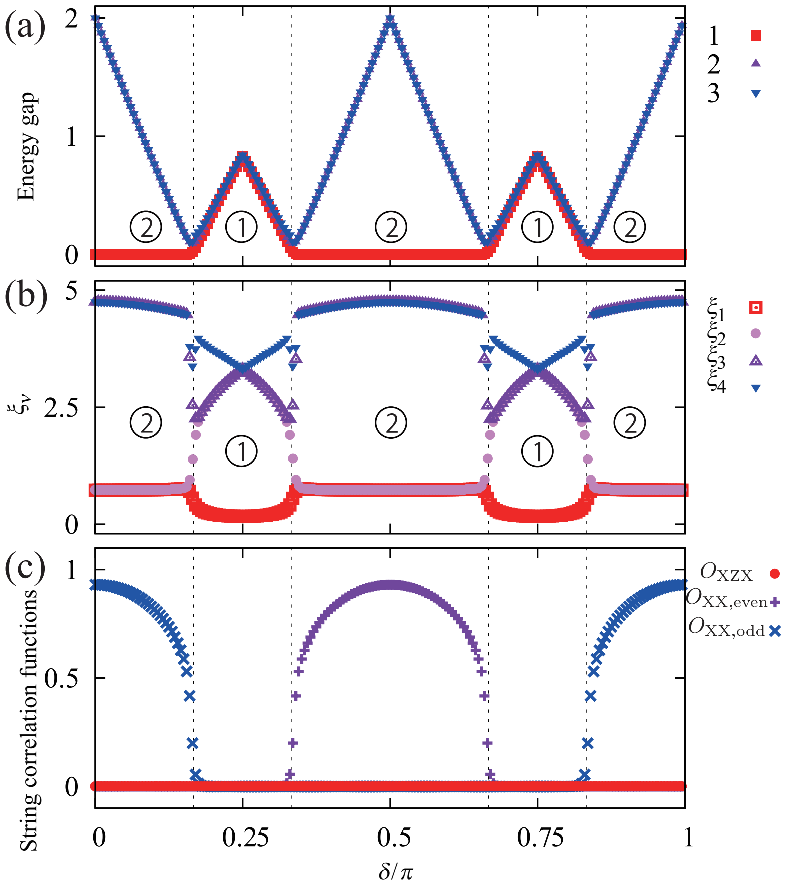

Figure5.2.2 (a) The low-lying energy spectrum E_n $(n = 1, 2, 3)$ with $N = 201$ for $h = 2$, $Q = \frac{\pi}{2}$. The energy gap closes at $\delta = \frac{\pi}{6}, \frac{\pi}{3}, \frac{2\pi}{3}, \frac{5\pi}{6}$. (b) The entanglement spectrum with $N = 201$ and $L = 99$ for (c) $h = 2$, $Q = \frac{\pi}{2}$. (c) The string correlation functions with $N = 201$ for $h = 2$, $Q = \frac{\pi}{2}$. The numbers in circles mean the degeneracy in the lowest energy/entanglement level. The degeneracies in the lowest level are 2 and 1 (no degeneracy) in the topological (ferromagnetic) and trivial (paramagnetic) phases, respectively. (Figure taken from Ref. [93].)

degenerate and the $O_{\mathrm{XX,odd}}$ is finite, while $O_{\mathrm{XX,even}}$ vanishes. This indicates that the entire system is decomposed into the trivial part (even sites) and the topological part (odd sites). The fermions in each part are coupled to each other by the cluster interaction [Eq. (5.1.4)] as is shown in Fig. 5.2.4 (c). To confirm this, we calculated the length ℓ dependence of the string correlation function $O_{\mathrm{XX}}(\ell)$ between $(\frac{N+1}{2})$-th site (the center) and $(\frac{N-1}{2}+\ell)$-th site at $h = 2$ [see Fig. 5.2.4 (d)]. When ℓ is odd, O_{XX} has a finite value. On the other hand, it is 0 when ℓ is even. As the center site belongs to the odd sites, this implies that the state on the even sites has topologically different properties from that of the odd sites. The spins on the even sites are fully polarized along the magnetic field whose direction depends on the sign of the magnetic field. By replacing σ^z_{2i} with its expectation value $(-1)^i$, the cluster interaction $\sigma^x_{2i-1}\sigma^z_{2i}\sigma^x_{2i+1}$ reduces to an alternating interaction $(-1)^i\sigma^x_{2i-1}\sigma^x_{2i+1}$ between next-nearest-neighbor spins. Because it alternates between a ferromagnetic interaction and antiferromagnetic one, the

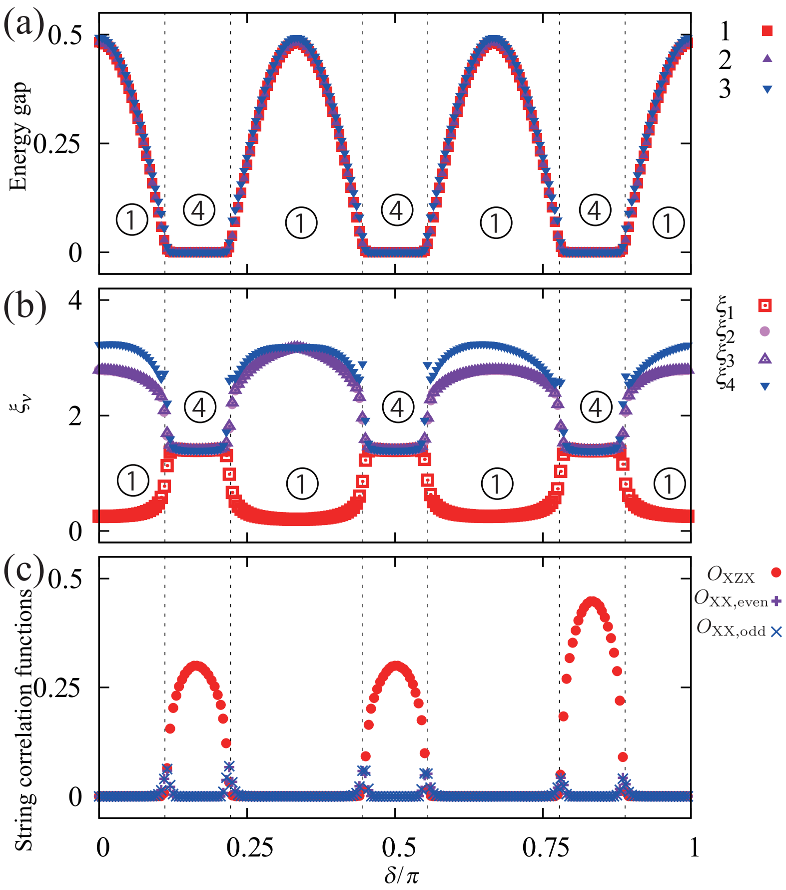

Figure5.2.3 (a) The low-lying energy spectrum E_n ($n = 1, 2, 3$) with $N = 201$ for $h = 2$, $Q = \frac{\pi}{3}$. The energy gap closes at $\delta = \frac{\pi}{9}, \frac{2\pi}{9}, \frac{4\pi}{9}, \frac{5\pi}{9}, \frac{7\pi}{9}, \frac{8\pi}{9}$. (b) The entanglement spectrum with $N = 201$ and $L = 99$ for $h = 2$, $Q = \frac{\pi}{3}$. (c) The string correlation functions with $N = 201$ for $h = 2$, $Q = \frac{\pi}{3}$. The numbers in circles mean the degeneracy in the lowest level. The degeneracies in the lowest level are 4 and 1 (no degeneracy) in the cluster and paramagnetic phases respectively. (Figure taken from Ref. [93].)

spins on odd sites align as $\cdots \rightarrow\rightarrow\leftarrow\leftarrow\rightarrow\rightarrow\leftarrow\leftarrow \cdots$, where $|\rightarrow\rangle$ ($|\leftarrow\rangle$) is the eigenstate of the Pauli matrix σ^x with eigenvalue 1 (-1). Those on the even sites, on the other hand, are polarized in the z-direction. We can see this in the oscillation of the string correlation function in Fig. 5.2.4 (d). Therefore we conclude that the entire system is decoupled into the spins on odd sites that interact with each other via the alternating interactions and the remaining part polarized along the magnetic field as shown in Fig. 5.2.4 (c).

Next we turn our attention to the Majorana edge modes. The amplitudes ϕ_ν and ψ_ν of the ν-th ($\nu = 1, 2$) Majorana fermion are shown in Figs. 5.2.5 (a) and (b). The parameter in Fig. 5.2.5 (a) is $h = 0$ for which the ground state shows the cluster phase. The ground states are four-fold degenerate because of the two zero modes. Note that each zero mode consists of a pair of the Majorana fermions at the ends of the system. In the absence of the periodic modulation ($h = 0$), we confirm that the Majorana fermions are localized at the

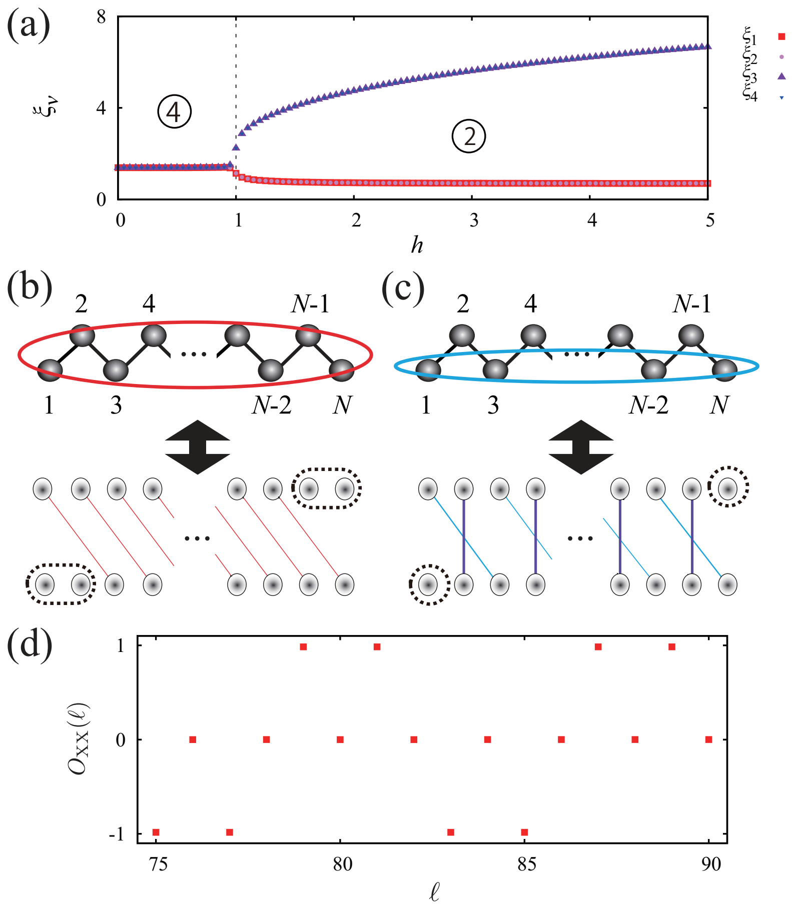

Figure5.2.4 (a) The entanglement spectrum with $N = 201$ and $L = 99$ for $Q = \frac{\pi}{2}$ and $\delta = 0$. There is a quantum phase transition between the cluster phase to the ferromagnetic phase at $h = 1$. The numbers in circles represent the degeneracy in the lowest level. (b), (c) Schematic representation of the system. The Majorana fermions on the sites enclosed by the ellipses in the upper panels are paired with the next nearest ones as shown in the lower panels. (b) When the amplitude h is smaller than 1, the entire system enclosed by red ellipse is still in cluster phase. (c) When the amplitude h is larger than 1, the entire system is decomposed into paramagnetic part (even sites) and ferromagnetic part (odd sites) enclosed by blue ellipse coupled by the cluster interaction in Eq. (5.1.4). (d) The length dependence of the string correlation function $O_{\rm XX}$ for $N = 201$, $h = 4$, $Q = \frac{\pi}{2}$, and $\delta = 0$. The value is finite (0) when length L is odd (even). (Figure taken from Ref. [93].)

ends [Fig. 5.2.5 (a)].

On the other hand, the situation is quite different when $h = 3$, $Q = \frac{\pi}{2}$, and $\delta = 0$ as shown in Fig. 5.2.5 (b). As in the previous case, the lowest two modes are localized at the ends, although the ground states and the entanglement spectrum are two-fold degenerate. Because of the spatial periodicity of the modulation in our case, the field at even sites is strong enough to make the Majorana fermions at even sites paired up locally, while those at odd sites remain intact. Therefore only one of the two zero modes is unaffected by the modulation [see Fig 5.2.4 (c)], which is responsible for the two-fold degeneracy in the entanglement spectrum. The other excitation acquires a finite energy by pairing up locally. This is why the ferromagnetic phase

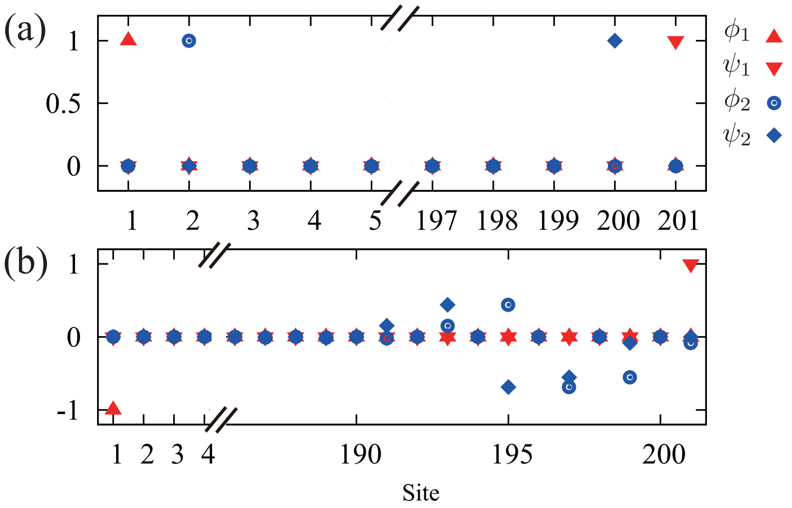

Figure5.2.5 (a) The amplitudes of the Majorana fermions. $N = 201$, $h = 0$. (b) The amplitudes of the Majorana fermions. $N = 201$, $h = 3$, $Q = \frac{\pi}{2}$, and $\delta = 0$. (Figure taken from Ref. [93].)

survives and the cluster phase does not appear for strong magnetic field ($h \gg 1$) in Fig. 5.2.2.

Finally we study the stability of the cluster phase against the amplitude h of the modulation. In Fig. 5.2.6 (a), we show the plot of the entanglement spectrum against the amplitude h for the wave number $Q = \frac{\pi}{3}$ and the phase $\delta = 0$. The cluster phase remains stable when $h < \sqrt[3]{4}$. The ground state is in the paramagnetic phase for larger h. In Fig. 5.2.6 (b), the amplitudes of the Majorana fermions of the lowest energy are shown for the same (Q, δ) and $h = 3$ in the paramagnetic phase. They now spread into the bulk.

For the wave number $Q = \frac{\pi}{3}$ and the phase $\delta = \frac{\pi}{2}$, we show the entanglement spectrum against the amplitude h in Fig. 5.2.6 (c). The four-fold degeneracy in the entanglement spectrum does *not* depend on the amplitude h, which suggests that the Majorana zero modes are stable even for large h. We can explain this as follows. Because of the nodes of the magnetic field on the sites, there are fermions on every three sites which do not feel the magnetic field. The Majorana fermions can be localized at these sites and form zero-energy modes as shown in Fig. 5.2.6 (d). This is why the Majorana zero modes are stable even for strong enough magnetic field. A similar argument can be applied to the existence of the cluster phase in Fig. 5.2.3.

5.3 Topological invariant

In the previous section, we studied the topological phases in terms of the edge modes, the entanglement spectrum, and the string correlation functions. In this section, we characterize these phases by studying the bulk system without boundary. Specifically, we calculate a

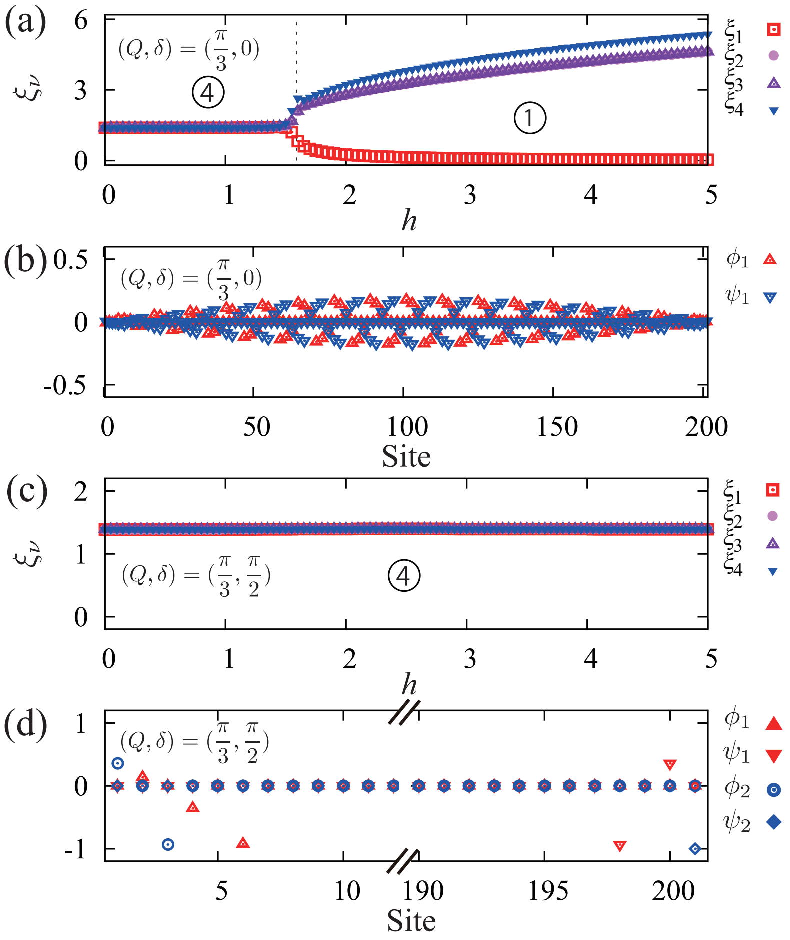

Figure5.2.6 (a) The entanglement spectrum with $N = 201$ and $L = 99$ for $Q = \frac{\pi}{3}$ and $\delta = 0$. The numbers in circles represent the degeneracy in the lowest level. There is a quantum phase transition between the cluster phase to the paramagnetic phase at $h = \sqrt[3]{4}$. (b) The amplitudes of the Majorana fermions. $N = 201$, $h = 3$, $Q = \frac{\pi}{3}$, and $\delta = 0$. (c) The entanglement spectrum with $N = 201$ and $L = 99$ for $Q = \frac{\pi}{3}$ and $\delta = \frac{\pi}{2}$. The cluster phase is stable against the modulation. (d) The amplitudes of the Majorana fermions. $N = 201$, $h = 3$, $Q = \frac{\pi}{3}$, and $\delta = \frac{\pi}{2}$. (Figure taken from Ref. [93].)

topological invariant which is given by an integral over momentum space. To calculate it, we impose the periodic boundary condition on the system. First, we perform the Fourier transformation. Since the $\mathbb{Z}_2$ index proposed in Ref. [20] indicates the parity of the number of edge modes and cannot distinguish the phases with even (odd) numbers of edge modes, we calculate the $\mathbb{Z}$ index [157, 158]. Rewriting the wave number Q of the modulation as $2\pi\frac{p}{q}$ with p, q coprime integers, we decompose the system into supercells with length q and use the Fourier transformation with periodic modulation:

$$c_{s,l} = \sqrt{\frac{q}{N}} \sum_{k=0}^{2\pi/q} c_{s,k} e^{ikql}, \tag{5.3.1}$$

where $l\,(l = 1, 2, \dots, N/q)$ labels the supercells and $s\,(s = 1, 2, \dots, q)$ denotes a site in each supercell [66]. The wave number k is defined in the reduced Brillouin zone $[0, 2\pi/q]$. Next, using these operators, we construct new operators:

$$\gamma_{2s-1}(k) = c_{s,k} + c^\dagger_{s,-k}, \quad \gamma_{2s}(k) = -\mathrm{i}\,(c_{s,k} - c^\dagger_{s,-k}). \tag{5.3.2}$$

For $k = 0, 2\pi/q$, these operators satisfy the anticommutation relation of the Majorana fermions. In this representation, we can rewrite our Hamiltonian in the matrix form:

$$H = \mathrm{i} \sum_{k=0}^{2\pi/q} \sum_{m,n=1}^{2q} B_{m,n}(k)\gamma_m(-k)\gamma_n(k), \tag{5.3.3}$$

$$B = \begin{bmatrix} 0 & -v^\dagger \\ v & 0 \end{bmatrix}. \tag{5.3.4}$$

This matrix B is a $2q \times 2q$ complex skew-symmetric matrix and carries topological information and the submatrix v is a $q \times q$ complex matrix. The matrix elements of the submatrix v are $v_{s,s} = -h\cos(\frac{s}{q} + \delta)$ for $s = 1, 2, \dots, q$, $v_{s,s+2} = -1$ for $s = 1, 2, \dots, q-2$, and $v_{q-1,1} = v_{q,2} = -\exp(ikq)$, and 0 otherwise. With the above setup in hand, we are ready to calculate the topological invariant, called the winding number [157, 158]. We need to know how many times the eigenvalues $\{z_n(k)\}\,(n = 1, \dots, q)$ of the submatrix v wind around the origin of the complex plane as we change the wave number k through the reduced Brillouin zone $[0, 2\pi/q]$, which is given by the following integral

$$W = \sum_{n=1}^{q} \int_0^{2\pi/q} \frac{dk}{2\pi i} \partial_k \ln z_n(k). \tag{5.3.5}$$

We calculated it for the sets of parameters corresponding to the cluster, ferromagnetic, and paramagnetic phases to find that W is equal to 2, 1, and 0, respectively. Therefore, we can see that the correspondence between the winding number with the periodic boundary condition and the number of the Majorana edge modes holds with the open boundary condition even in the presence of the periodic modulation (Table 5.1.1).

5.4 Summary of this chapter

In this chapter, we have studied quantum phase transitions and the stability of the Majorana zero modes of a generalized Kitaev model in one dimension where the chemical potential is modulating in space. First, we have studied quantum phase transitions when we vary the phase of the modulation from the viewpoint of edge physics. We have characterized each phase by the number of the Majorana zero modes, the entanglement spectrum, and the string correlation functions. We have shown that the number of the Majorana zero modes localized at the ends of the system is reflected in the degeneracy of the lowest level of the entanglement spectrum. Second, focusing on the stability of the Majorana zero modes, we have studied quantum phase transitions when we vary the amplitude of the modulation. We have found a quantum phase transition between the topological phases and shown that in certain cases the degeneracy of the entanglement spectrum does not change even when the amplitude of the modulation is sufficiently large. Finally, we have studied the topological properties of the bulk system with an alternative approach with the periodic boundary condition. We have calculated the topological invariant, which corresponds to the number of the zero-energy excitations that exist for the open boundary condition. We thus confirm that the bulk-edge correspondence holds even in the presence of the spatially periodic modulation.

Chapter6

Summary and outlook

In this thesis, we have studied the topological and dynamical properties of the Majorana fermions in one dimension with several competing interactions.

In Chapter 1, we have overviewed the study of the phases of matter and seen how the concept of topology has been introduced to characterize phases called topological phases. We then showed the motivation of this thesis in the recent study of quantum-information science and condensed-matter physics.

In Chapter 2, we have reviewed the topological phases using the spin-1 Heisenberg model and the Kitaev model as the examples. We have seen three ways to characterize the topological phases: entanglement properties, edge modes, and non-local string correlation functions. We also introduced the MPS which efficiently represents the ground states in one dimension.

In Chapter 3, we have explained the numerical methods used in this thesis: the Bogoliubov-transformation method for non-interacting fermions and iTEBD method based on the MPS. We then illustrated how to calculate the entanglement properties and correlation functions.

In Chapter 4, we have studied quantum phase transitions and dynamics in the model with competition among several Majorana interactions. We first identified the universality classes of the critical points using several CFT techniques and then characterized these phases by the order parameters, the winding number, and the entanglement spectrum. Second, with the knowledge of the topological properties of the ground states, we have investigated dynamical properties during two types of interaction sweep through the critical points which separate topological phases: the C phase to the $\mathrm{AF}^{(y)}$ phase and the C phase to the C* phase. After slow sweeps across the critical points, spatially periodic structures have been observed both in the correlation functions and in the entanglement entropy and oscillating and splitting structures have been found in the entanglement spectrum. Finally, we have understood these structures by using the low-lying bogolon states excited near the critical points. In addition, we have found that the entanglement spectrum reflects the strength of the Majorana correlation in the excited states as well as for the ground states.

In Chapter 5, we have studied quantum phase transitions and the stability of the Majorana zero modes of a generalized Kitaev model whose chemical potential (or gate voltage) is spatially modulating. First, we have investigated quantum phase transitions as we vary the phase of the modulation and characterized each phase by the Majorana zero modes, the entanglement spectrum, and the non-local string correlation functions. Second, focusing on the stability of the Majorana zero modes, we have studied quantum phase transitions when we vary the amplitude of the modulation. We have found a quantum phase transition between the topological phases where the number of the Majorana zero modes changes, and shown some cases where the degeneracy of the entanglement spectrum does not change even when the amplitude of the modulation is sufficiently large. Finally, we have studied the topological properties of the bulk system with the periodic boundary condition. We have calculated the topological invariant, which corresponds to the number of the zero-energy excitations that exist for the open boundary condition.

In this thesis, we have only considered the topological phases of a generalized Kitaev model which are quadratic in the fermions and thus exactly solvable by the Bogoliubov transformation. Therefore, it would be interesting how quartic interactions modify the edge modes and the interacting edge modes affect the dynamics. Although the non-local properties have been well studied for the ground states, there are few studies in the dynamics and we know little about the universal properties such as the Kibble–Zurek scaling in the conventional phase transitions. In this thesis, we have studied the sweep dynamics and seen the relationship between the string correlation function and the entanglement structure. Thus it would be necessary to know to what extent this relation holds for other phases such as the Haldane phase. Furthermore, it would be necessary to further study the physical properties of the entanglement spectrum in the excited states by using other models which possess the zero-energy modes in the topological phases.

App. A Haldane phase

In this appendix, we show the topological properties of the Haldane phase of spin-1 Heisenberg antiferromagnet with the open boundary condition [4, 5]:

$$H = \sum_{i=1}^{N-1} \mathbf{S}_i \cdot \mathbf{S}_{i+1}, \tag{A.1}$$

where N denotes the number of sites and $\mathbf{S}_i = (S_i^x, S_i^y, S_i^z,)$ is the spin-1 operator at the i-th site. This model is transformed into a local Hamiltonian

$$\begin{aligned} \tilde{H} &= VHV^{-1} \\ &= \sum_j \left[S_j^x \exp(\mathrm{i}\pi S_{j+1}^x) S_{j+1}^x + S_j^y \exp\left(\mathrm{i}\pi(S_j^z + S_{j+1}^x)\right) S_{j+1}^x + S_j^z \exp(\mathrm{i}\pi S_{j+1}^z) S_{j+1}^z \right] \end{aligned} \tag{A.2}$$

by the non-local unitary transformation [10, 11]

$$V = \prod_{j<k} \exp(\mathrm{i}\pi S_j^z S_k^x). \tag{A.3}$$

The model (A.2) has the global discrete symmetry $\mathbb{Z}_2 \times \mathbb{Z}_2$ (π-rotation about x, y, z axes).

Here we explain the physical properties of the models (A.1) and (A.2). The non-local correlation functions [6, 10] that detect the hidden antiferromagnetic order in the Haldane phase are transformed into the conventional local correlation functions as [10, 11]

$$\langle S_j^x \exp(\mathrm{i}\pi \sum_{l=j+1}^{k} S_l^x) S_k^x \rangle = \langle S_j^x S_k^x \rangle, \tag{A.4}$$

$$\langle S_j^z \exp(\mathrm{i}\pi \sum_{l=j}^{k-1} S_l^z) S_k^z \rangle = \langle S_j^z S_k^z \rangle. \tag{A.5}$$

For the open boundary condition, the zero-energy modes appear at the edges of the system and four-fold degeneracy of the ground states results. These four states correspond to the symmetry-broken states of the transformed Hamiltonian (A.2) with $\mathbb{Z}_2 \times \mathbb{Z}_2$ symmetry [10].

App. B Bogoliubov transformation

The transverse-field Ising model [108, 109] is transformed into a fermion model by the Jordan–Wigner transformation [120]

$$H_{\mathrm{TFIM}} = -\sum_{i=1}^{N}(\sigma_i^x\sigma_{i+1}^x + \lambda\sigma_i^z) \tag{B.1}$$

$$= -\sum_{i=1}^{N}\Big[(c_i^\dagger - c_i)(c_{i+1}^\dagger + c_{i+1}) + \lambda(2c_i^\dagger c_i - 1)\Big] \tag{B.2}$$

$$= -\sum_{i=1}^{N}\left[(c_i^\dagger c_{i+1} + c_{i+1}^\dagger c_i) + (c_i^\dagger c_{i+1}^\dagger + c_{i+1}c_i) + 2\lambda(c_i^\dagger c_i - \frac{1}{2})\right]. \tag{B.3}$$

This is the Kitaev model of spinless p-wave superconductor [20]:

$$H_{\mathrm{Kitaev}} = \sum_{i=1}^{N}\Big[-t(c_i^\dagger c_{i+1} + c_{i+1}^\dagger c_i) - (\Delta c_i^\dagger c_{i+1}^\dagger + \Delta^* c_{i+1}c_i) - \mu c_i^\dagger c_i\Big], \tag{B.4}$$

$$t = \Delta = \Delta^* = 1, \quad \mu = 2\lambda. \tag{B.5}$$

This Hamiltonian commutes with the parity operator

$$P = (-1)^{\sum_{i=1}^{N} c_i^\dagger c_i}. \tag{B.6}$$

From $P^2 = 1$, we get $P = \pm 1$. The even (odd) parity corresponds to the antiperiodic (periodic) boundary condition in the spin representation.

We solve the transverse-field Ising model under the periodic boundary condition. By the Fourier transformation

$$c_j = \frac{1}{\sqrt{2\pi}}\int_{-\pi}^{\pi} dk\, e^{\mathrm{i}kj} c_k, \tag{B.7}$$

the Hamiltonian is written as

$$H_{\mathrm{TFIM}} = 2\int_{-\pi}^{\pi} dk\,(-\cos k - \lambda)c_k^\dagger c_k - 2\mathrm{i}\int_{-\pi}^{\pi} dk\,(\sin k\, c_k c_{-k} - \sin k\, c_{-k}^\dagger c_k^\dagger). \tag{B.8}$$

We then perform the Bogoliubov transformation [121]:

$$\begin{cases} \eta_k = c_k\cos\theta_k - \mathrm{i}\, c_{-k}^\dagger \sin\theta_k, & \text{(B.9a)} \\ \eta_{-k}^\dagger = -\mathrm{i}\, c_k \sin\theta_k + c_{-k}^\dagger\cos\theta_k, & \text{(B.9b)} \end{cases}$$

where η_k and θ_k satisfy the following relation

$$\{\eta_k, \eta_{k'}^\dagger\} = \delta_{kk'}, \quad \tan 2\theta_k = -\frac{\delta_k}{\epsilon_k}. \tag{B.10}$$

With the above transformations, the Hamiltonian is diagonalized and the energy dispersion is given as

$$\epsilon(k) = 2\sqrt{(\cos k + \lambda)^2 + \sin^2 k} \qquad (-\pi < k \leq \pi). \tag{B.11}$$

The ground state $|\Psi_0\rangle$ is the vacuum of the Bogoliubov operators $\{\eta\}$ and has the form of the BCS-type wave function:

$$|\Psi_0\rangle = \prod_{k>0} (\cos\theta_k + \sin\theta_k c_k^\dagger c_{-k}^\dagger)|0\rangle_c, \tag{B.12}$$

where $|0\rangle_c$ is the c-vacuum.

In the following, we show the expression of the Bogoliubov transformation. The Bogoliubov transformation U_{B} in the momentum space is given as

$$U_{\mathrm{B}} = \exp\left[-\mathrm{i}\sum_{k>0} \theta_k (c_{-k}c_k - c_{-k}^\dagger c_k^\dagger)\right]. \tag{B.13}$$

Using the Baker–Campbell–Hausdorff formula

$$e^A B e^{-A} = B + [A, B] + \frac{1}{2!}[A, [A, B]] + \cdots \tag{B.14}$$

and the relation

$$[AB, C] = A\{B, C\} - \{A, C\}B, \tag{B.15}$$

we can confirm that the operator U_{B} is actually the expression of the Bogoliubov transformation:

$$U_{\mathrm{B}}^{-1}\eta_k U_{\mathrm{B}} = c_k. \tag{B.16}$$

The ground state $|\Psi_0\rangle$ is the Bogoliubov vacuum and is written by using the vacuum $|0\rangle_c$ of the c-fermions as

$$|\mathrm{GS}\rangle = U_{\mathrm{B}}|0\rangle_c. \tag{B.17}$$

Next we show the Bogoliubov transformation W_{B} in the real space [121]. To do that, we use the generators $W_\pm$ of the orthogonal matrices ϕ and ψ. The matrices $W_\pm$ are antisymmetric matrices and satisfy

$$\phi = \exp W_+, \quad \psi = \exp W_-. \tag{B.18}$$

Then, the Bogoliubov transformation W_{B} is written as

$$W_{\mathrm{B}} = \exp\left[\frac{1}{2}\sum_{i,j=1}^{N}\left(\frac{W_{+}-W_{-}}{2}\right)_{ij}(c_i c_j + c_i^{\dagger} c_j^{\dagger}) + \sum_{i,j=1}^{N}\left(\frac{W_{+}+W_{-}}{2}\right)_{ij} c_i^{\dagger} c_j\right], \tag{B.19}$$

and we obtain

$$W_{\mathrm{B}}^{-1}\eta_i W_{\mathrm{B}} = c_i. \tag{B.20}$$

The ground state $|\Psi_0\rangle$ is the Bogoliubov vacuum and is written by using the vacuum $|0\rangle_c$ of c-fermions as

$$|\Psi_0\rangle = W_{\mathrm{B}}|0\rangle_c. \tag{B.21}$$

App. C Jordan–Wigner transformation

The one-dimensional spin models are transformed into the fermion models by the Jordan–Wigner transformation [120]. Here we give the examples that can be transformed into the models of non-interacting spinless fermions. By the Jordan–Wigner transformation

$$c_i = \prod_{j=1}^{i-1}(-\sigma_j^z)\sigma_i^-,\ c_i^\dagger = \prod_{j=1}^{i-1}(-\sigma_j^z)\sigma_i^+, \tag{C.1}$$

the relations of the spin-$\frac{1}{2}$'s are transformed into the canonical anticommutation relations of the fermions

$$\{c_i, c_j^\dagger\} = \delta_{i,j}, \quad \{c_i, c_i\} = 0, \quad \{c_i^\dagger, c_i^\dagger\} = 0. \tag{C.2}$$

Here the $\{\sigma_i\}$ are the Pauli matrices at the i-th site and c_i ($c_i^\dagger$) annihilates (creates) the spinless fermion at the i-th site. Because we obtain the following equations by this transformation

$$\sigma_i^z = 2c_i^\dagger c_i - 1, \tag{C.3}$$

$$\sigma_i^x\sigma_{i+1}^x = (c_i^\dagger - c_i)(c_{i+1}^\dagger + c_{i+1}), \tag{C.4}$$

$$\sigma_i^y\sigma_{i+1}^y = -(c_i^\dagger + c_i)(c_{i+1}^\dagger - c_{i+1}), \tag{C.5}$$

$$\sigma_i^x\sigma_{i+1}^z\sigma_{i+2}^x = -(c_i^\dagger - c_i)(c_{i+2}^\dagger + c_{i+2}), \tag{C.6}$$

$$\sigma_i^y\sigma_{i+1}^z\sigma_{i+2}^y = (c_i^\dagger + c_i)(c_{i+2}^\dagger - c_{i+2}), \tag{C.7}$$

the spin models such as the transverse-field Ising model [108, 109]

$$H_{\mathrm{TFIM}} = -\sum_{i=1}^{N}(J\sigma_i^x\sigma_{i+1}^x + h\sigma_i^z), \tag{C.8}$$

the XY model [131]

$$H_{\mathrm{XY}} = \sum_{i=1}^{N}(J^{XX}\sigma_i^x\sigma_{i+1}^x + J^{YY}\sigma_i^y\sigma_{i+1}^y), \tag{C.9}$$

the cluster model [131, 132, 134]

$$H_{\mathrm{C}} = -\sum_{i=1}^{N} J^{XZX}\sigma_i^x\sigma_{i+1}^z\sigma_{i+2}^x, \tag{C.10}$$

and the dual cluster model

$$H_{\mathrm{C}^*} = \sum_{i=1}^{N} J^{YZY} \sigma_i^y \sigma_{i+1}^z \sigma_{i+2}^y \tag{C.11}$$

are quadratic in the spinless fermions. Therefore these spin models are diagonalized by the Bogoliubov transformation [121].

App. D Majorana zero mode

We consider the zero modes of the Kitaev model [20]

$$H = \sum_{i=1}^{N} \left[-(c_i^\dagger c_{i+1} + c_{i+1}^\dagger c_i) - (c_i^\dagger c_{i+1}^\dagger + c_{i+1} c_i) - 2h c_i^\dagger c_i \right]. \tag{D,1}$$

We focus on the amplitudes ϕ and ψ in the Bogoliubov transformation [121]

$$\eta_\mu = \sum_{i=1}^{N} \left(\frac{\phi_{i\mu} + \psi_{i\mu}}{2} c_i + \frac{\phi_{i\mu} - \psi_{i\mu}}{2} c_i^\dagger \right). \tag{D,2}$$

Here, column vectors ϕ_μ and ψ_μ of order N are respectively the μ-th column of the matrices ϕ and ψ and are the solution of the following simultaneous equations (the Heisenberg's equation of motion):

$$\begin{cases} E_\mu \psi_\mu = (A+B)\phi_\mu, & \text{(D,3a)} \\ E_\mu \phi_\mu = (A-B)\psi_\mu, & \text{(D,3b)} \end{cases}$$

where the matrices A and B of order N are given by

$$A = \begin{pmatrix} -2h & -1 & 0 & \dots & 0 \\ -1 & -2h & -1 & \ddots & \vdots \\ 0 & -1 & \ddots & \ddots & \vdots \\ \vdots & \ddots & \ddots & \ddots & -1 \\ 0 & \dots & \dots & -1 & -2h \end{pmatrix}, \quad B = \begin{pmatrix} 0 & -1 & 0 & \dots & 0 \\ 1 & 0 & -1 & \ddots & \vdots \\ 0 & 1 & \ddots & \ddots & \vdots \\ \vdots & \ddots & \ddots & \ddots & -1 \\ 0 & \dots & \dots & 1 & 0 \end{pmatrix}. \tag{D,4}$$

From the canonical commutation relation, we can see that ϕ と ψ are orthogonal:

$$\phi^T \phi = I_N, \quad \psi^T \psi = I_N. \tag{D,5}$$

Next we explicitly construct the zero mode. When $E_m = 0$ for a certain m, two equations in the simultaneous equations (D,3) become independent:

$$\begin{cases} 0 = (A+B)\phi_m, & \text{(D,6a)} \\ 0 = (A-B)\psi_m. & \text{(D,6b)} \end{cases}$$

For $0 \le h < 1$, we can find that

$$\phi_m = (1, -h, (-h)^2, \dots)^T, \quad \psi_m = (\dots, (-h)^2, -h, 1)^T \tag{D,7}$$

are the solution of zero-energy mode, which are exponentially localized near the edges of the system.

App. E Operator content and universality class

In this appendix, based on Ref. [92], we determine the operator content of the conformal field theories describing the critical points in Fig. 4.2.1. To be specific, we take the periodic boundary condition and consider the multicritical point M1: $(J^{YY}/J^{XZX}, J^{YZY}/J^{XZX}) = (-1, 0)$ where the gapless k-linear branches exist at $k = 0, \pm 2\pi/3$. Then, the low-energy physics may be described by the effective Hamiltonian

$$\begin{aligned} &H_{\mathrm{GC}} - E_{\mathrm{ZP}} \\ &\approx \sum_{|k|\le\Lambda} v_{\mathrm{s}} k\, \eta^{\dagger}_{k-\frac{2\pi}{3}} \eta_{k-\frac{2\pi}{3}} + \sum_{|k|\le\Lambda} v_{\mathrm{s}} k\, \eta^{\dagger}_{k} \eta_{k} + \sum_{|k|\le\Lambda} v_{\mathrm{s}} k\, \eta^{\dagger}_{k+\frac{2\pi}{3}} \eta_{k+\frac{2\pi}{3}} \\ &\equiv \sum_{|k|\le\Lambda} v_{\mathrm{s}} k\, \eta(1)^{\dagger}_{k} \eta(1)_{k} + \sum_{|k|\le\Lambda} v_{\mathrm{s}} k\, \eta(2)^{\dagger}_{k} \eta(2)_{k} + \sum_{|k|\le\Lambda} v_{\mathrm{s}} k\, \eta(3)^{\dagger}_{k} \eta(3)_{k} , \end{aligned} \tag{E.1}$$

where the common "light velocity" $v_{\mathrm{s}} = 6J^{XZX}$ and E_{ZP} denotes the regularized zero-point energy. The summation over k should be cut off at Λ which gives the bound for the linearization of the spectrum. Due to the non-local nature of the Jordan–Wigner transformation (2.3.24), the boundary condition (or, the allowed values of momentum k) for the fermion depends explicitly on the total fermion number F:

$$k = \begin{cases} \frac{2\pi}{N}(j + 1/2) \ \ (j = 0, \ldots, N-1) & \text{when } F \text{ is even} \\ \frac{2\pi}{N} j \ \ (j = 0, \ldots, N-1) & \text{when } F \text{ is odd} . \end{cases} \tag{E.2}$$

When the system size N is an integer-multiple of 3, the above moding carries over to the individual branches $\eta(i)$ $(i = 1, 2, 3)$ [159] and the zero-point energy is given by

$$E_{\mathrm{ZP}} = \begin{cases} N\epsilon_{\infty} - \frac{\pi v_{\mathrm{s}}}{6N}\frac{3}{2} & F = \text{even} \\ N\epsilon_{\infty} - \frac{\pi v_{\mathrm{s}}}{6N}\frac{3}{2} + \frac{2\pi v_{\mathrm{s}}}{N}\frac{3}{8} & F = \text{odd} \end{cases} \tag{E.3}$$

up to $O(1/N)$.

In order to take into account the fermion-number dependence of the boundary condition, it is convenient to introduce the following projection operator which is written in terms of the fermion numbers $\{F^{(i)}_{\mathrm{R/L}}\}$ of the individual Majorana branches:

$$\begin{aligned} &\mathcal{P}_{\pm} \equiv \frac{1}{2}\left[1 \pm (-1)^{F}\right] \\ &F = F^{(1)}_{\mathrm{L}} + F^{(1)}_{\mathrm{R}} + F^{(2)}_{\mathrm{L}} + F^{(2)}_{\mathrm{R}} + F^{(3)}_{\mathrm{L}} + F^{(3)}_{\mathrm{R}} , \end{aligned} \tag{E.4}$$

where $\mathcal{P}_{+}$ $(\mathcal{P}_{-})$ must be used with anti-periodic (periodic) moding. As $F^{(i)}_{\mathrm{R}} =$

$\sum_{k>0} \eta(i)^{\dagger}_{k}\eta(i)_{k}$, $F_{\mathrm{L}}^{(i)} = \sum_{k>0} \eta(i)^{\dagger}_{-k}\eta(i)_{-k}$, the partition function for the even-F sector (at temperature T) is calculated as

$$\begin{aligned}
&Z_{F\text{-even}} \\
&= q^{-\frac{3}{48}}\bar{q}^{-\frac{3}{48}} \operatorname{Tr} \mathcal{P}_{+}\, q^{\sum_{i=1}^{3}\sum_{n_i>0} n_i \eta(i)^{\dagger}_{n_i}\eta(i)_{n_i}}\, \bar{q}^{\sum_{n_i}\sum_{n_i>0} n_i \eta(i)^{\dagger}_{-n_i}\eta(i)_{-n_i}} \\
&= \frac{1}{2}(q\bar{q})^{-\frac{3}{48}} \Bigg\{ \left(\operatorname{Tr} q^{\sum_{n>0} n\eta^{\dagger}_{n}\eta_{n}}\right)^{3} \left(\operatorname{Tr} \bar{q}^{\sum_{n>0} n\eta^{\dagger}_{-n}\eta_{-n}}\right)^{3} \\
&\quad + \left(\operatorname{Tr}(-1)^{F_{\mathrm{L}}} q^{\sum_{n>0} n\eta^{\dagger}_{n}\eta_{n}}\right)^{3} \left(\operatorname{Tr}(-1)^{F_{\mathrm{R}}} \bar{q}^{\sum_{n>0} n\eta^{\dagger}_{-n}\eta_{-n}}\right)^{3} \Bigg\} \\
&= \frac{1}{2}(q\bar{q})^{-\frac{3}{48}} \Bigg\{ \left[\prod_{n=0}^{\infty}(1+q^{n+\frac{1}{2}}) \prod_{\bar{n}=0}^{\infty}(1+\bar{q}^{\bar{n}+\frac{1}{2}})\right]^{3} \\
&\quad + \left[\prod_{n=0}^{\infty}(1-q^{n+\frac{1}{2}}) \prod_{\bar{n}=0}^{\infty}(1-\bar{q}^{\bar{n}+\frac{1}{2}})\right]^{3} \Bigg\} \\
&= \frac{1}{2}\left(\left|\frac{\vartheta_3(q)}{\eta(q)}\right|^{3} + \left|\frac{\vartheta_4(q)}{\eta(q)}\right|^{3} \right) ,
\end{aligned} \tag{E.5}$$

where

$$q = \bar{q} = \exp\left(-\frac{2\pi v_{\mathrm{s}}}{TN}\right) \tag{E.6}$$

and the Boltzmann constant is set to unity. The $\vartheta_i(q)$ are the Jacobi theta functions [160] $\vartheta_i(q) \equiv \vartheta_i(0, q^{\frac{1}{2}})$ and

$$\eta(q) = q^{\frac{1}{24}} \prod_{n=1}^{\infty}(1-q^{n}) . \tag{E.7}$$

Similarly, the partition function for the subspace with odd fermion numbers $Z_{F\text{-odd}}$ is given by

$$\begin{aligned}
&Z_{F\text{-odd}}\\
&= q^{-\frac{3}{48}}\,\bar{q}^{-\frac{3}{48}}\,\mathrm{Tr}\,\mathcal{P}_-\, q^{\sum_i \sum_{n_i\geq 0}\left[n_i\eta(i)^\dagger_{n_i}\eta(i)_{n_i}+\frac{1}{16}\right]}\bar{q}^{\sum_i \sum_{n_i>0}\left[n_i\eta(i)^\dagger_{-n_i}\eta(i)_{-n_i}+\frac{1}{16}\right]}\\
&= \frac{1}{2}(q\bar{q})^{\frac{3}{24}}\left\{\left[\prod_{n=0}^{\infty}(1+q^n)\prod_{\bar{n}=1}^{\infty}(1+\bar{q}^{\bar{n}})\right]^3\right.\\
&\qquad\qquad\left.+\left[\prod_{n=0}^{\infty}(1-q^n)\prod_{\bar{n}=1}^{\infty}(1-\bar{q}^{\bar{n}})\right]^3\right\}\\
&= \frac{1}{2}\left|\frac{\vartheta_2(q)}{\eta(q)}\right|^3 .
\end{aligned} \tag{E.8}$$

In deriving the above, we have used the fact that the zero mode $n = 0$ is occupied by either $\eta(i)_\mathrm{R}$ or $\eta(i)_\mathrm{L}$ [here $\eta(i)_\mathrm{R}$]. Therefore, the full (low-energy) partition function at the multicritical point M1 reads as

$$Z_{\mathrm{M1}} = Z_{F\text{-even}} + Z_{F\text{-odd}} = \frac{1}{2}\left(\left|\frac{\vartheta_3(q)}{\eta(q)}\right|^3 + \left|\frac{\vartheta_4(q)}{\eta(q)}\right|^3 + \left|\frac{\vartheta_2(q)}{\eta(q)}\right|^3\right) , \tag{E.9}$$

which is *different* from that of three decoupled Ising models:

$$(Z_{\mathrm{Ising}})^3 = \left\{\frac{1}{2}\left(\left|\frac{\vartheta_3(q)}{\eta(q)}\right| + \left|\frac{\vartheta_4(q)}{\eta(q)}\right| + \left|\frac{\vartheta_2(q)}{\eta(q)}\right|\right)\right\}^3 . \tag{E.10}$$

In fact, we can show that Z_{M1} is equivalent to the partition function of the level-1 SO(3) WZW model [161, 162]. To see this, it is convenient to expand $q^{\frac{3}{48}}\bar{q}^{\frac{3}{48}}Z_{\mathrm{M1}}$ in a power series of q and $\bar{q}$:

$$q^{\frac{3}{48}}\bar{q}^{\frac{3}{48}}Z_{\mathrm{M1}} = 1 + 4q^{\frac{3}{16}}\bar{q}^{\frac{3}{16}} + 9q^{\frac{1}{2}}\bar{q}^{\frac{1}{2}} + 3q + 3\bar{q} + \cdots \tag{E.11}$$

For instance, the coefficient 3 of q ($\bar{q}$) in $q^{\frac{3}{48}}\bar{q}^{\frac{3}{48}}Z_{\mathrm{M1}}$ coincides with the number of the left (right) SO(3) currents. Similarly, the coefficient 4 (9) of $(q\bar{q})^{\frac{3}{16}}$ [$(q\bar{q})^{\frac{1}{2}}$] comes from the number of the WZW primary fields with $(h,\bar{h}) = \left(\frac{3}{16},\frac{3}{16}\right)$ [$(h,\bar{h}) = \left(\frac{1}{2},\frac{1}{2}\right)$] transforming under the spinor (vector) representation of SO(3) [163]. Note that the non-trivial boundary condition (E.2) has led us to summing over all possible fermionic boundary conditions and reproduces the correct partition function of the WZW model. We can follow similar steps to derive the partition function corresponding to the multicritical point M2:

$$Z_{\mathrm{M2}} = \frac{1}{2}\left(\left|\frac{\vartheta_3(q)}{\eta(q)}\right|^4 + \left|\frac{\vartheta_4(q)}{\eta(q)}\right|^4 + \left|\frac{\vartheta_2(q)}{\eta(q)}\right|^4\right) , \tag{E.12}$$

which implies that the critical point M2 is described by the level-1 SO(4) WZW model.

Acknowledgement

I would like to express my deepest gratitude to my supervisor, Prof. Keisuke Totsuka, for his guidance and comments throughout my research life. I am grateful to him for his insightful comments on my papers and presentations. I would also like to thank Prof. Shu Tanaka and Prof. Ippei Danshita for their collaborations and discussions. I am grateful to Prof. Masatoshi Sato for his lectures and discussions on physics. I would like thank members of my laboratory, Yukihisa Imamura, Kazuma Nagao, Kazuhiko Tanimoto, Dr. Takuto Kawakami, Dr. Toru Kikuchi, and Dr. Masaya Kunimi for their heart-warming supports and communications in my daily life. I would like to express my appreciation to former members of my institute, in particular, Prof. Takami Tohyama, Yuri Ichioka, Dr. Atsuo Shitade, Dr. Koudai Sugimoto, Dr. Kazuya Shinjo, Dr. Kiyoshi Kanazawa, Dr. Tomohiko G. Sano, Dr. Satoshi Takada, and Dr. Ryosuke Yoshii for their advices and discussions. I am grateful to my colleagues Hidekazu Tsukiji, Ichihiko Hashimoto, Kento Watanabe, and Ippei Obata for their support in my daily life. I also thank to Shigeo Hakkaku, Yuki Kamiya, Naotaka Kubo, Yuya Kusuki, Tsuyoshi Sugita, and Yota Watanabe for their communications in my daily life. I really appreciate Ryota Hirakawa for his discussions and lectures on mathematics. I would like to thank Yuya Nakagawa, Ryota Kawakami, and Koji Umemoto for their discussions and communications on physics and mathematics since high school. I would like to express my appreciation to Rie Tsukada for her encouragement and discussions on English and philosophy.

I was supported by Grant-in-Aid for JSPS Fellows. The computations in the present work were carried out on the computers at Yukawa Institute for Theoretical Physics, Kyoto University.

Finally, I would like to give a special thanks to my family for their support and encouragement in my life.

Bibliography

[1] L. D. Landau and E. M. Lifschitz, *Statistical Physics - Course of Theoretical Physics Vol 5* (Pergamon, London, 1958).

[2] K. v. Klitzing, G. Dorda, and M. Pepper, Phys. Rev. Lett. **45**, 494 (1980).

[3] R. B. Laughlin, Phys. Rev. B **23**, 5632 (1981).

[4] I. Affleck, T. Kennedy, E. H. Lieb, and H. Tasaki, Phys. Rev. Lett. **59**, 799 (1987).

[5] I. Affleck, T. Kennedy, E. H. Lieb, and H. Tasaki, Commun. Math. Phys. **115**, 583 (1988).

[6] M. den Nijs and K. Rommelse, Phys. Rev. B **40**, 4709 (1989).

[7] Y. Hatsugai and M. Kohmoto, Phys. Rev. B **44**, 11789 (1991).

[8] K. Hida, Phys. Rev. B **45**, 2207 (1992).

[9] M. Kohmoto and H. Tasaki, Phys. Rev. B **46**, 3486 (1992).

[10] T. Kennedy and H. Tasaki, Phys. Rev. B **45**, 304 (1992).

[11] M. Oshikawa, J. Phys.: Condens. Matter **4**, 7469 (1992).

[12] K. Totsuka and M. Suzuki, J. Phys.: Condens. Matter **7**, 1639 (1995).

[13] X.-G. Wen, F. Wilczek, and A. Zee, Phys. Rev. B **39**, 11413 (1989).

[14] X.-G. Wen, Phys. Rev. B **44**, 2664 (1991).

[15] C. L. Kane and E. J. Mele, Phys. Rev. Lett. **95**, 146802 (2005).

[16] B. Andrei Bernevig, T. L. Hughes, and S.-C. Zhang, Science, **314**, 1757 (2006).

[17] M. König, S. Wiedmann, C. Brüne, A. Roth, H. Buhmann, L. W. Molenkamp, X.-L. Qi, and S.-C. Zhang, Science **318**, 766 (2007).

[18] J. E. Moore and L. Balents, Phys. Rev. B **75**, 121306 (2007).

[19] L. Fu, C. L. Kane, and E. J. Mele, Phys. Rev. Lett. **98**, 106803 (2007).

[20] A. Y. Kitaev, Physics-Usp. **44**, 131 (2001).

[21] X-L Qi and S-C Zhang, Rev. Mod. Phys. **83**, 1057.

[22] X.-G. Wen, Phys. Rev. B **41**, 12838 (1990).

[23] B. I. Halperin, Phys. Rev. Lett. **52**, 1583 (1984).

[24] D. Arovas, J. R. Schrieffer, and F. Wilczek, Phys. Rev. Lett. **53**, 722 (1984).

[25] X.-G. Wen, Int. J. Mod. Phys. B **4**, 239 (1990).

[26] X.-G. Wen and Q. Niu, Phys. Rev. B **41**, 9377 (1990).

[27] D. J. Thouless, M. Kohmoto, M. P. Nightingale, and M. den Nijs, Phys. Rev. Lett. **49**, 405 (1982).

[28] Y. Oreg, G. Refael, and F. von Oppen, Phys. Rev. Lett. **105**, 177002 (2010).

[29] V. Mourik, K. Zou, S. M. Plissard, E. P. A. M. Bakkers, and L. P. Kouwenhoven, Science **336**, 25 (2012).

[30] L. P. Rokhinson, X. Liu, and J. K. Furdyna, Nat. Phys. **8**, 795 (2012).

[31] L. Jiang, T. Kitagawa, J. Alicea, A. R. Akhmerov, D. Pekker, G. Refael, J. I. Cirac, E. Demler, M. D. Lukin, and P. Zoller, Phys. Rev. Lett. **106**, 220402 (2011).

[32] S. B. Bravyi and A. Y. Kitaev, Annals of Physics **298**, 210 (2002).

[33] C. Nayak, S. H. Simon, A. Stern, M. Freedman, and S. D. Sarma, Rev. Mod. Phys. **80**, 1083 (2008).

[34] C. Holzhey, F. Larsen, and F. Wilczek, Nucl. Phys. B **424**, (1994) 443.

[35] P. Calabrese and J. Cardy, J. Stat. Mech. Theor. Exp. (2004) P06002.

[36] J. I. Latorre, E. Rico, and G. Vidal, Quant. Inf. Comput. **4**, 48 (2004).

[37] A. Kitaev and J. Preskill, Phys. Rev. Lett. **96**, 110404 (2006).

[38] M. Levin and X.-G. Wen, Phys. Rev. Lett. **96**, 110405 (2006).

[39] M. Hastings, Journal of Statistical Mechanics:Theory and Experiment **2007** P08024 (2007).

[40] S. Furukawa and G. Misguich, Phys. Rev. B **75**, 214407 (2007).

[41] H. Katsura, T. Hirano, and Y. Hatsugai, Phys. Rev. B **76**, 012401 (2007).

[42] H. Katsura, T. Hirano, and V. E. Korepin, J. Phys. A **41**, 135304 (2008).

[43] H. Katsura, N. Kawashima, A. N. Kirillov, V. E. Korepin, and S. Tanaka, J. Phys. A **43**, 255303 (2010).

[44] J. Eisert, M. Cramer, M.B. Plenio, Rev. Mod. Phys. **82**, 277 (2010).

[45] H.-C. Jiang, Z. Wang, and L. Balents, Nature Physics **8**, 902 (2012).

[46] H. Li and F. D. M. Haldane, Phys. Rev. Lett. **101**, 010504 (2008).

[47] F. Pollmann, A. M. Turner, E. Berg, and M. Oshikawa, Phys. Rev. B **81**, 064439 (2010).

[48] A. M. Turner, F. Pollmann, and E. Berg, Phys. Rev. B **83**, 075102 (2011).

[49] K. Hasebe and K. Totsuka, Phys. Rev. B **84**, 104426 (2011).

[50] J. I. Cirac, D. Poilblanc, N. Schuch, and F. Verstraete, Phys. Rev. B **83**, 245134 (2011).

[51] J. Lou, S. Tanaka, H. Katsura, and N. Kawashima, Phys. Rev. B **84**, 245128 (2011).

[52] M. Fagotti, P. Calabrese, and J. E. Moore, Phys. Rev. B **83**, 045110 (2011).

[53] A. Sterdyniak, A. Chandran, N. Regnault, B. A. Bernevig, and P. Bonderson, Phys Rev. B **85**, 125308 (2012).

[54] S. Tanaka, R. Tamura, and H. Katsura, Phys. Rev. A **86**, 032326 (2012).

[55] X.-L. Qi, H. Katsura, and A. W. W. Ludwig, Phys. Rev. Lett. **108**, 196402 (2012).

[56] H. Nonne, M. Moliner, S. Capponi, P. Lecheminant, and K. Totsuka, Europhys. Lett. **102**, 37008 (2013).

[57] L. Cincio and G. Vidal, Phys. Rev. Lett. **110**, 067208 (2013).

[58] K. Shinjo, S. Sota, and T. Tohyama, Phys. Rev. B **91**, 054401 (2015).

[59] K. Tanimoto and K. Totsuka, arXiv:1508.07601 (2015).

[60] J. Alicea, Y. Oreg, G. Refael, F. von Oppen, and M. P. A. Fisher, Nat. Phys. **7**, 412-417 (2011).

[61] L.-H. Wu, Q.-F. Liang, and X. Hu, Sci. Technol. Adv. Mater. **15** (2014) 064402.

[62] C. S. Amorim, K. Ebihara, A. Yamakage, Y. Tanaka, and M. Sato, Phys. Rev. B **91**, 174305 (2015).

[63] J. Alicea, Rep. Prog. Phys. **75**, 076501 (2012).

[64] W. DeGottardi, D. Sen, and S. Vishveshwara, Phys. Rev. Lett. **110**, 146404 (2013).

[65] W. DeGottardi, M. Thakurathi, S. Vishveshwara, and D. Sen, Phys. Rev. B **88**, 165111 (2013).

[66] L.-J. Lang and S. Chen, Phys. Rev. B **86**, 205135 (2012).

[67] M. Tezuka and N. Kawakami, Phys. Rev. B **88**, 155428 (2013).

[68] X. Cai, L.-J. Lang, S. Chen, and Y. Wang, Phys. Rev. Lett. **110**, 176403 (2013).

[69] E. M. Stoudenmire, J. Alicea, O. A. Starykh, and M. P. A. Fisher, Phys. Rev. B **84**, 014503 (2011).

[70] M. Suzuki and R. Kubo, J. Phys. Soc. Jpn. **24**, 51 (1968).

[71] T. W. B. Kibble, J. Phys. A **9**, 1387 (1976).

[72] W. H. Zurek, Nature **310**, 505 (1985).

[73] W. H. Zurek, U. Dorner, and P. Zoller, Phys. Rev. Lett. **95**, 105701 (2005).

[74] V. Mukherjee, U. Divakaran, A. Dutta, and D. Sen, Phys. Rev. B. **76**, 174303 (2007).

[75] J. Dziarmaga, Adv. Phys. **59**, 1063 (2010).

[76] A. Das, Phys. Rev. B **82**, 172402 (2010).

[77] A. Polkovnikov, K. Sengupta, A. Silva, and M. Vengalattore, Rev. Mod. Phys. **83**, 863 (2011).

[78] S. Suzuki, J. Inoue, and B. K. Chakrabarti, *Quantum Ising Phases and Transitions in Transverse Ising Models*, Lecture Notes in Physics **862** (Springer, Heidelberg, 2013).

[79] E. Canovi, E. Ercolessi, P. Naldesi, L. Taddia, and D. Vodola, Phys. Rev. B **89**, 104303 (2014).

[80] G. Torlai, G. Taglicazzo, and G. D. Chiara, J. Stat. Mech. (2014) P06001.

[81] R. Vosk and E. Altman, Phys. Rev. Lett. **112**, 217204 (2014).

[82] A. Bermudez, D. Patanè, L. Amico, and M. A. Martin-Delgado, Phys. Rev. Lett. **102**,

135702 (2009).

[83] A. Bermudez, L. Amico, and M. A. Martin-Delgado, New. J. Phys. **12**, 055014 (2010).

[84] G. Kells, D. Sen, J. K. Slingerland, and S. Vishveshwara, Phys. Rev. B **89**, 235130 (2014).

[85] S. Hegde, V. Shivamoggi, S. Vishveshwara, and D. Sen, New J. Phys. **17** (2015) 053036.

[86] L. Mazza, D. Rossini, M. Endres, and R. Fazio, Phys. Rev. B **90**, 020301 (2014).

[87] E. P. L. van Nieuwenburg and S. D. Huber, Phys. Rev. B **90**, 075141 (2014).

[88] C. Chamon, M. O. Goerbig, R. Moessner, and L. F. Cugliandolo, *Topological Aspects of Condensed Matter Physics*, Lecture Notes of the Les Houches Summer School: Volume 103, August 2014 (Oxford University Press, GB, 2017).

[89] G. Vidal, Phys. Rev. Lett. **98**, 070201 (2007).

[90] R. Orús and G. Vidal, Phys. Rev. B **78**, 155117 (2008).

[91] T. Ohta, S. Tanaka, I. Danshita, and K. Totsuka, J. Phys. Soc. Jpn. **84**, 063001 (2015).

[92] T. Ohta, S. Tanaka, I. Danshita, and K. Totsuka, Phys. Rev. B **93**, 165423 (2016).

[93] T. Ohta and K. Totsuka, J. Phys. Soc. Jpn. **85**, 074003 (2016).

[94] X. Chen, Z.-C. Gu, and X.-G. Wen, Phys. Rev. B **83**, 035107 (2011).

[95] X. Chen, Z.-C. Gu, and X.-G. Wen, Phys. Rev. B **84**, 235128 (2011).

[96] N. Schuch, D. Pérez-García, and J. I. Cirac, Phys. Rev. B **84**, 165139 (2011).

[97] R. White, Phys. Rev. Lett. **69**, 2863 (1992).

[98] X. Chen, Z.-C. Gu, and X.-G. Wen, Phys. Rev. B **82**, 155138 (2010).

[99] M. B. Hastings and X.-G. Wen, Phys. Rev. B **72**, 045141 (2005).

[100] Z.-C. Gu and X.-G. Wen, Phys. Rev. B **80**, 155131 (2009).

[101] S.-P. Kou and X.-G. Wen, Phys. Rev. B **80**, 224406 (2009).

[102] A. Kapustin, R. Thorngren, A. Turzillo, and Z. Wang, JHEP 1512:052 (2015).

[103] L. Fidkowski and A. Kitaev, Phys. Rev. B **83**, 075103 (2011).

[104] X.-G. Wen, Phys. Rev. B **65**, 165113 (2002).

[105] X.-G. Wen, Phys. Rev. D **68**, 065003 (2003)

[106] U. Schollwöck, Annals of Physics **326**, 96 (2011).

[107] M. Hasting and T. Koma, Communinations in Mathematical Physics **265** 781 (2006).

[108] P. Pfeuty, Ann. Phys. **57**, 79 (1970).

[109] S. Sachdev, *Quantum Phase Transitions*, (Cambridge Univ. Press, Cambridge, 2001).

[110] 太田卓見, 長距離相互作用のあるフェルミオン模型のダイナミクス, 物性研究・電子版 **4**, 4, 044601.

[111] M. Hastings, Phys. Rev. B **73**, 085115 (2006).

[112] F. Verstraete and J. I. Cirac, arXiv:0407066 (2004).

[113] G. Vidal, Phys. Rev. Lett. **101**, 110501 (2008).

[114] G. Vidal, Phys. Rev. Lett. **91**, 147902 (2003).

[115] D. Pérez-García, F. Verstraete, M. M.Wolf, and J. I. Cirac, Quantum Inf. Comput. **7**, 401 (2007).

[116] R. Orús, Annals of Physics **349**, 117 (2014).

[117] M. Fannes, B. Nachtergaele, and R. F. Werner, Comm. Math. Phys. **144**, 443 (1992).

[118] D. Pérez-García, M. M. Wolf, M. Sanz, F. Verstraete, and J. I. Cirac, Phys. Rev. Lett. **100**, 167202 (2008).

[119] F. Pollmann and A. M. Tuner, Phys. Rev. B **86**, 125441 (2012).

[120] P. Jordan and E. P. Wigner, Zeitschrift fur Physik, **47**, 631 (1928).

[121] E. Lieb, T. Schultz, and D. Mattis, Ann. Phys. (N.Y.) **16**, 407 (1961).

[122] E. Majorana, Nuovo Cimento **14**, 171 (1937).

[123] S. Tomonaga, Progr. Theor. Phys. **5**, 544(1950).

[124] J. M. Luttinger, J. Math. Phys. **4**, 1154 (1963).

[125] A. Altland and M. R. Zirnbauer, Phys. Rev. B **55**, 1142 (1997).

[126] A. Kitaev, AIP Conf. Proc. **1134**, 22 (2009).

[127] A. P. Schnyder, S. Ryu, A. Furusaki, and A. W. W. Ludwig, Phys. Rev. B **78**, 195125 (2008).

[128] S. Ryu, A. P. Schnyder, A. Furusaki, and A. W. W. Ludwig, New J. Phys. **12**, 065010 (2010).

[129] L. Fidkowski and A. Kitaev, Phys. Rev. B **81**, 134509 (2010).

[130] Y. Niu, S. B. Chung, C.-H. Hsu, I. Mandal, S. Raghu, and S. Chakravarty, Phys. Rev. B **85**, 035110 (2012).

[131] M. Suzuki, Prog. Theor. Phys. **46**, 1337 (1971).

[132] S. O. Skrøvseth and S. D. Bartlett, Phys Rev. A **80**, 022316 (2009).

[133] W. Son, L. Amico, R. Fazio, A. Hamma, S. Pascazio, and V. Vedral, Europhys. Lett. **95**, 50001 (2011).

[134] P. Smacchia, L. Amico, P. Facchi, R. Fazio, G. Florio, S. Pascazio, and V. Vedral, Phys. Rev. A **84**, 022304 (2011).

[135] R. Raussendorf and H. J. Briegel, Phys. Rev. Lett. **86**, 5188 (2001).

[136] R. Raussendorf, D. E. Browne, and H. J. Briegel, Phys. Rev. A **68**, 022312 (2003).

[137] K. Fujii, Y. Nakata, M. Ohzeki, and M. Murao, Phys. Rev. Lett. **110**, 120502 (2013).

[138] Y. Bahri, R. Vosk, E. Altman, and A. Vishwanath, Nature Communications **6**, 7341 (2015).

[139] J. K. Pachos and M. B. Plenio, Phys. Rev. Lett. **93**, 056402 (2004).

[140] V. Lahtinen and E.Ardonne, Phys. Rev. Lett. **115**, 237203 (2015).

[141] E. Barouch and B. M. McCoy, Phys. Rev. A **3**, 786 (1971).

[142] L. Amico and A. Osterloh, J. Phys. A: Math. Gen. **37** (2004) 291.

[143] E. Barouch, B. M. McCoy, and M. Dresden, Phys. Rev. A **2**, 1075 (1970).

[144] T. Caneva, R. Fazio, and G. E. Santoro, Phys. Rev. B **76**, 144427 (2007).

[145] M. Suzuki, Phys. Lett. A. *146*, 319 (1990).

[146] H. W. J. Blöte, J. L. Cardy, and M. P. Nightingale, Phys. Rev. Lett. **56**, 742 (1986).

[147] J. Cardy, Nucl.Phys. B **270**, 186 (1986).

[148] I. Affleck, Phys. Rev. Lett. **56**, 746 (1986).

[149] In Ref. [134], the universality of three decoupled Ising models was concluded. However, the system at M1 has much larger SO(3) symmetry.

[150] P. W. Anderson, Phys. Rev. **110**, 827 (1958).

[151] I. Peschel, J. Phys. A: Math. Gen. **36**, L205 (2003).

[152] I. Peschel and V. Eisler, J. Phys. A: Math. Theor. **42** 504003 (2009).

[153] J. Sirker, M. Maiti, N.P. Konstantinidis, and N. Sedlmayr, J. Stat. Mech. P10032 (2014).

[154] J. Dziarmaga, Phys. Rev. B **74**, 064416 (2006).

[155] A. Das and B. K. Chakrabarti, Rev. Mod. Phys. **80**, 1061 (2008).

[156] S. Suzuki, J. Phys.: Conf. Ser. **302** 012046 (2011).

[157] R. Wakatsuki, M. Ezawa, and N. Nagaosa, Phys. Rev. B **89**, 174514 (2014).

[158] C.-K. Chiu, J. C. Teo, A. P. Schnyder, and S. Ryu, Rev. Mod. Phys. **88**, 035005 (2015).

[159] Unless this condition is met, the continuum limit is ill-defined and we cannot construct the vacuum of the corresponding CFT.

[160] I.S. Gradshteyn and I.M. Ryzhik, *Table of Integrals, Series, and Products*, Academic Press, 2000.

[161] E. Witten, Comm. Math. Phys. **92**, 455 (1984).

[162] V. Knizhnik and A.B. Zamolodchikov, Nucl. Phys. B **247**, 83 (1984).

[163] P. di Francesco, P. Mathieu, and D. Sénéchal, *Conformal Field Theory*, Springer, 1996.